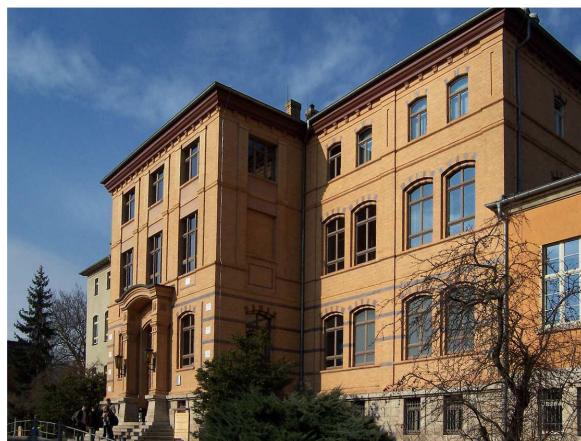


# Institut für Festkörperphysik

FRIEDRICH-SCHILLER-UNIVERSITÄT JENA



 <p><b>Tiefemperaturphysik</b> Prof. Dr. P. Seidel</p>	 <p><b>Angewandte Physik / Festkörperphysik</b> Prof. Dr. T. Fritz</p>
 <p><b>Experimentelle Festkörperphysik</b> Prof. Dr. C. Röhning</p>	 <p><b>Ionenstrahlphysik</b> Prof. Dr. W. Wesch</p>
 <p><b>Photovoltaik</b> Prof. Dr. C. Röhning</p>	 <p><b>Laborastrophysik und Clusterphysik</b> Prof. Dr. F. Huisken</p>

**Annual Report 2011**

# Institut für Festkörperphysik

Friedrich-Schiller-Universität Jena

*Annual Report 2011*



**Editors:** Prof. Dr. Carsten Ronning

**Institut für Festkörperphysik  
Friedrich-Schiller-Universität Jena  
Max-Wien-Platz 1  
D-07743 JENA**

Tel.: +49 (0) 3641 / 947300  
Fax: +49 (0) 3641 / 947302  
e-mail: carsten.ronning@uni-jena.de  
home page: <http://www.ifk.uni-jena.de/>

Prof. Dr. Carsten Ronning  
director Tel.: +49 (0) 3641 / 947300, 947301  
Fax: +49 (0) 3641 / 947302  
e-mail: carsten.ronning@uni-jena.de  
home page: <http://www.nano.uni-jena.de>  
<http://www.photovoltaik.uni-jena.de>

Prof. Dr. Torsten Fritz Tel.: +49 (0) 3641 / 947400, 947411  
Fax: +49 (0) 3641 / 947412  
e-mail: torsten.fritz@uni-jena.de  
home page: <http://www.organics.uni-jena.de>

Prof. Dr. Friedrich Huisken Tel.: +49 (0) 3641 / 947354, 947301  
Fax: +49 (0) 3641 / 947308  
e-mail: friedrich.huisken@uni-jena.de  
home page: <http://www.astrolab.uni-jena.de>

Prof. Dr. Paul Seidel Tel.: +49 (0) 3641 / 947410, 947411  
Fax: +49 (0) 3641 / 947412  
e-mail: paul.seidel@uni-jena.de  
home page: <http://www.physik.uni-jena.de/~tief>

Prof. Dr. Werner Wesch Tel.: +49 (0) 3641 / 947330, 947301  
Fax: +49 (0) 3641 / 947302  
e-mail: werner.wesch@uni-jena.de  
home page: <http://www.physik.uni-jena.de/inst/exphys//ionen/>

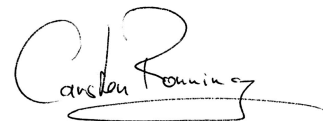
## Preface

We like to take this annual report 2011 as an opportunity to thank a lot of people and organizations for their manifold support for our research at the Institute of Solid-State Physics at the Friedrich-Schiller-University Jena. Furthermore, this report, which is already the 16<sup>th</sup> in this series, is also addressed to the interested scientific community and to our colleagues within the university and from outside.

Special thanks go to the following organizations for their financial support:

- Deutsche Forschungsgemeinschaft – DFG
- Bundesministerium für Bildung und Forschung – BMBF
- Bundesministerium für Umwelt, Naturschutz und Reaktorsicherheit – BMU
- Bundesministerium für Wirtschaft und Technologie – BMWi
- Thüringer Ministerium für Bildung, Wissenschaft und Kultur – TMBWK
- Deutscher Akademischer Austauschdienst – DAAD
- Gesellschaft für Schwerionenforschung, Darmstadt – GSI
- Deutsches Elektron Synchrotron, Hamburg – DESY
- Several Industrial Partners

We like also to thank all our colleagues at other Universities and Institutes, which are collaborating with us, but the collaborative work has not be presented in the research articles of this report. Furthermore, we are very grateful for the work of our very motivated secretaries, technicians and the people in the mechanical and electrical workshops. All have contributed to our research in an outstanding way and, thus, to this report.

A handwritten signature in black ink, consisting of a large, stylized 'C' and 'R' followed by the name 'Carsten Ronning' written in a cursive script.

Prof. Dr. Carsten Ronning

# Contents

<b>1. Scientific groups of the institute</b>	7
<b>2. Scientific reports</b>	
Effects of self-assembled gold nanoparticles on the flux pinning in $\text{YBa}_2\text{Cu}_3\text{O}_{7-\delta}$ thin film devices.....	12
Investigations on dc-SQUIDs based on growth modified bi-crystal grain boundaries.....	14
Josephson current second harmonic effects on magnetic flux in long junctions.....	16
Coherent radiation of self-heated Josephson junctions in the resonator.....	18
Weak continuous monitoring of a flux qubit - resonator system with intermediate coupling.....	20
Cryogenic Current Comparator for FAIR.....	22
SQIF-based dc SQUID amplifier with intrinsic negative feedback.....	24
Spatial resolved Magnetorelaxometry in combination with toxicological characterization of magnetic nanoparticles.....	26
Conductive Zinc oxide thin films coated by combustion CVD using aerosol droplets at atmospheric pressure.....	28
Mechanical loss of a sapphire single crystal at low temperatures.....	30
Oxygen induced mechanical loss in crystalline silicon.....	32
Parametric instabilities in future gravitational wave detectors.....	34
Investigation of the mechanical loss of a thin crystalline quartz flexure.....	36
Rare-Earth Compound Regenerator for a Coaxial Two Stage Pulse Tube Refrigerator.....	38
Josephson junctions with different transparency distribution functions.....	40
New closed cycle refrigerator system for electro-optical measurements.....	41
Luminescence of Ga-graded $\text{Cu}(\text{In,Ga})\text{Se}_2$ thin-films.....	42
Phosphorus doping of CdTe thin film solar cells.....	44
Photoluminescence of the back and front side of $\text{Cu}(\text{In,Ga})\text{Se}_2$ absorbers.....	46
Organic Heteroepitaxy of PTCDA and SnPc on Single Crystalline Silver.....	48
Quantification of LEED Measurements for Investigations of Organic Thin Films.....	50
Enhanced photoluminescence from Si nanocrystals deposited on ZnO Nanowires.....	52
Formation of GEMS from interstellar silicate dust.....	54
Structural modifications of low-energy heavy-ion irradiated germanium.....	56
Void formation in a-Ge due to high electronic energy deposition.....	58
Composition-dependent atomic-scale structure of $\text{Cu}(\text{In,Ga})\text{Se}_2$ .....	60
Qualitative analysis of diamond like carbon layers.....	62
Persistent Ion Beam Induced Conductivity in Zinc Oxide.....	64
Highly Mn doped GaAs nanowires by ion implantation.....	66
Determination of GaAs nanowire minority carrier diffusion lengths via EBIC from axial pn-junctions.....	68
DNA modification of zinc oxide nanowires for sensing application.....	70

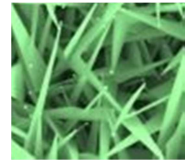
Nano-X-ray absorption spectroscopy of single Co-implanted ZnO nanowires .....	72
Contacting of ZnO nanowires by dielectrophoresis and electrical characterization.....	74
Realization and measurement of planar, edge-type and grain boundary Josephson junctions based on iron pnictide superconductors for examination of their order parameter symmetry .....	76
Domain Wall Dynamics in Soft Magnetic Nanostripes.....	78
Ion beam synthesis of silver clusters in lithium niobate .....	80
Damage formation in SiC ion implanted at 625 K .....	82
Damage formation and optical absorption in neutron irradiated SiC .....	84
<b>3. Technical reports and equipment</b>	
Operation of the ion-accelerators JULIA and the ion-implanter ROMEO .....	86
Cryogenic service .....	88
Equipment .....	89
<b>4. Current research projects</b>	<b>93</b>
<b>5. Publications</b>	
5.1 Publications in scientific journals .....	96
5.2 Invited talks and colloquia .....	103
5.3 Conference contributions .....	105
5.4 Theses .....	112
<b>6. Cooperations, guests and colloquia at IFK</b>	
6.1 Visiting scientists .....	115
6.2 Colloquia at Institute of Solid State Physics .....	115
<b>7. Teaching activities</b>	
7.1 Lectures .....	117
7.2 Seminars .....	117
7.3 Practica .....	118
<b>8. Personnel</b>	<b>119</b>



## Scientific groups of the institute

### Experimental Physics / Solid State Physics

*Prof. Dr. C. Ronning*



- Synthesis, doping and functionization of semiconductor nanowires
- Photovoltaics
- Growth and functionalization of diamond-like materials
- Semiconductor physics: doping using ion beams

Recent work of the research group in the field of semiconductor nanowires focuses both on the growth of desired nanostructures as well as on the modification of semiconductor nanowires for the use as photonic and electronic devices. This includes in realization of light-emitting diodes, field effect transistors, sensors for bio and chemical applications, and the observation of laser oscillations within single ZnO nanowires.

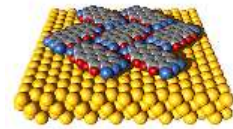
Another important scientific area of the group is the investigation of hard/soft interfaces in terms of biocompatibility. Here, the accelerator systems Mr. JIM Stringer and LEILA are used for the growth of diamond-like materials as well as for nanostructuring of surfaces (Rippels). The biocompatibility and bioactivity of such thin films and surfaces is currently investigated in collaboration with the IMT.

The research on photovoltaics is directed to two different fields: (a) Preparation and development of  $\text{Cu}(\text{In,Ga})(\text{Se,S})_2$  - based thin film solar cells (CIGS). The research aims at a better understanding of the materials science of the CIGS chalcopyrite semiconductor and the improvement of existing and the development of novel cell concepts. To this end, a complete baseline on a form factor of  $10 \times 10 \text{ cm}^2$  is available as well as various characterization tools including AM 1.5 solar simulation and spectral response. (b) Preparation and development of CdTe-based thin film solar cells. The research aims at a better understanding of the materials science of the II-VI semiconductor CdTe and the improvement of existing and the development of novel cell concepts. To this end, a complete baseline on a form factor of  $10 \times 10 \text{ cm}^2$  is available as well as various characterization tools including AM 1.5 solar simulation and spectral response.

Finally, it is worth to mention that on-going work of the group is performed in the area of ion beam doping of ZnO (in collaboration with Prof. Dr. M. Grundmann, Uni Leipzig), ion beam doping of  $\text{Cu}_2\text{O}$  thin films (Prof. Dr. B.K. Meyer, University of Gießen), ion beam analysis of thin high- $k$  materials (Dr. C. Wenger, IHP Frankfurt/Oder), and RBS-investigations of BN thin films (Prof. Dr. H.G. Boyen, Uni Hasselt).



## Applied Physics / Solid State Physics



*Prof. Dr. T. Fritz*

- Preparation of highly ordered thin films of organic molecules by UHV-deposition (OMBE)
- Chemical vapor deposition and characterization of carbon nanotubes
- Growth of graphene and carbon nanotubes on silicon carbide
- *In situ* optical spectroscopy (DRS and PL)
- Analyses of surfaces, layers and nanostructures using AES, XPS, LEED, RHEED, XPD, STM, AFM, and SEM

The group *Applied Physics / Solid State Physics* at the Institute of Solid State Physics is engaged in the research on nanostructures, solid surfaces and thin films of both organic and inorganic semiconductor materials.

Our main research interest lies in the discovery of structure-property-relations of structurally well defined ultrathin epitaxial layers, organic quantum wells and carbon nanotubes. The main target of our research is the development of basic principles for the use of nano materials in prospective devices.

For analyses of the chemical composition and bonding at surfaces and in thin films we use surface analysis methods like photoelectron spectroscopy (XPS, UPS) and Auger electron spectroscopy (AES). The crystalline structure can be determined by electron diffraction (LEED, RHEED, XPD, and electron channeling). Scanning tunneling microscopy (STM), atomic force microscopy (AFM) and scanning electron microscopy (SEM) are used for high-resolution imaging of nanostructures and surfaces.

Our *in situ* optical spectroscopy, namely differential reflectance spectroscopy (DRS) is used to study organic (sub-)monolayers and heterostructures in terms of absorption spectroscopy to analyse the optical interaction between the molecules or between organic adsorbates and inorganic substrates.

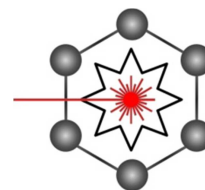
We have also developed a computational method to calculate the inter- and intralayer potential energy and to predict epitaxial alignments for realistically large OMBE domains (comprising several thousands of molecules).

Carbon nanotubes have been produced on solid substrates by chemical vapour deposition (CVD) using methane and ethanol as precursor gas. Extensive characterization of the CVD samples by SEM, AFM and Raman spectroscopy revealed high-quality single-wall carbon nanotubes of diameters between 1 and 2 nm. The amount of residual catalyst and amorphous carbon species has been determined to be very low. Our long-time experience in silicon carbide research has been used to grow graphene as well as carbon nanotubes on single-crystalline SiC substrates.

## Laboratory Astrophysics/Cluster Physics

*Prof. Dr. F. Huisken*

- Photoluminescence studies of silicon and germanium nanocrystals produced by CO<sub>2</sub> laser pyrolysis
- Electronic spectroscopy of neutral and ionized polycyclic aromatic hydrocarbons (PAHs) in supersonic jets and cryogenic matrices
- Study of astrochemical reactions in liquid helium nanodroplets



The Joint *Laboratory Astrophysics/Cluster Physics* Group at the Institute of Solid State Physics results from a cooperation between the MaxPlanckInstitute for Astronomy, Heidelberg, and the FriedrichSchillerUniversity, Jena. Inaugurated in February 2003, it is conducted by Prof. Dr. Thomas Henning and Prof. Dr. Friedrich Huisken.

The research of the Joint Laboratory Astrophysics and Cluster Physics Group is devoted to fundamental astrophysical questions that can be answered by laboratory experiments, with particular emphasis on spectroscopy. The electromagnetic radiation reaching us from stellar objects is modified in a characteristic manner by interstellar molecules and dust particles. Many of these “fingerprints” are still far from being understood. In order to determine the species causing the modification of the electromagnetic signals detected by telescopes and satellites, comprehensive laboratory studies are urgently needed.

The laboratory is equipped with modern molecular and cluster beam machines as well as laser systems to contribute to the clarification of such fundamental questions. For this purpose, the molecules, clusters, and nanoparticles of interest are prepared in vacuum chambers under conditions coming close to those encountered in the interstellar space (low temperature and low density).

## Low Temperature Physics

*Prof. Dr. P. Seidel*



- Superconductivity within thin layers and layer systems
- Josephson effects, proximity effect, and tunnel effects in superconducting devices
- DC-SQUID's and their application in measurement, e.g. biomagnetism, MRX, CCC
- cryogenic measurements of mechanical quality factor and optical properties
- Dynamics of superconducting Josephsonarrays
- cryogenic engineering (cryocoolers, cryogenic storage)

The *low temperature physics* group works on the following fields:

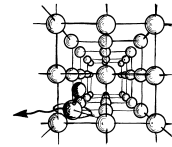
- preparation, characterization, modelling and application of Josephson junctions and SQUIDs (precision and magneto-relaxation measurements with LTS SQUIDs, development of HTS SQUIDs, intrinsic Josephson junctions and Josephson junctions with iron based superconductors)
- low temperature physics and cryogenic engineering (development of new kinds of pulse tube cryocoolers with magnetic regenerators, cryogenic storage, cryogenic current comparator CCC for particle beam analysis)
- experimental work within the SFB/TR on cryogenic measurements of the Q-factor and of optical properties of components for future gravitational wave detectors
- thin film technologies for insulators and other materials

The research is carried out in cooperations with other research groups in Thuringia (TU Ilmenau, IPHT Jena, SUPRACON Jena, Innovent e.V. Jena, Helmholtz Institute Jena). Within common activities the group works together with the Gesellschaft für Schwerionenforschung Darmstadt, DESY Hamburg, MPI Heidelberg, IFW Dresden and the Zentrum für Raumfahrttechnologie und Mikrogravitation and DLR Bremen.

Several research activities exist with industrial partners e.g. with Chemicell Berlin, HTS Systeme Wallenfels, and the TransMIT center for adaptive cryotechniques Gießen. A long tradition of cooperation with the the Universities of Moscow (Russia), Bratislava (Slovak Republic), Kharkov (Ukraine), Glasgow (U.K.), Poznan (Poland), Padua, Torino and Florence (Italy), Twente (Netherlands) and the Universities of Osaka, Tokyo and Nagoya (Japan) is also remarkable.

## Ion Beam Physics

*Prof. Dr. W. Wesch*



- Modification of solids by ion implantation and succeeding processes and ion beam analysis (RBS, PIXE, ERD, NRA)
- Ion beam synthesis of buried nanostructures
- Investigation of the effect of high electronic excitation on structural modification of crystalline and amorphous semiconductors
- Simulation of processes of ion-solid interaction

The *Ion Beam Physics* Group deals with modification of solids and synthesis of buried nanostructures using ion beams and combined secondary processes. The studies cover fundamental processes of ion-beam induced structural modification in semiconductors and insulators being relevant for future electronic, optoelectronic and photonic device technologies.

Concerning the II-VI semiconductors, in 2010 the studies were focused to the investigation of damage formation in CdTe at room temperature and 15 K using our two-beam irradiation chamber for in situ irradiation and ion beam analysis. Furthermore damage evolution in SiC by silver and neutron irradiation was investigated in collaboration with the University of Pretoria in South Africa. The investigation of structural modification of LiNbO<sub>3</sub> by ion irradiation as well as ion beam enhanced etching of this material was continued in collaboration with the Institute of Applied Physics. Additionally we started to study ion beam synthesis of metal nanoclusters in LiNbO<sub>3</sub> for photonic applications, and in collaboration with the University Minsk in Belarus we continued our work on ion beam synthesis of III-V compound nanoclusters in silicon.

Beside these activities on materials modification utilizing ion beams with conventional energies (several 10 keV to several MeV), the effect of high electronic excitation due to swift heavy ion irradiation (several 100 MeV) on plastic deformation and on the formation of voids and porous structures in amorphous Ge and GaSb were studied in collaboration with the Australian National University Canberra in Australia. The processes of void formation in amorphous Ge was also investigated by classical molecular dynamics computer simulations.

# Effects of self-assembled gold nanoparticles on the flux pinning in $\text{YBa}_2\text{Cu}_3\text{O}_{7-\delta}$ thin film devices

C. Katzer, P. Michalowski, F. Schmidl, J. Albrecht<sup>1</sup>, G. Schütz<sup>2</sup>, M. Rettenmayr<sup>3</sup> and P. Seidel

<sup>1</sup> Hochschule Aalen – Beethovenstraße 1, D-73430 Aalen

<sup>2</sup> Max-Planck-Institut für Intelligente Systeme – Heisenbergstraße 3, D-70569 Stuttgart

<sup>3</sup> Institut für Materialwissenschaft und Werkstofftechnologie – Löbdergraben 32, D-07749 Jena

The movement of flux vortices which typically is observed in high-temperature superconductors is an essential limiting factor for many applications. Especially the performance of magnetic field sensors such as direct current superconducting quantum interference device (dc-SQUID) gradiometers is determined by the motion of magnetic flux as it is linked to flux noise. In the last couple of years several possibilities to suppress this vortex motion have been reported. One approach was to reduce the width of the superconducting lines by patterning small slits in the washer structures of the dc-SQUIDs or the antennas to avoid vortex penetration in the first place [1]. Unfortunately this approach is accompanied by a strong increase of the SQUID inductance which may reduce the sensor performance yet again. Hence other possibilities to pin flux vortices without changing the SQUID inductance were investigated. It was reported that the preparation of normal conducting channels by ion beam irradiation [2] or local inserts of normal conducting materials [3,4] could lead to an enhanced flux pinning. The aim of our current work is to analyse the influence of self-organised gold nanoparticles on the critical current density of  $\text{YBa}_2\text{Cu}_3\text{O}_{7-\delta}$  (YBCO) thin films as well as the flux noise of gradiometers constructed from such modified YBCO films. We therefore prepared four planar galvanically coupled dc-SQUID gradiometers on one  $\text{SrTiO}_3$  bicrystal substrate and embedded

gold nanoparticles at well-defined positions to compare the different gradiometers among each other (see fig. 1).

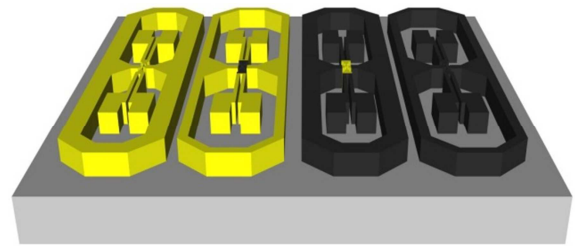


Fig. 1: Layout of the dc-SQUID gradiometers fabricated out of conventional (black) and gold modified YBCO (gold).

Prior to the growth of the superconducting thin film a gold layer was deposited on the substrates. During the subsequent preparation of the YBCO film gold nanoparticles evolve from the initial layer whereas the initial layer thickness determines the size of the particles. For particle sizes up to 50 nm we found those to be single crystalline. Scanning and transmission electron microscopy images showed a nearly homogeneous distribution of the gold crystals on the surface and within the YBCO layer itself (see fig. 2) so one can expect them to form additional and highly effective pinning centres.

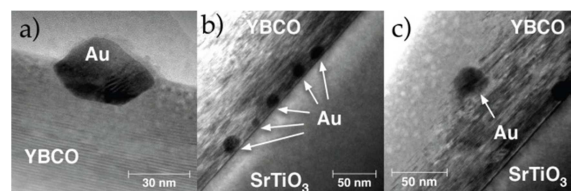
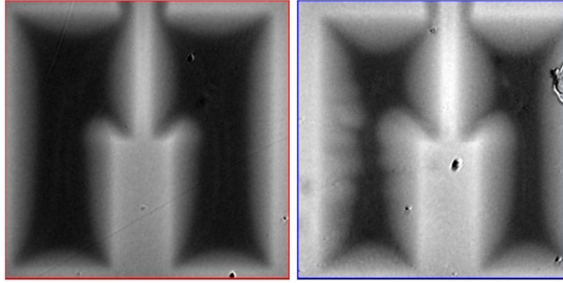


Fig. 2: The nanoparticles can be found a) on top of the YBCO layer, b) at the  $\text{SrTiO}_3$ -YBCO interface and c) within the YBCO itself.

Indeed we found a much smaller penetration depth of the magnetic flux in the Au modified areas which is evidence for an enhanced pinning of flux vortices.



**Fig. 3:** Flux density distribution in Au modified (left) and pure YBCO films (right) at  $B_{\text{ext}}=40\text{mT}$  and  $T=14\text{K}$  after zero-field-cooling. Black parts correspond to  $B=0\text{T}$ .

We used magneto-optical Faraday microscopy to map the flux density distribution in the superconducting lines of our gradiometers. Subsequently we calculated the local critical current density  $j_c$  via an inversion of the Biot-Savart law [5]. Using this method the temperature dependence of the critical current density was measured and plotted over the whole superconducting temperature range. As can be seen in fig. 4 we found a large enhancement of  $j_c$  (approximately 70% at 77K) for Au modified YBCO areas for all temperatures. Both curves exhibit the same shape so we suggest an additional pinning via Au particles. Although the obtained critical current den-

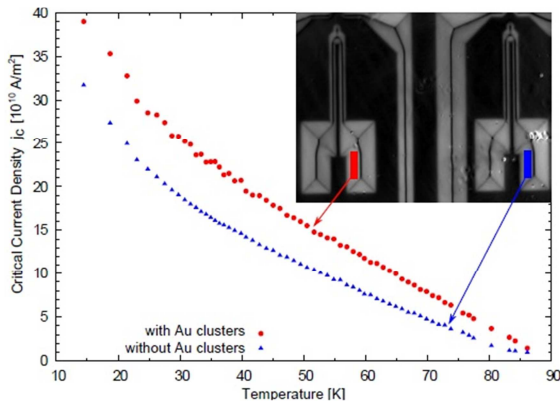


**Fig. 4:** Temperature dependence of  $j_c$  for Au modified and pure YBCO. The inset depicts the areas where the current density data was obtained from.

sities do not mark any record in the field of artificial pinning centres the inclusion of Au nanoparticles appears as the method of choice as it allows the adjustment of grain boundary properties at the same time [6]. Furthermore an additional pinning of flux vortices should not only result in an enhancement of  $j_c$  but also in a reduced flux noise of our dc-SQUID gradiometers. For this reason we carried out first measurements at  $T=77\text{K}$  in a locally shielded environment (single  $\mu$ -metal shield) using an ac-bias reversal technique [7]. Indeed we could achieve a white noise level of about  $5.5\mu\Phi_0/\sqrt{\text{Hz}}$  which is comparable to the best values we achieved for single dc-SQUIDS without antennas. For further information see [8].

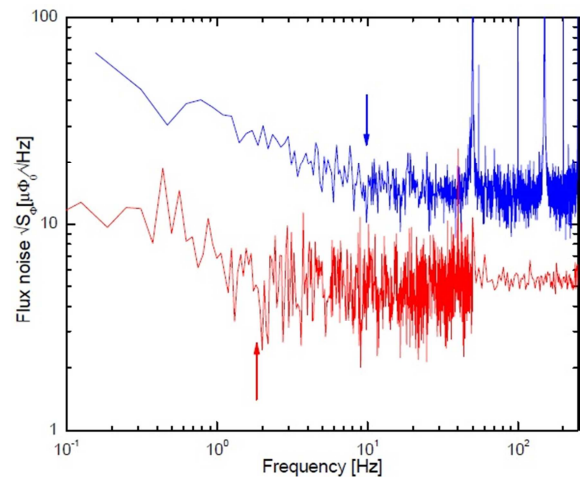


**Fig. 5:** Noise curve of an only antenna modified gradiometer (bottom) and a conventional gradiometer (top) of the same layout.

## References

- [1] E. Dansker et al., *Appl. Phys. Lett.* **70** (1997), 3267.
- [2] T. Schuster et al. *Phys. Rev. B* **47** (1993), 373.
- [3] P. Mikheenko et al., *J. Phys: Conf. Ser.* **234** (2010), 022022.
- [4] A. Kursumovic et al., *Supercond. Sci. Technol.* **22** (2009), 015009.
- [5] C. Jooss et al., *Rep. Prog. Phys.* **65** (2002), 651.
- [6] P. Michalowski et al., *Phys. Status Solidi – RRL* **5** (2011), 268.
- [7] dc-SQUID electronics SEL-1 by MAGNICON.
- [8] C. Katzer et al., *Europhys. Lett* **95** (2011) 68005.

# Investigations on dc-SQUIDs based on growth modified bi-crystal grain boundaries

P. Michalowski, D. Kuhwald, C. Katzer, F. Schmidl, and P. Seidel

Magnetic field sensors made of  $\text{YBa}_2\text{Cu}_3\text{O}_{7-\delta}$  (YBCO) have been studied by our group for about two decades. One key aspect are direct current superconducting quantum interference devices (dc-SQUIDs) based on bi-crystal grain boundary Josephson junctions.

The usability of dc-SQUIDs is strongly influenced by the transfer function  $V_\Phi$  or the modulation depth  $\Delta V$ . According to Il'ichev et al. [1,2]  $V_\Phi$  can be calculated as

$$V_\Phi = \frac{7I_C R_N}{\pi\Phi_0(1+\beta_L)} \left( 1 - 3.57 \frac{\sqrt{k_B T L_S}}{\Phi_0} \right), \quad (1)$$

where  $\beta_L = 2I_C L_S / \Phi_0$  is the SQUID parameter and  $\Phi_0$  is the flux quantum.  $I_C$ ,  $R_N$  and  $L_S$  are the critical current, the normal state resistance and the inductivity of the SQUID.

Regarding eq. (1), it would be preferable to use grain boundaries with high  $I_C R_N$  products, while the critical current density  $j_C$  is kept low to obtain a small  $I_C$ . To realize this, one possibility is to tune the SQUID parameters by ion beam etching after the patterning of the devices [3]. In our current work we are following another approach: adjusting the properties of bi-crystal grain boundary Josephson junctions by using gold nanocrystals [4].

We prepared our samples by depositing a thin gold layer of varying thickness – 3 and 5 nm – on a  $\text{SrTiO}_3$  bi-crystal substrate. During the following deposition of the YBCO film, gold nanoparticles evolve from the initial layer. In former scanning and transmission electron microscopy experiments we found these particles to be mono-

crystalline [5]. Furthermore the gold nanoparticles do not affect the superconducting properties of the YBCO layer in a negative way [6]. We subsequently used ion beam etching to produce a structure of similar dc-SQUIDs along the grain boundary (see fig. 1). This setup allows us to compare the effects of gold nanocrystals with different sizes on the superconducting parameters of the Josephson junctions and thereby the SQUID.

We measured the temperature dependence of  $I_C$  for the SQUIDs S2 (initial gold layer thickness of 3 nm) and S9 (5 nm). As fig. 2 shows  $I_C$  of S9 is smaller than that of S2 over the whole temperature range.

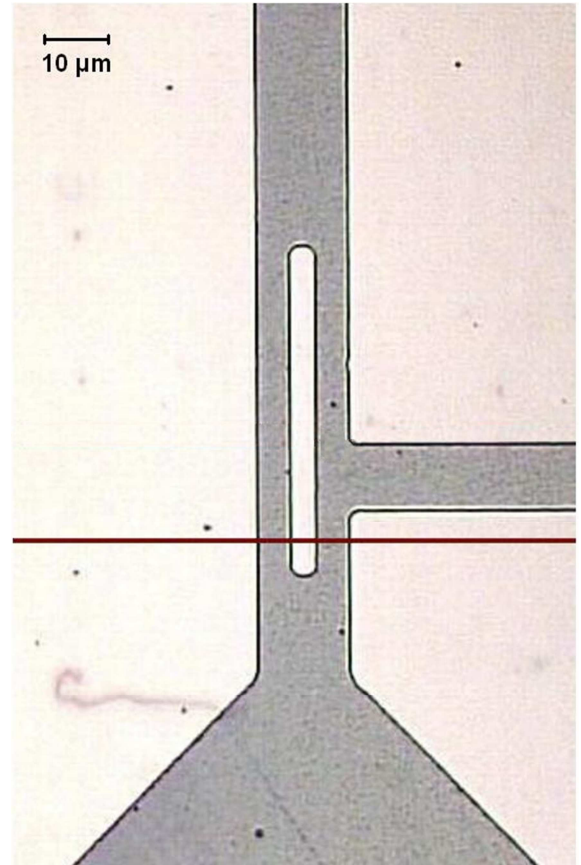


Fig. 1: Light microscope image of SQUID B109e S9. The line marks the grain boundary.

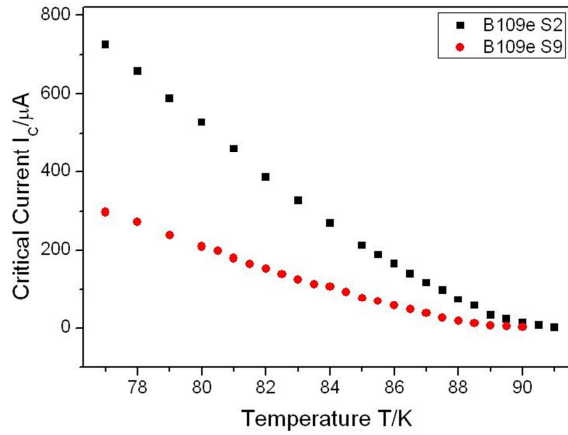


Fig. 2: Critical current  $I_c$  of SQUIDs B109e S2 and S9 depending on temperature  $T$ .

Both curves exhibit the typical behavior of grain boundary Josephson junctions in high- $T_c$  superconductors [7]. This indicates that the gold nanocrystals do not change the transport mechanism, whereas the value of the critical current is significantly different depending on the initial layer thickness. To study  $\Delta V$  we also exposed the SQUIDs to the varying magnetic field of a small coil and measured the dependence of the voltage  $V$  on the coil current  $I_{coil}$  for different bias currents  $I_B$ . We found modulations for SQUIDs with different initial gold thicknesses. An example can be seen in fig. 3.

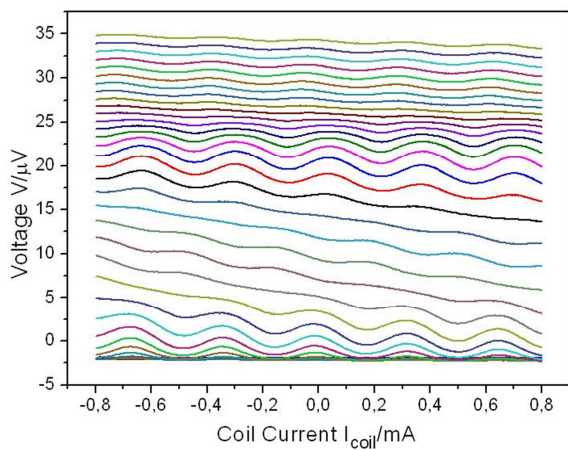


Fig. 3: Modulation curves of SQUID B109e S9 for bias currents  $I_B=190..780 \mu A$  at  $T=69 K$ .

To compare  $\Delta V$  of different SQUIDs we carried out modulation measurements for different temperatures and ascertained  $\Delta V$

for the respective  $I_B$ . Data for SQUID B109e S9 is given in fig. 4. and shows a higher maximum  $\Delta V$  for the SQUID with the larger initial gold layer. For all investigated SQUIDs  $\Delta V$  passes through several maxima and rises with smaller temperatures  $T$ . An interesting point is the shift of the maximum of  $\Delta V$  to the second and third peak with lower temperatures.

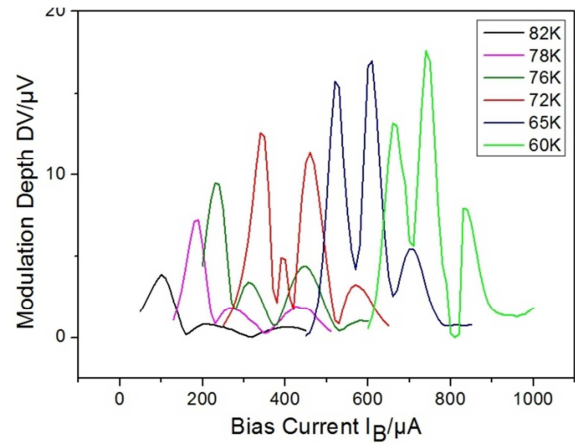


Fig. 4: Modulation depth  $\Delta V$  depending on bias current  $I_B$  of B109e S9 measured for different temperatures.

In the future we have to secure a broader basis for our conclusions. Furthermore we are going to investigate the effect of gold nanoparticles on the London penetration depth and thereby the SQUID inductance as well as on the noise characteristics of the devices.

## References

- [1] K. Enpuku et al., J. Appl. Phys. **73** (1993), 7929.
- [2] E. Il'ichev et al., Appl. Phys. Lett. **68** (1996), 708.
- [3] S. Wunderlich et al., Physica C **340** (2000), 51–64.
- [4] P. Michalowski et al., Phys. Status Solidi – RRL **5** (2011), 268.
- [5] V. Grosse et al., Phys. Status Solidi RRL **4** (2010), 97.
- [6] C. Katzer et al., Europhys. Lett **95** (2011), 68005.
- [7] H. Hilgenkamp et al., Rev. Mod. Phys. **74** (2002), 485–549.



# Josephson current second harmonic effects on magnetic flux in long junctions

P.Kh.Atanasova<sup>1</sup>, Yury Shukrinov<sup>2</sup>, E.V.Zemlyanaya<sup>2</sup>, and Paul Seidel

<sup>1</sup>University of Plovdiv, FMI, Plovdiv 4003, Bulgaria

<sup>2</sup>Joint Institute for Nuclear Research, Dubna, 141980, Russia

For the traditional JJ the current-phase dependence is a sinusoidal function. Such a model is described by the sine-Gordon equation. For a sufficiently wide class of JJ the superconducting Josephson current as a function of magnetic flux  $\varphi$  can be represented as a sine series [1]. It was recognized recently that the higher harmonics in this expansion are important in many applications. The interesting properties of LJJ with an arbitrarily strong amplitude of second harmonic in current phase relation were considered in [2]. Using only first two terms of the expansion (1) leads to the double sine-Gordon equation (2SG).

$$(1) \quad \begin{aligned} -\varphi' + a_1 \sin\varphi + a_2 \sin 2\varphi - \gamma &= 0, \\ x &\in (-l; l). \end{aligned}$$

Here and below the prime means a derivative with respect to the coordinate  $x$ . The magnitude  $\gamma$  is the external current,  $l$  is the semilength of the junction,  $a_1$  and  $a_2$  are the normalized amplitudes of the first and second harmonics of the Josephson current [1,3]. The boundary conditions for (1) have the form  $\varphi'(\pm l) = h_e$ , where  $h_e$  is external magnetic field. Stability and bifurcations of static solution  $\varphi(x, p)$ , where  $p = (l, a_1, a_2, h_e, \gamma)$  are analyzed on the basis of numerical solution of the corresponding Sturm-Liouville problem [4]

$$(2) \quad \begin{aligned} -\psi'' + q(x)\psi &= \lambda\psi, \quad \psi'(\pm l) = 0, \\ q(x) &= a_1 \cos\varphi + 2a_2 \cos 2\varphi. \end{aligned}$$

The minimal eigenvalue  $\lambda_0(p) > 0$  corresponds to the stable solution. In case  $\lambda_0(p) < 0$  solution  $\varphi(x, p)$  is unstable. The case  $\lambda_0(p) = 0$  indicates the bifurcation with respect to one of the parameters  $p$ . We characterize the solutions of equation (2) by number of fluxons  $N(p)$  which is

$$\text{defined as } N(p) = \frac{1}{2l\pi} \int_{-l}^l \varphi(x) dx.$$

The solutions with  $N[\varphi] = 1$  which are not  $\varphi = \pi$  at  $h_e = 0$  and  $\gamma = 0$  we denote as  $\Phi^1$ . The deformation of the  $\varphi'(x)$  of fluxon states under influence of the parameter  $a_2 \in [-1; 1]$  was considered in [5]. We observe a qualitative change in the local minima with decrease of  $a_2$  in the interval  $[-1; 0]$  and in the local maxima with increase of  $a_2$  in the interval  $[0; 1]$ . With change of the coefficient  $a_2$  the number of fluxons corresponding to the distribution  $\Phi^1$  is conserved [4] i.e.  $\partial N / \partial a_2 = 0$  and  $N[\Phi^1] = 1$ . As external magnetic field  $h_e$  is growing, more complicated stable fluxon with  $n = N[\varphi] = 2, 3, \dots$  appear which are denoted by  $\Phi^n$ .

The effect of the second harmonic contribution on  $\Phi^1$  was studied in [2,6,7]. It was shown [2] that taking into account at  $h_e = 0$  the second harmonics in current phase relation with  $a_2 < -0.5$  leads to the appearance of the “small” fluxon state additionally to the traditional “large” one. We call the solution at  $a_2 = -0.7$  in Fig. 1 as  $M_0$  (in [2] it is a “small” fluxon),

because  $N[M_0] = 0$ . Number of fluxons of “large” fluxon is equal to  $N[\text{large}] = 1$  and we denote it by  $\Phi^1$ . In [6], stability properties of “large” fluxon  $\Phi^1$  at nonzero  $h_e$  have been studied. Two coexisting stable  $\Phi^1$  like fluxons were demonstrated in some region of magnetic field. Here, we investigate this effect in case of two-fluxon and three-fluxon distributions.

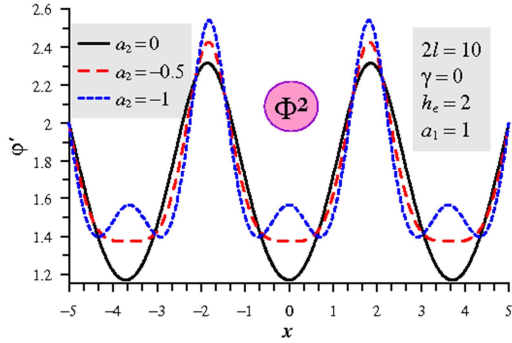


Fig. 1: Solutions at negative  $a_2$ .

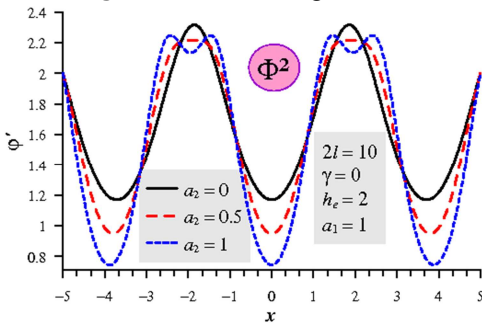


Fig. 2: Solutions at positive  $a_2$ .

In Fig. 2 the internal magnetic field of the two-fluxon distribution  $\Phi^2$  for  $2l = 10$ ,  $\gamma = 0$ ,  $h_e = 2$  and  $a_1 = 1$  at different  $a_2$  is presented. We observe a strong deformation of the fluxon distributions with decrease of  $a_2$  in the interval  $[-1; 0]$ . At  $a_2 = -0.5$  the curve of internal magnetic field  $\varphi'(x)$  has a plateau at the points  $x \approx -4$ ,  $x \approx 0$  and  $x \approx 4$ . Further increase of the absolute value of  $a_2$  leads to the transformation of these plateaus to local maxima of the internal magnetic field. Thus, accounting of the  $a_2$  contribution qualitatively changes a shape of the fluxon distribution  $\Phi^2$ . A similar deformation in the local maxima regions

(points  $x \approx -2$  and  $x \approx 2$ ) is observed for  $a_2 > 0$  (Fig. 2). We stress that the number of fluxons is conserved  $N[\Phi^2] = 2$  for all values  $a_2$ .

The two-fluxon solution  $\Phi^2$  in LJJ with  $2l = 10$  and  $\gamma = 0$  is stable at  $0.5 \leq h_e \leq 2.5$ . Qualitatively, the behavior of the curves  $\lambda_0(h_e)$  for this solution is similar to the case of one-fluxon solution  $\Phi^1$  [6]. The only difference is that in the  $\Phi^2$  case we don't have a region of coexistence of two stable branches that was observed for negative  $a_2$  in the  $\Phi^1$  case. For three-fluxon state at  $a_2 > 0.5$  new curves and coexistence of two different 3-fluxon states appears.

As summary we show that the second harmonic contributions significantly changes the shape and stability properties of trivial and fluxon static distributions in LJJ.

### Acknowledgments

We thank to E. Goldobin for the stimulating important suggestions. This research was partially supported by Heisenberg-Landau Program and by the project N111-FMI-004 (P.Kh.A).

### References

- [1] Golubov A A, et al. 2004 *Rev. Mod. Phys.* **76** 411-469
- [2] Goldobin E, Koelle D, Kleiner R and Buzdin A 2007 *Phys. Rev. B.* **76** 224523
- [3] P.Kh.Atanasova, T.L.Boyadjiev, Y U M Shukrinov, E.V.Zemlyanaya, P. Seidel 2010 *J. Phys. Conf. Ser.* **248** 012044.
- [4] Puzynin I V, Boyadzhiev T L, Vinitiskii S I, Zemlyanaya E V, Puzynina T P, Chuluunbaatar O 2007 *Physics of Particles and Nuclei* **38** 70–116
- [5] Atanasova P Kh, Boyadjiev T L, Shukrinov Yu M, Zemlyanaya E V, *LNCS* 6046, pp. 347-352. Springer, Heidelberg (2011)
- [6] Atanasova P Kh, Boyadjiev T L, Shukrinov Yu M, Zemlyanaya E V, *Fifth Int. Conf. on Finite Difference Methods: Theory and Applications*, 2010.

# Coherent radiation of self-heated Josephson junctions in the resonator

Alexander Grib<sup>1</sup> and Paul Seidel

<sup>1</sup> *Physics Department, Kharkiv V. N. Karazin National University, 61022, Kharkiv, Ukraine*

Recently, the immense progress in experiments on the detection of synchronized radiation from intrinsic Josephson junction arrays in high temperature superconductors (HTSC) was achieved [1]. It was supposed that the array of intrinsic junctions itself can be a geometrical resonator which determines the resonance modes for synchronization [1]. Experiments showed that the temperature along the samples of intrinsic Josephson junctions can be strongly inhomogeneous due to their self-heating by the extracted Joule heat [2].

We investigate these effects theoretically for the simplest system of the chain of two junctions embedded in the resonator. The resonator is presented as a sequential connection of the inductance  $L$ , the capacitance  $C$  and the resistance  $R$ . It is connected in parallel with the line which contains two Josephson junctions marked by indices  $i = 1, 2$ . The system of dynamic equations for phase differences  $\varphi_i$  of the order parameter across the  $i$ -th junction together with the equation for the current in the LRC resonance contour is as follows:

$$C_i \frac{\Phi_0}{2\pi} \frac{d^2 \varphi_i}{dt^2} + \frac{\Phi_0}{2\pi R_{Ji}} \frac{d\varphi_i}{dt} + I_{ci} \sin(\varphi_i) + \frac{dq}{dt} = I_b$$

$$L \frac{d^2 q}{dt^2} + R \frac{dq}{dt} + \frac{q}{C} = \frac{\Phi_0}{2\pi} \left( \frac{d\varphi_1}{dt} + \frac{d\varphi_2}{dt} \right),$$

(1a,b)

where  $I_{ci}$ ,  $C_i$  and  $R_{Ji}$  are the critical current, the capacitance and the resistance of the  $i$ -th junction, correspondingly,  $q$  is the charge on the capacitor  $C$ ,  $I_b$  is the bias current,  $t$  is the time and  $\Phi_0 = 2.07 \cdot 10^{-15}$  Wb is the quantum of magnetic flux. Critical voltages at the temperature of the cryo-

stat  $T_{cr}$  are assumed to be the same:

$$V_{c1}(T_{cr}) = V_{c2}(T_{cr}) = V_c(T_{cr}).$$

The estimate of self-heating of the junctions above  $T_{cr}$  can be made with the use of the Fourier law of the stationary heat flux:

$$\Delta T_i = \gamma_i P_i, \quad (2)$$

where  $\Delta T_i = T_i - T_{cr}$  with  $T_i$  as the temperature of the  $i$ -th junction,  $P_i$  is the power of

the Joule heat extraction and  $\gamma_i \approx \frac{r_i}{\lambda A_i}$  is

the coefficient which characterizes the heat sink with  $\lambda$  as thermal conductivity,  $A_i$  as the area of the junction and  $r_i$  as the distance at which the temperature becomes equal to  $T_{cr}$ . We suppose that  $\gamma_1 = \gamma_2 = \gamma$ . The power of Joule heat extraction is than

$$P_i = \left\langle \frac{\Phi_0}{2\pi} \frac{d\varphi_i}{dt} \left( I_b - \frac{dq}{dt} \right) \right\rangle, \quad (3)$$

where the sign  $\langle \dots \rangle$  means averaging over large interval of time. Close to the critical temperature, the temperature dependence of the critical voltage can be expanded to [3]:

$$V_{ci}(T_i) = V_{ci}(T_{cr}) - \gamma \left| \frac{dV_c}{dT} \right| P_i. \quad (4)$$

Supposing  $R_{Ji}(T) \approx const.$ , we can solve the system Eqs.(1)-(4) self-consistently and find IV-curves of self-heated junctions. We chose values  $|dV_{ci}/dT| = 1.63 \cdot 10^{-4}$  V/K,  $A_{1,2} = 10^{-12}$  m<sup>2</sup>,  $\lambda = 8$  W/(m·K),  $r_{1,2} = 10^{-7}$  m,  $I_{c1}(T_{cr}) = 15.4$  mA,  $I_{c2}(T_{cr}) = 15.0$  mA,  $V_c = 2 \cdot 10^{-3}$  V,  $C_1 = 12.7$  pF,  $C_2 = 12.4$  pF,  $C = 1$  pF,  $L = 90$  fH,  $R = 1 \cdot 10^{-3}$  Ohm.

Calculated IV-characteristics of self-heated junctions are presented in Fig. 1. The obtained curve coincides with the IV-

characteristics of junctions without self-heating in the regions of resonance steps.

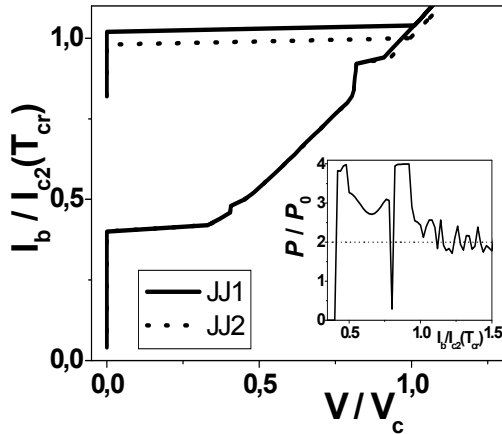


Fig. 1: IV-characteristics of self-heated junctions in the resonator. Inset: the normalized ac power of radiation of the whole chain plotted on the normalized bias current.

In inset we show the normalized ac power of radiation of the whole chain  $P/P_0$  [4]. For two junctions this value is equal to 4 if junctions radiate coherently [4]. It is seen from Fig. 1 that the value  $P/P_0 = 4$  is reached in the regions of the resonant steps. The temperatures of overheating of junctions are shown in Fig. 2.

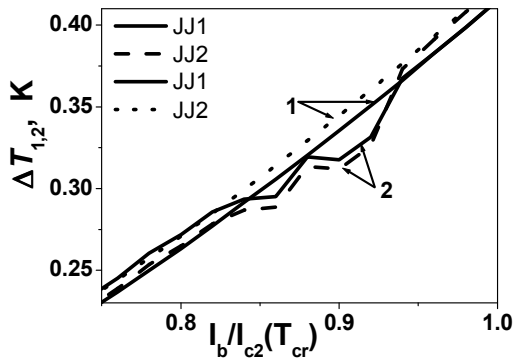


Fig. 2: Dependences  $\Delta T_{1,2} = f(I_b / I_{c2}(T_{cr}))$  for self-heated junctions without the resonator (1) and with the resonator (2).

These plots show some particularities at bias currents corresponding to the resonant step. It is seen from Eqs. (2), (3) that at the current resonance due to the large negative term  $dq/dt$  in Eq. (3) the value of  $\Delta T_i$  be-

comes smaller than that calculated for the junction without the resonator [5]. If there is the voltage resonance, then due to the increase of the voltage in Eq. (3) the value of  $\Delta T_i$  becomes large. These particularities are observed in Fig. 2. To make particularities clear, we plotted the difference  $\delta T_i$  between values of  $\Delta T_i$  obtained for junctions in the resonator and for junctions without the resonator (Fig. 3).

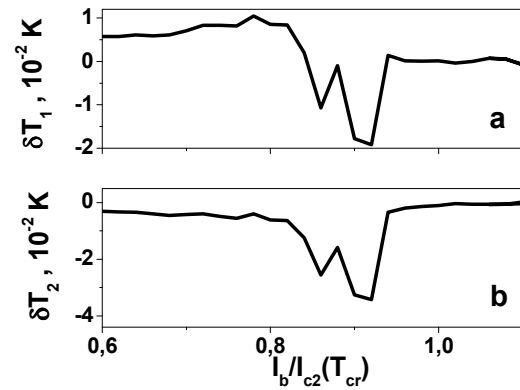


Fig. 3: Dependences  $\delta T_{1,2} = f(I_b / I_{c2}(T_{cr}))$  for junctions 1 (a) and 2 (b).

However, these effects produce the change in the temperature which is one order of magnitude smaller than the main effect of the Joule heat extraction produced by the direct current (see Fig. 2).

In conclusion, we calculated IV-characteristics of self-heated Josephson junctions and showed that self-heated junction can be synchronized. Overheating of junctions is produced by the resonator and it is a order of magnitude smaller than changes produced by the direct current.

## References

- [1] L. Ozyuzer et al., Science 318, (2007) 1291
- [2] C. Kurter et al., IEEE Trans. Appl. Supercond. 19 (2009) 428
- [3] K. K. Likharev, Dynamics of Josephson junctions and Circuits (Gordon and Breach, Philadelphia, 1991)
- [4] A. N. Grib, P. Seidel, and J. Scherbel, Phys. Rev. B 65, (2002) 094508
- [5] A. Grib, P. Seidel, Elektronika 6, (2011) 26-27

## Weak continuous monitoring of a flux qubit - resonator system with intermediate coupling

G. Oelsner<sup>1</sup>, P. Macha<sup>1</sup>, M. Grajcar<sup>2</sup>, O. Astafiev<sup>3</sup>, A.N. Omelyanchouk<sup>4</sup>, B. Ivanov<sup>1</sup>, U. Hübner<sup>1</sup>, S. Anders<sup>1</sup>, E. Il'ichev<sup>1</sup>, and H.-G. Meyer<sup>1</sup>

<sup>1</sup>*Institute of Photonic Technology, PO Box 100239, D-07702 Jena, Germany*

<sup>2</sup>*Department of Solid State Physics, Comenius University, SK-84248 Bratislava, Slovakia*

<sup>3</sup>*B. Verkin Institute for Low Temperature Physics and Engineering, 47 Lenin Avenue, 61103 Kharkov, Ukraine*

<sup>4</sup>*NEC Nano Electronics Research Laboratories, Tsukuba, Ibaraki, 305-8501, Japan*

Artificial quantum systems are more and more in use in different fields of modern physics. One important example are superconducting circuits at very low temperatures, which have been demonstrated to show quantum mechanical behavior. The advantage of these systems over natural quantum systems (like atoms or spins) is their high level of controllability and scalability. Despite the use of such systems as basic blocks for possible quantum computation also general quantum mechanical effects can be shown. Especially the field of cavity quantum electrodynamics (cQED) opens a wide range of possible experiments.

In general cQED studies the coherent interaction of a photon field, described as a quantum oscillator, with a two level system [1]. Solid state cQED based on superconducting circuits has been suggested [2] and demonstrated [3,4] using superconducting qubits coupled to a superconducting transmission line resonator.

To observe the coherent dynamics of the system the coupling strength  $g$  should exceed the rates of incoherent processes, namely the qubit dephasing  $G$  and the resonator relaxation  $k$ . This is the condition for the so called strong coupling regime.

On the other hand the resonator itself can be used to read out the state of the qubit [5]. In the so called dispersive regime, when the eigenfrequency of the qubit is well de-tuned from the resonator, even quantum non demolition (QND) measurements can be performed. Here the center frequency of the

resonator encodes the information of the qubit state. The readout can be performed in a weak continuous [3,6] or pulsed mode [5].

In order to minimize the backaction of the resonator to the qubit the coupling constant can be decreased. However, to avoid the performance degradation of the resonator as detector the condition  $g \gg k$  should be fulfilled.

We test experimentally an intermediate coupling where  $g \gg k$  but  $g \sim G$  [7].

The resonator is fabricated as coplanar waveguide with a fundamental, half wavelength, mode of 2.5 GHz. The loss rate was determined by measuring the quality factor and found to be  $k/2\pi = 130$  kHz. The superconducting flux qubit is placed at the center of the resonator. Here the amplitude of the current and therefore the magnetic field from the fundamental mode reaches its maximum and therefore optimal coupling to the qubit can be achieved. The coupling constant was estimated by the geometric structure to be  $g = 3$  MHz.

The qubit resonator system is described in the flux basis by the Hamiltonian

$$H = \frac{h\varepsilon(\Phi_x)}{2} \sigma_z + \frac{h\Delta}{2} \sigma_x + h\nu_r a^\dagger a + hg \sigma_z (a^\dagger + a),$$

where  $D$  is tunnel splitting of the qubit,  $s_{x,z}$  are the Pauli matrices,  $a^\dagger$  ( $a$ ) is the photon creation (annihilation) operator and  $h\varepsilon(\Phi_x) = 2F_0 I_p (1 - \Phi_x / \Phi_0)$  is the energy bias of the qubit. This value is defined by the persistent current  $I_p$  in the qubit loop and the external dc magnetic flux  $\Phi_x$ ;  $\Phi_0$  is the magnetic flux quantum. The Hamiltonian can

be rewritten in the eigenbasis of the qubit

$$H = \frac{h\nu_q}{2} \sigma_z + h\nu_r a^\dagger a + hg_\varepsilon \sigma_x (a^\dagger + a),$$

where we neglected the small diagonal term  $g_D (a^\dagger + a) s_z$ . The energy splitting of the qubit is then given by  $h\nu_q = \sqrt{\varepsilon^2 + \Delta^2}$ . Furthermore we find the normalized coupling as  $g_e = g_D / h\nu_q$ . By measuring the transmission through the qubit resonator system the eigenenergies of the system can be probed (Fig.1(a)).

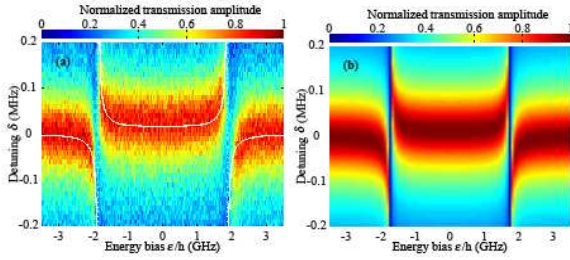


**Fig.1:** a) Normalized transmission amplitude of the resonator as a function of the qubit energy bias  $e$  and the driving frequency. The data was measured at a nominal temperature of the mixing chamber below 20 mK, ensured  $k_B T \ll h\nu_q, h\nu_r$ . The calculated frequencies of the lowest photon transition in the qubit-resonator system are depicted as white solid lines. b) Theoretical calculations. The number of photons is taken to be less than one, other parameters are taken from the experiment.

We also calculated the transmission through the system by analyzing the Makrovian Master equation for the density matrix  $\rho$ ,  $\dot{\rho} = -i/h[H, \rho] + L(\rho)$ . Here  $L = L_r + L_q$  includes the two incoherent processes: dissipation in the resonator (photon decay) and qubit decoherence: relaxation with rate  $G_1$  and pure dephasing with rate  $G_f$ . The total dephasing rate  $G$  was used as fitting parameter and found to be 0.26 MHz (Fig.2b).

The qubit parameters are found in another part of the experiment. For that a second Microwave tone is applied to the system. If the frequency of the qubit and the resonator are well de-tuned (in the dispersive limit) the systems Hamiltonian can be transformed to

$$H \approx h \left( \nu_r + \frac{g_\varepsilon^2}{\delta} \sigma_z \right) a^\dagger a + \frac{h}{2} \left( \nu_q + \frac{g_\varepsilon^2}{\delta} \right) \sigma_z,$$

In that form we find the influence of the qubit to the resonator as a small ac Zeeman shift of

the size  $g_e^2 / d s_z$ , where  $d = \nu_r - \nu_q$  is the detuning between resonator and qubit.

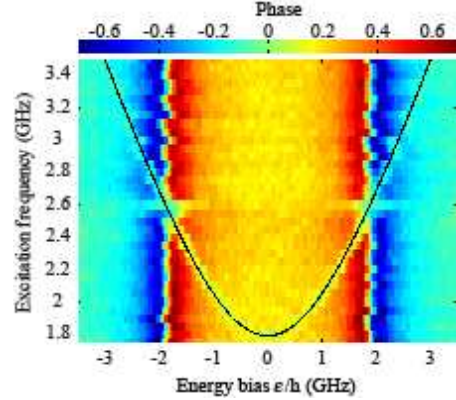


**Fig.2:** Transmission phase of the resonator as a function of the mw frequency and the energy bias  $e$ . The black line depicts the fitted energy level splitting of the qubit.

If the high frequency tone matches the eigenfrequency of the qubit, its levels get equally populated. This yields the vanishing of the shift (Fig.3). Therefore the qubit parameters are directly accessible and found to be  $D = 1.8$  GHz and  $I_p = 180$  nA.

In conclusion we note that even in the regime of intermediate coupling  $g \sim G$  coherent interaction between resonator and qubit can be observed. Furthermore a complete characterization of the qubit can be done by spectroscopic measurements and fitting the experimentally observed transmission.

## Acknowledgments

We gratefully acknowledge the financial support of the EU through Solid project. B.I. acknowledges the partial support of the DAAD.

## References

- [1] J. M. Raimond, et al., Rev. Mod. Phys. **73**, 565 (2001)
- [2] A. Blais, et al., Phys. Rev. A **69**, 062320 (2004).
- [3] A. Wallraff, et al., Nature **431**, 162 (2004).
- [4] A. A. Abdumalikov, Jr., et al., Phys. Rev. B **78**, 180502(R) (2008).
- [5] R. Bianchetti, Phys. Rev. A **80**, 043840 (2009).
- [6] M. Grajcar, et al., Phys. Rev. B **69**, 060501(R) (2004).
- [7] G. Oelsner, et al., Phys. Rev. B **81**, 172505 (2010)

# Cryogenic Current Comparator for FAIR

R. Geithner\*, F. Kurian\*\*, R. Neubert, W. Vodel\*, and P. Seidel

\*Helmholtz-Institut Jena, Fröbelstieg 3, D-07743 Jena

\*\*GSI Helmholtzzentrum für Schwerionenforschung GmbH, Planckstraße 1, D-64291 Darmstadt

For the recently launched FAIR (Facility for Antiproton and Ion Research) project [1] at GSI Darmstadt an improved Low Temperature dc Superconducting Quantum Interference Device (LTS SQUID) based Cryogenic Current Comparator (CCC) for non-contact monitoring of low intensity particle beams should be developed.

The sensitivity ultimately depends on the pickup coil. It was demonstrated [2] that the use of a ferromagnetic core leads to a possible optimization for better noise performance using materials with a high relative permeability  $\mu_r$  and therewith a high inductance factor for given coil dimensions.

Referring to our measurements [2] three Nanoperm M764 cores delivered from the manufacturer Magnetec [3] with the final dimensions were ordered and characterized at the GSI. The temperature and frequency dependent inductance  $L_S(\nu)$  and the serial resistance  $R_S(\nu)$  were measured with an Agilent E4980A LCR-Meter at 4.2 K and had shown that these cores fulfill our requirements [4] (see Fig. 1, curve a – c). Compared to the low temperature properties of the pickup coil (see Fig. 1, curve d) of the successfully tested CCC for dark current measurements in a former project together with DESY (DESY-CCC) [5] we see a four times higher inductance factor which is less frequency dependent (see Fig. 1). The core material used for DESY-CCC pickup coil was Vitrovac 6025F from the manufacturer Vacuumschmelze Hanau [6]. Beneath this the noise contribution of the cores should also be evaluated. These measurements should be carried out with a

LTS-DC-SQUID [7] based noise measurement equipment.

Because of the high sensitivity against magnetic fields the SQUID and the coil have to be carefully shielded.

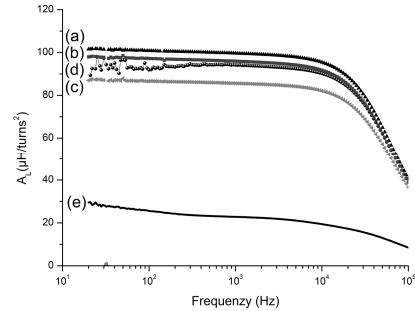


**Fig. 1:** Inductance factor  $A_L$  at 4.2 K of Nanoperm M-764-01 core 2 (a), core 3 (b), core 1 (c) with normal conducting multi-turn winding and core 2 (d) with superconducting single-turn winding as well DESY-CCC pickup coil (Vitrovac 6025F) with superconducting single-turn winding (e).

Beside the direct measurement it is also possible to evaluate the noise contribution of the cores by using the Fluctuation-Dissipation-Theorem (FDT) [8]. Using the FDT you can calculate the current noise spectral density (PSD\_I) from the results of the measurements of the frequency dependent inductance  $L_S(\nu)$  and serial resistance  $R_S(\nu)$  of coils including these cores with an LCR-Meter. These measurements could be done in an unshielded test setup in contrast to the noise measurements using SQUID measuring technique.

To measure the noise contribution of the cores with a SQUID noise measurement equipment a single turn superconducting winding is applied to the core and connected to the input coil of the SQUID. To compare the measurements with the predictions of the FDT you have to take the input coil of the SQUID sensor  $L_{SQUID}$  into account

for the calculation. Because there is any core material in the superconducting input coil of the SQUID the frequency dependence and the serial resistance could be neglected.

$$PSD_{-I} = 4k_B T \frac{R_s(\nu)}{(2\pi\nu(L_{SQUID} + L_s(\nu)))^2 + (R_s(\nu))^2} \quad (1)$$

As one can see in Equation (1) the serial resistance  $R_s(\nu)$  of the characterized coil is very dominant for low frequencies. In the case of the CCC the pickup coil has a single-turn superconducting winding. For the characterization of the cores at GSI multi-turn normal conducting windings were used to reach a higher total inductance. This results in a higher serial resistance which leads to a higher calculated noise. To get the accurate serial resistance for the future pickup coil these measurements had to perform again with a single-turn superconducting winding.

To be able to characterize the cores, the welded pickup coils and the completed CCC in Jena a new wide neck cryostat was commissioned. It has a diameter of 400 mm with an usable helium level of 860 mm. The operating time is about three days even for large samples.

The LCR-Meter measurements with the single-turn superconducting coil verify the inductance factors from the characterization at the GSI (see Fig. 1, curve e). Because of the lack of a superconducting shielding for the toroidal coils with the Nanoperm cores there are no direct noise measurements using a SQUID possible yet. In the case of the DESY-CCC the inductance and the serial resistance of the single-turn superconducting pickup coil as well as its current noise was measured. The results from FDT showed a good agreement with the measurements (see Fig. 2; curve a, b).

From FDT we calculate a three till six time lower current noise for Nanoperm M-764 (see Fig. 2, curve c) compared to the previ-

ous DESY-CCC pickup coil with a Vitrovac 6025F core.

The white current noise of such a coil is  $2.5 \text{ pA/Hz}^{1/2}$  only and seems to be limited by the SQUID noise (see Fig. 2, curve (d)). The total noise in the frequency range from 20 Hz up to 10 kHz would be reduced by a factor of 3.1 to 28 nA compared to 87 nA for the DESY-CCC pickup coil.

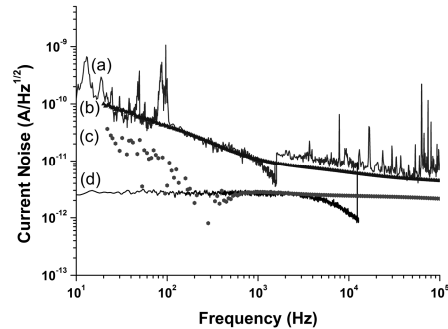


**Fig. 2:** Measured current noise of the DESY-CCC pickup coil (a) and the SQUID (d) as well as the calculated current noise from FDT of the DESY-CCC pickup coil (b) and Nanoperm M-764 core 2 (c).

The next step is to measure the current noise of the Nanoperm M764 cores and to compare these results with the prediction of the FDT. This will be followed by the characterization of the completed CCC.

The improvements of the noise contribution together with some constructional changes should lead to a 3 times better sensitivity and a much better reduction of the currently seen mechanical interferences [5].

## References

- [1] Facility for Antiproton and Ion Research (FAIR), homepage available: <http://www.gsi.de/fair/>
- [2] R. Geithner et al., IEEE Trans. Appl. Supercond., 21 (2011) 3, 444 - 447
- [3] MAGNETEC GmbH, Industriestrasse 7, D-63505 Langenselbold, Germany
- [4] R. Geithner et al., Proc. of DIPAC 2011, TUPD66, pp. 458 – 460, Hamburg, Germany
- [5] R. Geithner et al., Rev. Sci. Instrum. 82 (2011), 013302
- [6] VACUUMSCHMELZE GmbH & Co. KG, Gruener Weg 37, D-63450 Hanau, Germany
- [7] W. Vodel, K. Mäkinen, Meas. Sci. Technol., 3 (1992), 1155-1160.
- [8] H.P. Quach, T.C.P. Chui, Cryogenics 44 (2004)6, 445



## SQIF-based dc SQUID amplifier with intrinsic negative feedback

T. Schönau, M. Schmelz, V. Zakosarenko, R. Stolz, S. Anders, L. Fritzsich and H.-G. Meyer

*Institute of Photonic Technology, PO Box 100239, D-07702 Jena, Germany*

We report on a two-stage setup, composed of a dc SQUID magnetometer coupled to a superconducting quantum interference filter (SQIF) [1, 2, 3, 4] which acts as a low noise cryogenic amplifier. The cryogenic amplification facilitates the readout by reducing the requirements on the room temperature flux-locked loop (FLL) electronics [5, 6]. Furthermore, it is possible to feed back part of the bias current of the SQIF to the input stage dc SQUID to obtain an on-chip linearization of the voltage-flux-characteristic.

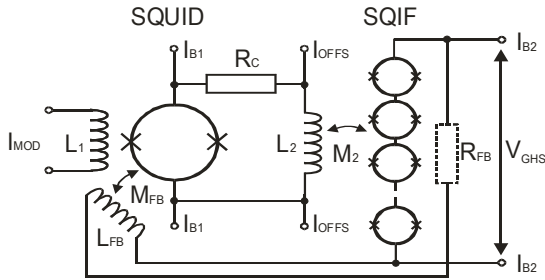


**Fig.1:** Circuit diagram of the two-stage setup containing the input stage SQUID and the SQIF. If the resistor  $R_{FB}$  is used, the on-chip linearization is applied.

The circuit diagram of the two stage SQUID-SQIF system is shown in figure 1. The input stage dc SQUID, in this case a magnetometer, is inductively coupled via the resistor  $R_C$  to the input coil of the SQIF.  $R_C$  is adjusted in the range of 1...2  $\Omega$  to limit the current modulation to about 80 % of the SQIF slope. An additional dc current  $I_{OFFS}$  is used to trim the operating point to the centre of the maximum slope of the SQIF transfer characteristic. The resulting  $V-\Phi$  characteristic of the two-stage system is SQUID-like but exhibits an increased voltage swing in the millivolt range. Accordingly, the setup is denoted as

Großhub-SQUID (GHS). If the optional feedback resistor  $R_{FB}$  is used, a part of the SQIF bias current  $I_{B2}$  couples inductively via the feedback coil  $L_{FB}$  to the SQUID. This on-chip feedback linearizes the system response as depicted in figure 2. If the flux in the GHS exceeds the stability range of  $\pm\Phi_0/4$ , the feedback becomes positive and jumps of  $\pm 1\Phi_0$  to the next stable point occur. We could demonstrate that these flux jumps can be reconstructed by post processing, which enables the measurement of magnetic fields with a practically unlimited dynamic range [7]. A further advantage is that the feedback path is significantly reduced compared to a conventional room temperature FLL. Thus, an increase in bandwidth can be expected [8].

The fabrication of the input stage dc SQUID sensors and the SQIFs is based on standard all-refractory Nb/AIO<sub>x</sub>/Nb technology developed at IPHT [9, 10]. The input stage SQUID is designed as second-order gradiometer with an inductance of  $L_{SQ} \approx 300$  pH. It is inductively coupled to a square magnetometer pickup loop with an outer diameter of 9.2 mm. The effective area of this magnetometer was measured inside a Helmholtz coil to be about 3.0 mm<sup>2</sup>.

The typical sensor parameters are: screening parameter  $\beta_L = 2\pi I_C L / \Phi_0 \approx 5.2$ , McCumber parameter  $\beta_C = 2\pi I_C R_N^2 C / \Phi_0 \approx 0.9$  and voltage swing  $\Delta V_1 \approx 70$   $\mu$ V at a bias current  $I_{B1} \approx 35$   $\mu$ A. In magnetically shielded environment an equivalent white flux noise of  $\Phi_n \approx 3.5$   $\mu\Phi_0/\text{Hz}^{1/2}$ , corresponding to a magnetic field

resolution of  $2.4 \text{ fT/Hz}^{1/2}$ , was measured. The sensor has two coils coupled to the pickup loop to enable separate flux modulation and feedback. Currents of  $1.95 \text{ }\mu\text{A}$  and  $3.0 \text{ }\mu\text{A}$  generate one flux quantum in the SQUID loop via  $L_1$  and  $L_{\text{FB}}$ , respectively.

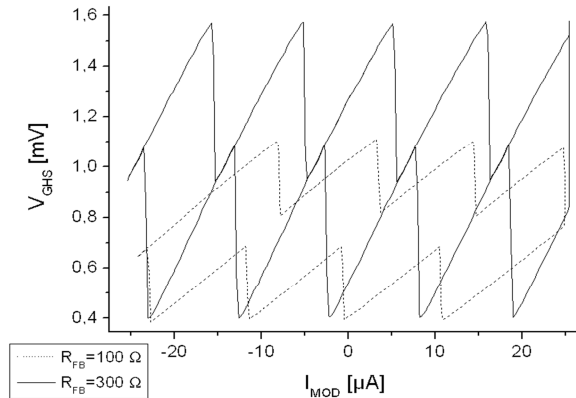


**Fig.2:** Influence of the feedback resistance  $R_{\text{FB}}$  on the  $V$ - $\Phi$  characteristic of the on-chip linearized GHS. The upper (lower) part of each characteristic corresponds to an increasing (decreasing) modulation current  $I_{\text{MOD}}$ .

The SQIF is formed by a series connection of  $N = 56$  SQUIDS. Their inductances are spread homogeneously between  $65 \text{ pH}$  and  $200 \text{ pH}$ . The SQUIDS are designed as first order series gradiometers. This ensures an operation independent of homogenous external magnetic fields like the Earth's field. For an adequate on-chip linearization, a high feedback current is required. For this purpose, a chip design with a parallel connection of four of the above mentioned SQIFs (denoted as  $4x\text{SQIF}$ ) has been realized. Thereby, the SQIF input coils are connected in series. Voltage swings of  $2.25 \text{ mV}$ ,  $1.9 \text{ mV}$  and  $1.4 \text{ mV}$  could be demonstrated for a SQIF, a  $4x\text{SQIF}$  and the whole GHS-setup without on-chip feedback, respectively. Theoretical considerations as well as noise measurements in RF-shielded environment proved, that the spectral flux noise of the GHS-setup without on-chip feedback is dominated by the input stage dc SQUID,

even if a room temperature FLL electronics with moderate voltage and current noise is used for the readout [7].

If the on-chip feedback is applied, the transfer function  $V_{\Phi}$  is reduced and thus the noise contribution of the room temperature amplifier increases [7]. The feedback strength and hence the reduction of  $V_{\Phi}$  can be adjusted by the feedback resistor  $R_{\text{FB}}$ . Thus, a compromise has to be found between linearity and noise enhancement. A way to increase  $V_{\Phi}$  without reducing the feedback strength is to realize the setup with sub-micron cross-type Josephson tunnel junctions [11, 12, 13] which will be further investigated.

## Acknowledgments

We thank Prof. Paul Seidel for his guidance and helpful instructions.

## References

- [1] Oppenländer J, Häussler Ch and Schopohl N 2000 Phys. Rev. B 63
- [2] Häussler Ch, Oppenländer J and Schopohl N 2001 J. Appl. Phys. 89
- [3] Oppenländer J, Zakosarenko V, Schultze V and Ijsselsteijn R. 2004 PCT/DE2003/ 002582
- [4] Zakosarenko V, Stolz R, Meyer H.-G. 2009 PCT/DE2009/001655
- [5] Welty R P and Martinis J M 1991 IEEE Trans. Magn. 27 2924-26
- [6] Welty R P and Martinis J M 1993 IEEE Trans. Appl. Supercond. 3 2605-08
- [7] T Schönau et al 2012 Supercond. Sci. Technol. 25 015005
- [8] Drung D and Mück M 2004 "SQUID electronics" SQUID Handbook, ed Clarke J and Braginski A I (Weinheim: WILEY-VCH) 127-170
- [9] Stolz R, Fritzsche L and H.-G. Meyer 1999 Supercond. Sci. Technol. 12 806-808
- [10] <http://www.fluxonics-foundry.de>, 2009
- [11] S Anders et al 2009 Supercond. Sci. Technol. 22 064012
- [12] M Schmelz et al 2011 Supercond. Sci. Technol. 24 065009
- [13] T Schönau et al 2011 ESNF Issue 18 STP 278 <http://www.ewh.ieee.org/tc/csc/europe/newsforum/pdf/KRYO-Schonau.pdf>

# Spatial resolved Magnetorelaxometry in combination with toxicological characterization of magnetic nanoparticles

M. Büttner, S. Hanitsch, I. Seyfarth<sup>1</sup>, U. Enke<sup>1</sup>, F. Schlenk<sup>3</sup>, C. Bergemann<sup>5</sup>, A. Csaki<sup>4</sup>, D. Fischer<sup>3</sup>, R. Bräuer<sup>2</sup>, E. Schleussner<sup>1</sup> and P. Seidel

<sup>1</sup> Department of Obstetrics and Gynecology, Placentalarbor Jena University Hospital, Friedrich-Schiller-University Jena, Germany

<sup>2</sup> Institute of Pathology, Jena University Hospital, Friedrich-Schiller-University Jena, Germany

<sup>3</sup> Department of Pharmaceutical Technology, Institute of Pharmacy, Friedrich-Schiller-University Jena, Germany

<sup>4</sup> Institute of Photonic Technology (IPHT), Jena, Germany

<sup>5</sup> Chemicell GmbH, Berlin, Germany

Based on the approach of Romanus et al. [1] a feasibility study was conducted whether the use of spatial Magnetorelaxometry(MRX) is able to gain additional information from toxicological placenta perfusion studies with magnetic nanoparticles.

Placenta perfusion is an established tool to determine whether substances are able to overcome the blood-placenta-barrier and are therefore transferred from the maternal blood cycle to the unborn child's. Therefore a vital postnatal human placenta is perfused in a simulated "maternal" circulation in which the substance of interest is added and a simulated "fetal" circulation [2] as shown in Fig. 1.

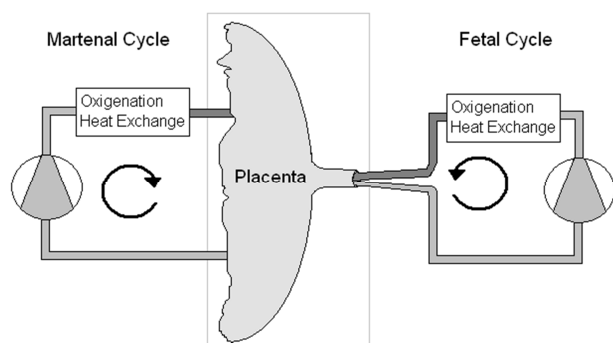


**Fig.1:** Basic principle of placenta perfusion essay as conducted in the placenta laboratory at the Friedrich-Schiller-University-Hospital.

By examination of the perfusion solution probed from the artificial "fetal" cycle the amount of substance which has been able to cross the blood-placenta-barrier can be determined [2]. Farther it is of interest how much of the substance is enriched within the placenta itself and if there is a distribution pattern detectable.

Hence the perfused placenta needs to be examined by micro biochemical or microscopic methods. Those are mostly destructive methods and require a complex set of sample preparation. If magnetic nanoparticles are to be examined with the placenta perfusion method the detection by means of the magnetic properties is obvious. Thus the SQUID-based Magnetorelaxome [4] trylocated at the institute of solid state physics was tested as novel tool in perfused placenta sample examination in the context of toxicological studies on magnetic nanoparticles.

The used magnetic nanoparticles were delivered in a multicore configuration. This required determining specific parameters for the device in conjunction with this kind of particles for applicable concentrations. For the quantization of magnetic nanoparticles a standardized sample configuration based on agarosegel has been established and calibration curves

have been measured for different particle systems.

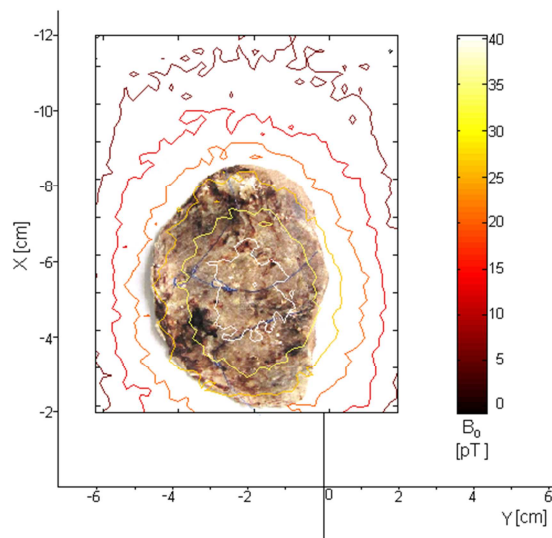


**Fig. 2:** Spatial resolved MRX scan merged with a photograph of a perfused placenta sample showing a rough distribution pattern of the magnetic flux density measured over the sample in pT related to the quantity of magnetic particles applied to the

The use of freeze-dried placenta samples for the detection of distribution pattern with 2D-MRX scans (as shown in Fig. 2) has been studied. Necessary improvement, within the apparatus depended limits, have been achieved by additional signal processing and sample preparation.

Although the spatial resolution of the system has been proven as not sufficient to detect a finer pattern of distribution, the nanoparticles could be detected with a high sensitivity and semi-quantitative estimations could be made which agreed with measurements of the respective perfusion solution samples.

So spatial resolved MRX measurement can, in principle, be used to examine

samples from placenta perfusion essays but requires additional systemic development as special sample configurations to reach its full capability.

### Acknowledgment

This work has been funded by the BMBF Project “NanoMed” and has been a cooperation between the placenta laboratory of the Friedrich-Schiller-University-Hospital and the institute of solid state physics.

### References

- [1] E Romanus; M Hückel; C Groß; S Prass; W Weitschies; R Bräuer; P Weber (2002): Magnetic nanoparticle relaxation measurement as a novel tool for in vivo diagnostics. In: *Journal of Magnetism and Magnetic Materials*, Jg. 252, H. 0, S. 387–389.
- [2] M. Myren, T. Mose, L. Mathiesen, L.E. Knudsen, The human placenta--an alternative for studying foetal exposure, *Toxicol In Vitro*, 21 (2007)1332-1340.
- [3] L. Seyfarth, U. Enke, R. Brauer, N. Brendel, M. Buttner, A. Csaki, F. Schlenk, C. Bergemann, D. Fischer, W. Fritzsche, P. Seidel, E. Schleussner, Placenta Perfusion - a Suitable Ex Vivo Model to Characterise Interaction of Nano-Particles with Human Tissue?, *Placenta*, 32 (2011) A29-A29.
- [4] M. Büttner, F. Schmidl, M. Schiffler, P. Seidel, Magnetorelaxation (MRX) Measurements With DC-SQUID Gradiometers, *IEEE Trans Appl Supercond*, 21 (2011) 473-476.
- [5] M. Büttner, P. Weber, F. Schmidl, P. Seidel, M. Roder, M. Schnabelrauch, K. Wagner, P. Gornert, G. Glockl, W. Weitschies, Investigation of magnetic active core sizes and hydrodynamic diameters of a magnetically fractionated ferrofluid, *Journal of Nanoparticle Research*, 13 (2011) 165-173.

# Conductive Zinc oxide thin films coated by combustion CVD using aerosol droplets at atmospheric pressure

I. Zunke<sup>1</sup>, A. Heft<sup>1</sup>, and P. Seidel

<sup>1</sup> *Innovent e.V. Technology Development, Prüssingstr. 27B, 07745 Jena*

ZnO is a good candidate for the replacement of commonly used indium tin oxide (ITO) thin films. Undoped as well as doped ZnO thin films with specific resistivities ranging from  $10^{-4} \Omega\text{cm}$  to  $10^7 \Omega\text{cm}$  have been produced by several CVD [1], sputtering [2], spray pyrolysis [3] or sol-gel [1] techniques. In cooperation with Innovent e.V., we have established an aerosol assisted combustion-CVD (C-CVD) process working under atmospheric pressure conditions that is suitable for using in an inline coating system for the glass industry. The established C-CVD process introduces only a short exposure of the substrates to the flame and therefore offers a better protection of its surface.

Innovent works on the three areas of competence; surface technologies, biomaterials and magnetic and optically systems. Especially the C-CVD-, r-C-CVD- and Plasma-CVD-technologies are employed and will be further developed.

The solid precursor  $\text{Zn}(\text{NO}_3)_2$  is dissolved in 2-propanol and deionised water (0,2 mol/l) and added to the gas flow by forming aerosol droplets. This zinc salt has significant advantages for the deposition of ZnO films compared with other commonly used organic substances like zinc acetylacetonate, zinc acetate or diethylzinc. It dissolves very well in water and 2-propanol; improved concentrations are therefore possible. It also does not clog the nozzle of the aerosol jet and is very easy in handling. A schematic view of the used system is shown in figure 1. The flame provides the energy for the reaction which

forms the reactive species and decomposes the precursor. The velocity of the table and the burner distance are the main parameter to influence the film thickness. The velocity affects the contact time between flame and substrate, whereas the distance influences the particle size.

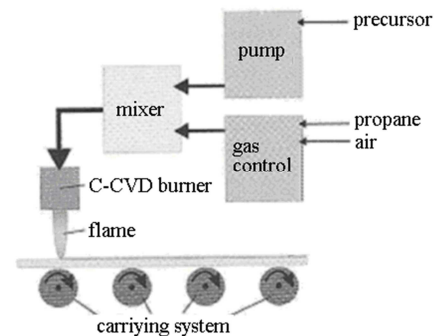


Fig. 1: Sketch of the used coating-system.

Typical film thicknesses of the deposited ZnO were in a range between 60 nm and 180 nm for several velocities. Small particles are formed during the combustion process, which agglomerate and adhere at the surface and thus form the thin film. When the thickness reaches a certain value, the particles begin to form an unbound porous powder.

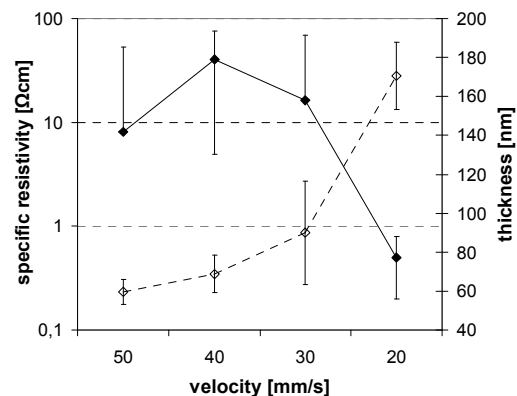


Fig. 2: Dependence of the sheet resistivity (continuous line) and film thickness (dashed line) on the velocity of the table at a burner distance of 7 mm.

The dependence of the specific resistivity on the film thickness is shown in figure 2. It can be seen, that the specific resistivity strongly depends on the film thickness and decreases with higher thicknesses. Usually the specific resistivity is independent of the film thickness, so this gives an advice to the morphology; thicker films are more compact than the thinner films. Lowest specific resistivities of about  $5 \cdot 10^{-1} \Omega\text{cm}$  are achieved at low substrate velocities and at high burner distances. When slowing down the velocity, the contact time between the flame and substrate increases. By that the number of particles reaching the substrate as well as the substrate temperature at the contact area rises.

For further investigation, all samples were characterised by XPS. The found elements and measured concentrations are marked in figure 3.

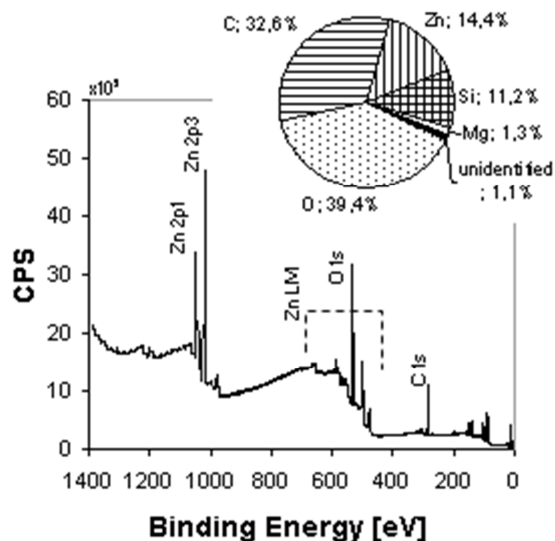


Fig. 3: Measured concentrations and XPS spectrum of a sample with 30 nm thickness with the basic peaks indicated.

So the ratio of Zn to O is not 1:1, whereat a certain share of the oxygen may be assigned to adhered water at the surface. Also the silicon substrate and adhered carbon can be identified as sources for the dislocation of the Zn to O ratio. In addition to that one can

state the fact that the detected electrons of oxygen have a higher energy than the ones of zinc. It is striking to state, that in spite of using  $\text{Zn}(\text{NO}_3)_2$  as precursor chemical, no nitrates were detected by XPS.

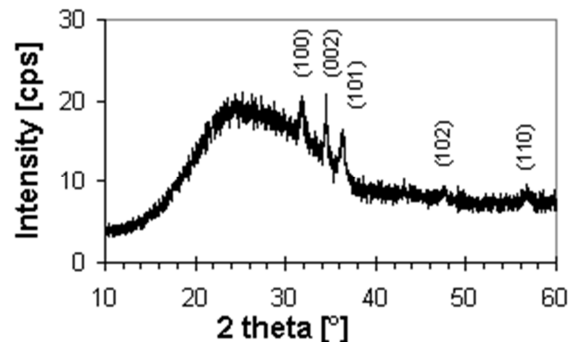


Fig. 4: XRD spectrum of a specimen at 7 mm working distance at 20 mm/s.

Using the XRD-analysis it could be proved that the coated ZnO films consist of crystalline ZnO (figure 4). It is hexagonal and is classified to the spacegroup P63mc. The lattice parameters were determined to  $a = 3.254 \text{ \AA}$  and  $c = 5.217 \text{ \AA}$ , which agree well with the literature.

The shown investigations confirmed the presence of ZnO. The undoped ZnO thin films are conductive and specific resistivities of around  $2,2 \cdot 10^{-1} - 10^2 \Omega\text{cm}$  are achieved. The presented technique is therefore a valuable addition to the more commonly used sputtering process. It furthermore has the advantage of its arrangement, where no additional reaction chamber or heating is needed.

Future investigations are pursuing focusing on the goal to dope these ZnO thin films with several elements, especially aluminium in order to produce the industry relevant highly conductive films.

## References

- [1] S. O'Brien et al., Thin Solid Films **518** (2010), p 4515–4519
- [2] C. Guillen et al., Vacuum **84** (2010), p 924–929
- [3] S. M. Rozati et al., Cryst. Res. Technol. **43**, (2008), p 273 – 275

## Mechanical loss of a sapphire single crystal at low temperatures

C. Schwarz, G. Hofmann, D. Heinert, J. Komma, P. Seidel, A. Tünnermann\*, R. Nawrodt

\* *Institut für Angewandte Physik, Friedrich-Schiller-Universität Jena, A.-Einstein-Str.15, 07745 Jena*

Low loss materials are of great interest for high precision measurements as ultra-stable cavities [1], whispering gallery modes resonators [2] and gravitational wave detectors [3]. Sapphire is such a material that provides low mechanical [4] and optical losses [5]. Previous measurements by Bagdasarov [4] revealed losses of  $2.5 \times 10^{-10}$  at 4.2 K. Using the example of a gravitational wave detector sapphire is used as a material for several optical components like mirrors, input couplers or beam splitters. As the laser beam passes through an optic or gets reflected from a surface the thermal noise of these components limits the sensitivity of the detector. The thermal noise is directly related with the mechanical loss of the material by the fluctuation-dissipation-theorem [6].

In this work the mechanical loss of a cylindrical sample with a diameter of 76.2 mm and a length of 24 mm was measured. The cylinder axis was parallel to the [1120] axis of the single crystal. All surfaces of the sample were polished to optical quality with a surface roughness of 0.96 nm (RMS). Compared to internal roughness measurements on silicon samples this value is up to five times higher which makes a loss contribution of a sample-suspension interaction due to rough and damaged surface layer possible.

The sample was suspended by means of a 75  $\mu\text{m}$  thick tungsten wire along the central plane of the barrel. To excite resonant vibrations an electrostatic comb like driving plate was placed within a distance of about 1 mm in parallel to one of the flat end faces. By tuning the frequency of the electric field close to one of the mechanical resonances

the sample started to vibrate. After reaching the maximum amplitude the frequency of the electric field was shifted to another value where no further energy coupled into the vibration and the free exponential ring down was read out with a commercial laser vibrometer [7]. From the time  $\tau$  for the amplitudes decay from the initial value to  $1/e$  and the resonant frequency  $f$  the mechanical loss can be calculated via:

$$\phi^{-1} = \pi f \tau . \quad (1)$$

Due to material parameters (e.g. the small piezoelectric constant) only three resonant modes between 32 and 51 kHz showed up with measurable amplitudes. To measure the mechanical loss in a temperature range from 5 to 325 K the probe chamber containing the suspended sample was placed inside a special built cryostat with optical view ports. The temperature sensing was carried out by a second sample of the same material and geometry to avoid additional friction on the loss measurement sample due to the contact between the sample and the temperature sensor.

Fig. 1 shows the results for the mechanical loss for three resonant frequencies. Without regard to the broad peak around 35 K the mechanical loss decreased with temperature down to  $1.8 \times 10^{-9}$  at 5.8 K which corresponds to a ring down time of about 4880 s. The first two modes showed similar losses due to their similar mode shapes.

For an explanation of the broad low temperature peak two approaches exist. In accordance to Braginsky [4] the peak is caused by Akhiezer damping which is based on phonon-phonon interaction. Bömmel and Dransfeld [8] formulated a

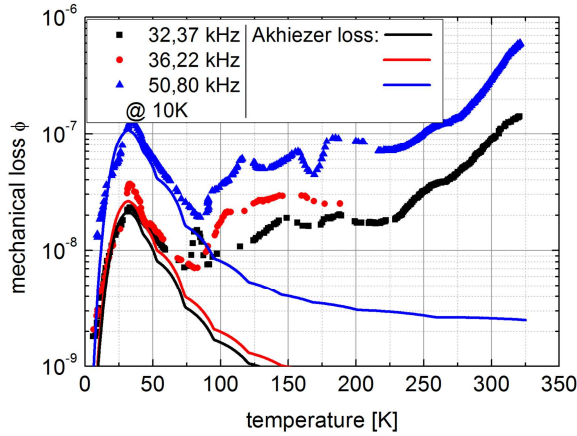


**Fig 1:** Temperature dependent mechanical loss of three resonant modes between 32 and 51 kHz in a temperature range of 5 to 325 K. The solid lines represent the calculated Akhiezer loss corresponding to the given resonant frequencies due to phonon-phonon interactions.

qualitative equation for further calculations:

$$\phi_{ph-ph} = \frac{CT\gamma^2}{\rho v^2} \frac{\omega\tau_*}{1 + (\omega\tau_*)^2}. \quad (2)$$

$C$  is the heat capacity,  $T$  the temperature,  $\gamma$  the Grüneisen parameter,  $\rho$  the material density,  $v$  the speed of sound,  $\omega$  the resonant frequency and  $\tau_*$  the mean phonon life time.  $\tau_*$  can be calculated from given values of the thermal conductivity  $\kappa$ :

$$\kappa \approx \frac{1}{3} \rho C v^2 \tau_*. \quad (3)$$

The results of equation (2) are plotted in fig. 1 as solid lines with the corresponding color to each resonant mode.  $\gamma$  was used as a parameter to scale the height of the Akhiezer loss for each mode. For the first mode at 32.37 kHz  $\gamma$  was chosen to be 2.0, for the others 2.1 and 3.8. Typical values for  $\gamma$  are between 1 and 3 [9]. 3.8 exceeds this range but perfectly fits the theory to the experimental data for the 50.80 kHz mode. The second approach [4, 10] for peaks below 100 K involves losses due to the mechanical treatment (e.g. spalling, grinding, lapping and finally polishing) of the sample. An annealing at high temperatures ( $\approx 1100^\circ\text{C}$ ) could reduce the losses to ex-

clude or at least minimize a loss contribution due to the mechanical treatment.

The presented data of the mechanical loss of sapphire at low temperature revealed a broad peak around 35 K and comparable low losses to silicon around 6 K. The origin of the peak can be explained by the presence of phonon-phonon interaction, called Akhiezer loss. Fig. 1 suggests that the lowest loss measured at 5.8 K is limited by a fundamental loss mechanism. Any further reduction on this sample can only be achieved by lowering the minimum temperature of the experimental setup.

An additional heat treatment, surface etching and cryogenic loss measurement are in the focus of our current investigations.

This work was supported by the DFG under contract SFB Transregio 7.

## References

- [1] S. Seel, et al.: Cryogenic Optical Resonators: A New Tool for Laser Frequency Stabilization at the 1 Hz Level. *Phys. Rev. Lett.* 78(25): 4741-4744, 1997.
- [2] V. S. Ilchenko et al.: Nonlinear Optics and Crystalline Whispering Gallery Mode Cavities. *Phys. Rev. Lett.* 92(4): 043903/1-4, 2004.
- [3] T. Tomaru et al.: Cryogenic measurement of the optical absorption coefficient in sapphire crystals at 1.064  $\mu\text{m}$  for the large-scale cryogenic gravitational wave telescope. *Phys. Lett. A* 283:81-84, 2001.
- [4] V. B. Braginsky, V. P. Mitrofanov, V. I. Panov: *Systems with Small Dissipation*. The University of Chicago Press, 1985.
- [5] D. Blair et al.: Optical absorption measurements in monocrystalline sapphire at 1  $\mu\text{m}$ . *Opt. Mat.* 8: 233-236, 1997.
- [6] H. B. Callen and T. A. Welton: Irreversibility and Generalized Noise. *Phys. Rev.* 83(1): 34-40, 1951.
- [7] <http://www.sios.de>, Dezember 2011
- [8] H. E. Bömmel and K. Dransfeld. Excitation and Attenuation of Hypersonic Waves in Quartz. *Phys. Rev.* 117(5):1245-1252, 1960.
- [9] S. Hunklinger: *Festkörperphysik*. Oldenbourg Wissenschaftsverlag GmbH, München, Wien, 2007.
- [10] C. R. Locke et al.: Properties of a monolithic sapphire parametric transducer: prospects of measuring the standard quantum limit. *Class. Quant. Grav.* 19:1877-1888, 2002.



## Oxygen induced mechanical loss in crystalline silicon

G. Hofmann, J. Komma, C. Schwarz, D. Heinert, G. Hammond\*, K. Haughian\*,  
P. Murray\*, S. Rowan\*, P. Seidel, and R. Nawrodt

\* *Institute for Gravitational Research, SUPA University of Glasgow, G12 8QQ Glasgow, UK*

Mechanical loss is directly linked to thermal noise via the Fluctuation-Dissipation-Theorem [1]. Thus, the understanding of mechanical loss mechanisms in solids plays a crucial role in view of the improvement of the sensitivity of high-precision experiments such as opto-mechanics, laser stabilisation or gravitational wave detectors.

Silicon has several advantages over other materials like sapphire or calcium fluoride as an optical material in such experiments. It is produced in large quantities with considerable purity and presumably soon available with diameters up to 500 mm. In addition it shows suitable optical properties at the quite common wavelength of 1550 nm [2].

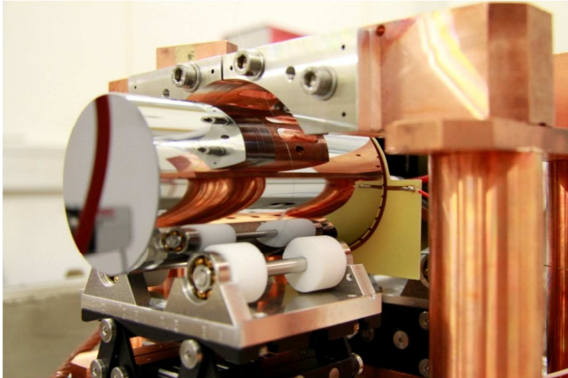


**Fig. 1** Suspension of the silicon sample inside the cryostat by a single loop of a tungsten wire.

We investigated cylindrically shaped single crystal silicon samples. All surfaces of the substrates have been polished to optical quality. The samples are suspended by a single loop of tungsten wire inside a special built cryostat (Fig. 1) capable to operate at temperatures between 5 and 300 K [3]. Using an electro-static driving plate the samples are excited to resonant vibrations and the displacement is detected with a commercial interferometer.

The free decay of the resonant movement with frequency  $f_{\text{res}}$  provides the ring-down-time  $\tau_{\text{ring}}$  and gives the  $Q$ -factor

$$Q = \pi f_{\text{res}} \tau_{\text{ring}}. \quad (1)$$

An alternative definition of the  $Q$ -factor is given by the relative energy loss per cycle

$$Q = \frac{2\pi \cdot \Delta E}{E} = \phi^{-1}, \quad (2)$$

which is for high  $Q$ -factors as obtained the inverse of the mechanical loss  $\phi$ .

Mechanical loss in solids is caused by different mechanisms of energy dissipation. Irreversible heat flow for example occurs between the stretched and compressed areas during the oscillation of the substrate. Thereby, the resonant vibration gets damped by the so called thermo-elastic loss [4]. The thermo-elastic damping of a bulk sample was calculated using a finite element analysis software like COMSOL due to its complicated mode shape.

Another origin of mechanical loss is due to defects in the crystalline lattice. The model of the standard anelastic solid gives rise to a frequency dependence of the mechanical loss

$$\phi(\omega) = \Delta \frac{\omega\tau}{1 + \omega^2\tau^2}, \quad (3)$$

with the frequency  $\omega = 2\pi f$  and a characteristic relaxation time  $\tau$ . The loss shows a Debye peak with a maximum at  $\omega\tau = 1$ . The relaxation time  $\tau$  is temperature dependent and follows the Arrhenius law

$$\tau = \tau_0 \exp\left(\frac{E_a}{k_B T}\right), \quad (4)$$

where  $\tau_0$  represents a characteristic relaxation constant,  $E_a$  stands for the activation energy whereas the product of Boltzmann's constant  $k_B$  and temperature  $T$  form the corresponding thermal energy [6]. Crystal defects like vacancies, impurities and interstitials normally are in thermal equilibrium

states. These may be described as a double well potential with equal transition rates between the states. If the equilibrium gets disturbed, one state is overpopulated. The relaxation to the new equilibrium requires energy to “jump” over the barrier  $E_a$  and also a relaxation time  $\tau$ .

Our measurements of 3 different silicon substrates provide a similar behavior in mechanical loss for each of them [7]. In Fig. 2 the dependency of the mechanical loss on temperature is exemplarily shown for a sample of 65 mm in diameter and 50 mm in height.

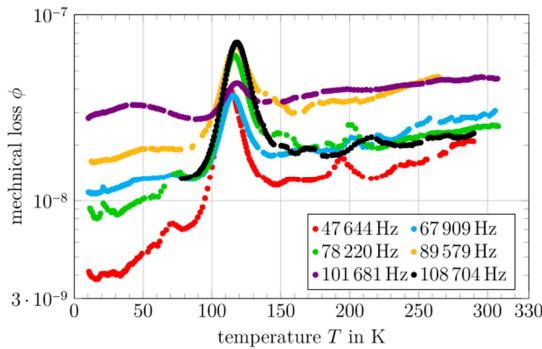


**Fig. 2** Mechanical loss  $\phi$  over temperature  $T$ . With decreasing temperature the mechanical loss also decreases. Below 40 K a loss of about  $4 \times 10^{-9}$  is reached. Around 120 K a Debye peak occurs. It is due to the presence of interstitial oxygen.

With decreasing temperature the mechanical loss decreases up to nearly one order of magnitude. The lowest loss is achieved below temperatures of 40 K and reaches  $4 \times 10^{-9}$ . In the region around 120 K a peak of Debye shape is observable. This Debye peak is associated with the presence of oxygen in the three 65 mm diameter Czochralski grown single crystal samples. In contrast, float-zone grown samples with 100 times less oxygen concentration do not show this peak. The interstitial oxygen settles along the  $\langle 111 \rangle$  direction bond between two silicon atoms. Because of the symmetry of the crystal there exist six equivalent positions for the oxygen. During the resonant movement of the silicon sample the atomic lattice gets slightly deformed. This causes the oxygen to change between these positions linked with dissipation of energy.

Increasing resonance frequency  $f_{\text{res}}$  the maximum is shifted to higher temperatures  $T_{\text{max}}$ . Thus the activation energy  $E_a$  can be determined using eq. (5) by plotting  $\ln(2\pi f_{\text{res}})$  over  $1/T_{\text{max}}$  as shown in Fig. 3. We obtained an activation energy about 168 meV for the loss mechanism which is consistent with results of other groups.

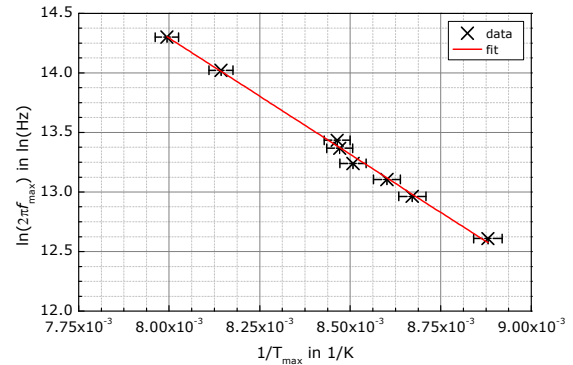


**Fig. 3** Arrhenius plot for the observed Debye peak. The activation energy yields 168 meV.

This work was supported by the German science foundation within the SFB TR7.

## References

- [1] P. R. Saulson. Phys. Rev. D, 42(8):2437–2445, 1990.
- [2] S. Rowan, J. Hough, D. R. M. Crooks. Phys. Lett. A, 347(1–3):25–32, 2005.
- [3] R. Nawrodt, A. Zimmer, S. Nietzsche, M. Thürk, W. Vodel und P. Seidel. Cryogenics, 46(10):718–723, 2006.
- [4] V. B. Braginsky, Mitrofanov V. P. und V. I. Panov. *Systems with Small Dissipation*. The University of Chicago Press, 1985.
- [5] C. Zener. Phys. Rev. 52:230–235, 1937.
- [6] A. S. Nowick und B. S. Berry. *Anelastic Relaxation in Crystal Solids*. Academic Press, 1972.
- [7] G. Hofmann. *Charakterisierung von Bulk-Materialien bei tiefen Temperaturen*. Diplomarbeit, Friedrich-Schiller-Universität Jena. 2011.

# Parametric instabilities in future gravitational wave detectors

D. Heinert, R. Nawrodt, S. Strigin<sup>1</sup>

<sup>1</sup>*Physics Department, Moscow State University, Moscow 119991, Russia*

Future gravitational wave detectors have to provide high sensitivities to detect the tiny effects of gravitational waves. One of the key limitations is thermal noise. In order to lower the thermal noise a reduction of the mechanical loss of the interferometer's mirrors is necessary.

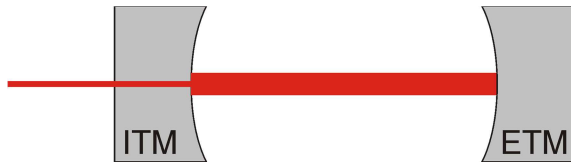


**Fig. 1:** Arm cavity of gravitational wave detectors. The laser light enters the cavity through the input test mass (ITM). Together with the end test mass (ETM) a resonant system is formed. The line width illustrates the intensity increase in the cavity.

But the decrease of mechanical loss within the detector allows a nearly undamped motion of the substrates once they are excited. One possible source of excitation is called parametric resonance. In this case an initial motion at the substrate resonances leads to a phase modulation of the laser beam within the arm cavity of the interferometric detector (Fig. 1). This modulation produces beats in the laser intensity and therefore a periodic change of the radiation pressure force on the substrate. The reflected field with a decreased frequency is called Stokes field. If it shows resonance with one of the optical cavity modes - the Stokes mode - the mirror's motion is amplified and drives the detector out of its working point. A detection of gravitational waves then becomes impossible. The whole effect is called parametric instability (PI).

The effect of PI was first investigated by Braginsky, Strigin and Vyatchanin in 2001 [1]. As an instability criterion they found

$$\frac{W}{cmL} \frac{\omega_1}{\omega_m \gamma_m \gamma_1} \frac{\Lambda}{1 + \frac{\Delta^2}{\gamma_1}} > 1. \quad (1)$$

Here  $W$  is the power of the reflected laser light,  $c$  the speed of light,  $m$  the mirror mass, and  $L$  the length of the arm cavity.  $\omega_1$  represents the optical frequency of the Stokes mode and  $\omega_m$  the mechanical frequency of the mirror's oscillation.  $\gamma_1$  and  $\gamma_m$  indicate the relaxation rates of the Stokes mode and the mirror, respectively. The radial frequency deviation between the modulated light and an optical resonance of the cavity is given by  $\Delta$ . The effect of PI also demands, that both optical modes and the mechanical mode show a similar spatial dependence. This fact is considered in the overlap factor

$$\Lambda = \frac{V[\int E_0(r)E_1(r)u_z(r)dA]^2}{\int |E_0|^2 dA \int |E_1|^2 dA \int |\vec{u}|^2 dV}. \quad (2)$$

$E_0$  and  $E_1$  describe the electric field of the optical main and Stokes mode, respectively, at the reflecting surface  $A$ . The motion of the mirror is summarised in the displacement  $\vec{u}$ .

D'Ambrosio and Kells [2] later showed that the mirror motion could also be damped by the effect of PI. This happens if the Anti-Stokes field is resonant in the cavity. Nevertheless this effect does not exclude all possible PIs as the resonance spectrum of the cavity is not symmetric around its main mode. A first consideration of initial LIGO could therefore not exclude the appearance of PIs [3]. Further model calculations of Advanced LIGO confirmed this work and showed several parametrically instable combinations [4].

As the successful detection of gravitational waves demands high laser powers to reduce

photon shot noise, it will lead to the effect of PI. Future detectors should therefore show techniques to damp PIs. One method suggests the attachment of lossy coatings to the barrel surface of the mirror. This should effectively damp the mirrors motion, lead to an increased value of  $\gamma_m$  and reduce the gain for PIs. Noise calculations also guarantee that the effect on the detector sensitivity should be tolerable [5]. A second approach uses an active scheme to damp the mirror motion by means of electrostatic actuators. The effectiveness of this approach was demonstrated experimentally in [6]. Nevertheless this method requires one feedback loop for each PI to be damped. Therefore, the reduction of the number of PIs by other means is favourable.

A displacement  $Z$  between the optical mode and the mirror substrate can cause an increased number of PIs and represents the main issue of this report. Without a displacement  $Z = 0$  the numerator of Eq. (2) permits only combinations with the same azimuthal behaviour to undergo PI. This condition fails if a misorientation  $Z \neq 0$  is allowed. Then the number of PI should increase. A quantitative analysis of this effect is given in [7]. As a starting point we calculated possible unstable combinations using the parameters of Advanced LIGO. For that purpose the mechanical resonances of the mirrors have been calculated with the help of the FEA software ANSYS [8]. The accuracy of the numerical calculation was proven by means of Chree-Lamb and torsional modes. Without a displacement ( $Z = 0$ ) we found a total of 12 unstable modes for frequencies below 50 kHz. Four of them were later ruled out by the effect of anti-Stokes modes. Then a displacement of  $Z = 1$  cm was considered. This calculation revealed two additional unstable combinations. At the same time the parametric gain of former

combinations decreased by up to 20%. For all calculations our numerical analysis maximised the parametric gain with respect to an optimal choice of a rotation between the optical and mechanical modes. The effect of such a rotation is illustrated in Fig. 2 for the newly arising combinations.

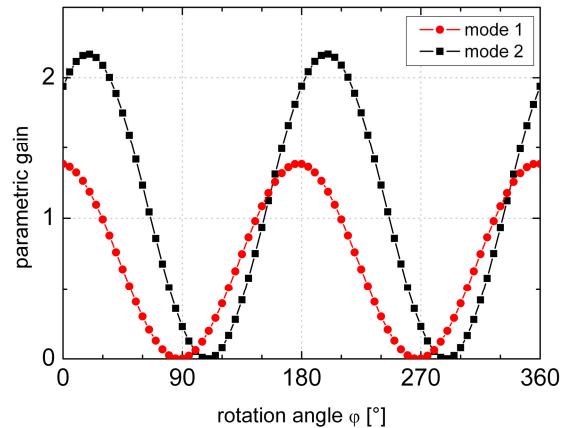


Fig. 2: Parametric gain variations due to a rotation between the optical and the mechanical modes. The sinusoidal behaviour must be taken into account for a reliable estimate of the effect of PI.

Due to noise couplings of the alignment control the displacement in future detectors should be well below  $Z = 1$  mm. At this scale changes in the parametric gain are well below 1% and, thus, negligible.

This work was supported by the DFG under contract SFB Transregio 7.

## References

- [1] V. B. Braginsky, S. E. Strigin, S. P. Vyatchanin, Phys. Lett. A 287, 331 (2001)
- [2] E. D'Ambrosio, W. Kells, Phys. Lett. A 299, 326 (2002)
- [3] V. B. Braginsky, S. E. Strigin, S. P. Vyatchanin, Phys. Lett. A 305, 111 (2002)
- [4] C. Zhao, L. Ju, J. Degallaix, S. Gras, D. G. Blair, Phys. Rev. Lett. 94, 121102 (2005)
- [5] S. Gras, D. Blair, L. Ju, Phys. Lett. A 372, 1348 (2008)
- [6] J. Miller, M. Evans, L. Barsotti, P. Fritschel, M. MacInnis, R. Mittleman, B. Shapiro, J. Soho, C. Torrie, Phys. Lett. A 375, 788 (2011)
- [7] D. Heinert, S. E. Strigin, Phys. Lett. A 375, 3804 (2011)
- [8] www.ansys.com

# Investigation of the mechanical loss of a thin crystalline quartz flexure

J. Komma, G. Hofmann, C. Schwarz, D. Heinert,  
G. Hammond\*, I. W. Martin\*, P. Seidel and R. Nawrodt

\*Institute for Gravitational Research, SUPA University of Glasgow, G12 8QQ Glasgow, Scotland

The mechanical properties and the behaviour of defects in crystalline quartz are well known and understood [1-3]. Therefore, this material is of great interest in commissioning and characterising a new setup for the study of the mechanical losses.

In this work the mechanical loss of a thin flexure of crystalline quartz was measured. This is the first loss measurement for such a thin structure in the audio frequency range for crystalline quartz in a temperature range from 5 to 300 K. The advantage of our sample compared with earlier investigations of bulk material is the simple geometry: There is no special sample preparation needed in order to get a low loss sample.

In this study a thin beam with a length of 43 mm, a width of 8.4 mm, and a thickness of 100  $\mu\text{m}$  was clamped at one end. The measurements have been performed by means of a ring-down technique. The sample is excited to resonant vibrations and the subsequent free ring-down is recorded by means of a highly sensitive vibration sensing method [4].

The mechanical loss  $\phi$  can be calculated via

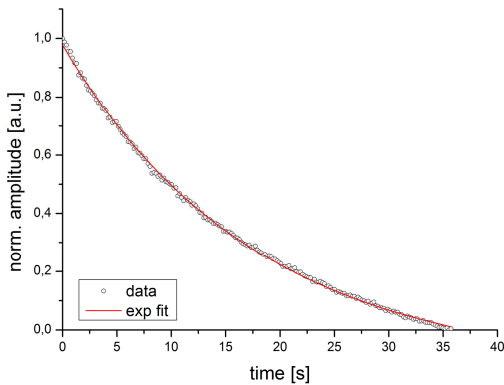


Fig. 1: Typical ring-down at a frequency of 1.8 kHz at 37 K. An exponential fit allows to calculate the ring-down time.

[5]:

$$\phi^{-1} = \pi f \tau \quad (1)$$

with the resonance frequency  $f$  and the characteristic ring-down time  $\tau$ . The ring-down time is determined as shown in Fig. 1 as the time to reach 1/e of the initial amplitude.

Fig. 2 shows a typical curve for a mechanical loss measurement for one resonant frequency. Above 50 K the loss is dominated by thermo-elastic damping [6]. Around

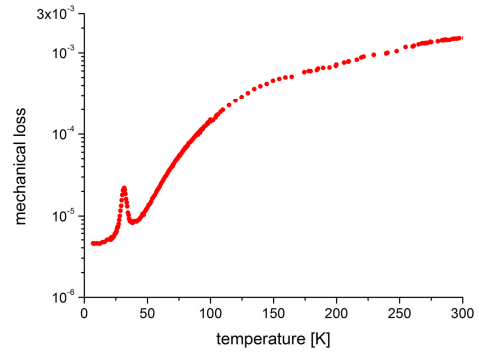
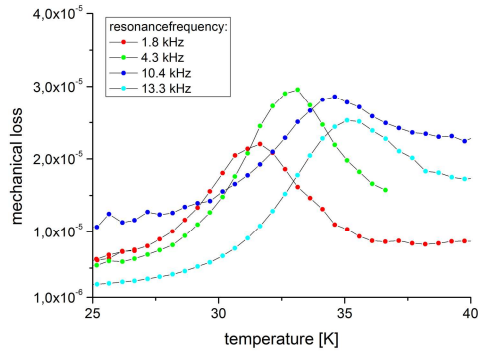


Fig. 2: Measured mechanical loss for a resonance frequency of 1.8 kHz.

35 K there is a significant loss peak. Earlier investigations identified sodium impurities as the origin of this defect peak.

In total, 16 different resonances have been studied. Fig. 3 shows the defect peak for different resonance frequencies. A shift for the maximum of the mechanical loss in temperature depending on the frequency is observed. This is a typical behavior for a thermally activated relaxation process. These processes are described by a Debye-like structure:

$$\phi = \Delta \times \frac{\omega \tau}{1 + \omega^2 \tau^2} \quad (2)$$



**Fig. 3:** Temperature shift of the loss peak shown for some resonance frequencies.

$\Delta$  is the relaxation strength,  $\omega$  the angular frequency of the vibration and  $\tau$  the relaxation time of the process. The relaxation time is given by [6]:

$$\tau = \tau_0 \exp\left(\frac{E_A}{k_B T}\right), \quad (3)$$

with the relaxation constant  $\tau_0$  and the activation energy  $E_A$  which is specific for a special loss process. With the knowledge that the maximum of the loss peak is located at  $\omega\tau = 1$ ,  $E_A$  can be obtained from an Arrhenius plot which is shown in Fig. 4. In

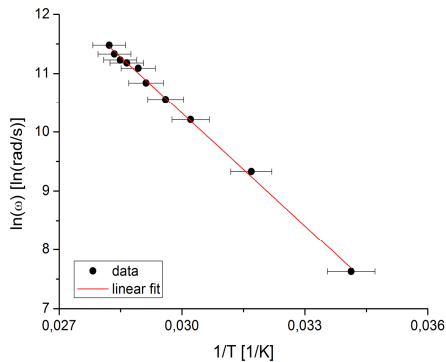


**Fig. 4:** Arrhenius plot of the mechanical loss peak at around 35 K [4].

this work the activation energy was determined to be  $(55 \pm 1)$  meV. This is in good agreement with previous bulk measurements of our group, where an activation energy of 56 meV was found [7, 8]. The activation energy corresponds to a transition of

the defect between two quasi-stable positions along the z-axis of the crystal (see Fig. 5).

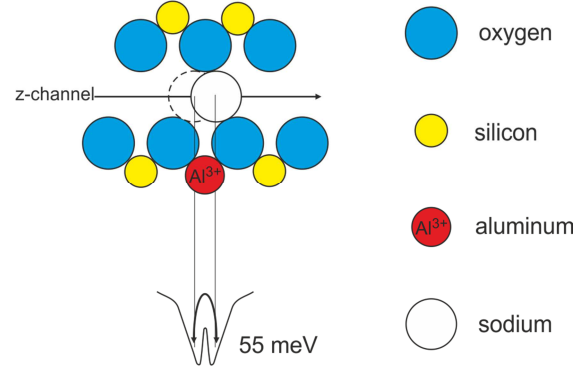


**Fig. 5:** Movement of a sodium defect inside crystal-line quartz.

It was shown that the defect analysis by means of mechanical spectroscopy of crystalline quartz is possible in thin flexures having a simplified geometry compared to samples that have been used previously.

This work was supported by the DFG under contract SFB Transregio 7.

## References

- [1] J. J. Martin. Aluminum-Related Acoustic Loss in AT-Cut Quartz Crystals (1984)
- [2] W. P. Mason. Impurities and Anelasticity in Crystalline Quartz, in: Physical Acoustics, Vol. III, Bd. 25. New York: Academic Press (1965)
- [3] A. S. Nowick und B. S. Berry. Anelastic Relaxation in Crystalline Solids. Academic Press (1972)
- [4] G. Hofmann. Principles and methods for Q factor measurements of cantilevers, Studienarbeit Friedrich-Schiller-Universität Jena (2010)
- [5] R. Saulson. Fundamentals of gravitational wave detectors, World Scientific, Singapore (1994)
- [6] C. Zener. Internal Friction in Solids. I. Theory of Internal Friction in Reeds, Phys. Rev. 52 230-235 (1937)
- [6] V. B. Braginsky, V. P. Mitrofanov, V. I. Panov. Systems with Small Dissipation. The University of Chicago Press (1985)
- [7] R. Nawrodt. Kryogene Gütemessung an optischen Substratmaterialien für zukünftige Gravitationswellendetektoren. Dissertation, Friedrich-Schiller-Universität Jena (2008)
- [8] A. Schröter. Mechanical losses in materials for future cryogenic gravitational wave detectors. Dissertation, Friedrich-Schiller-Universität Jena (2007)

# Rare-Earth Compound Regenerator for a Coaxial Two Stage Pulse Tube Refrigerator

R. Habibi, M. Thürk, and P. Seidel

Pulse tube refrigerators (PTRs) have the potential to operate nearly vibration free since they work without a moving piston. Therefore they are on the center point of the actual cryocooler research.

The established PTR-design featured a spatial separation between regenerator and pulse tube, which is called a U-tube PTR.

To miniaturize this refrigerator and to avoid remaining perpendicular vibrations a coaxial design had been developed by Köttig [1]. Two needle valves per stage provide the active phase shift. With a two stage coaxial construction (Fig. 1) no-load cold tip temperatures down to 5.2 K were reached.

The first stage regenerator of this PRK was made out of stainless steel wire mesh screens. For second stage lead coated wire mesh screens were used because lead provides the topmost volumetric heat capacity below 40 K (Fig. 2).

The theory of Debye predicts a cubic correlation between the temperature and the heat capacity at low temperatures whereas the specific heat of helium near the phase boundary increases below 10 K. According to the regenerator theory this proportion of the heat capacities decreases heat regeneration manifestly, which is unbearable for a 4.2 K PTR [3].

Our measurements of the axial temperature profile of the second stage (Fig. 3) have verified a very inefficient heat-regeneration at temperatures below 10 K. The axial temperature gradient is very low near the cold tip in contrast to the gradient near the warm end of the second stage (Fig. 3).

Special materials perform a second order magnetic phase transition even below 10 K that results in an additional contribution to the heat capacity (Fig. 4).

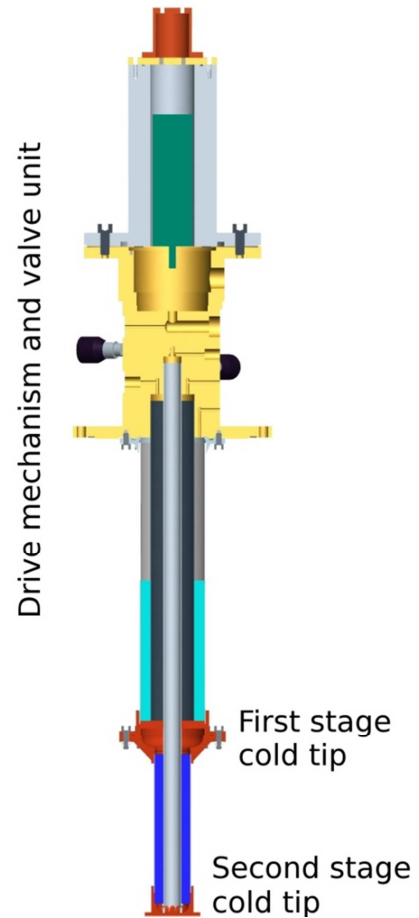


Fig. 1: Sectional view of the two stage PTR in coaxial design. The 2<sup>nd</sup> stage pulse tube is located inside the respective regenerator and additionally inside 1<sup>st</sup> stage pulse tube.

From our assessments ErNiCo and ErNi have emerged as appropriate materials in a combination with Gd<sub>2</sub>O<sub>2</sub>S (GOS) for high cooling power at 4.2 K.

Based on an investigation about the second stage's temperature profile (Fig. 3) and the specific heat of the new materials (Fig. 4) we designed a new multilayer second stage regenerator.

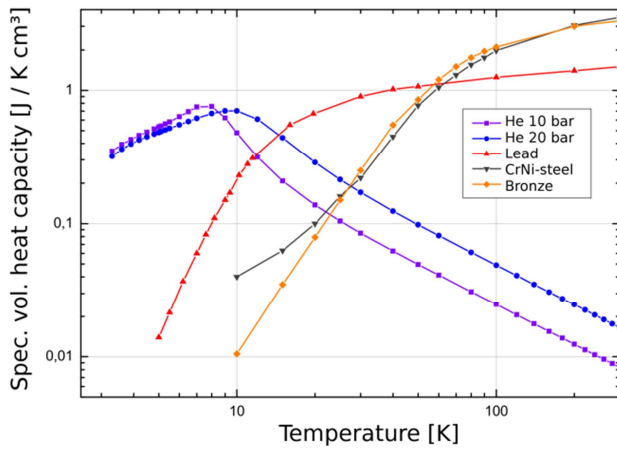


Fig. 2: Diagram of the specific volumetric heat capacity of lead and helium [2]. In contrast to helium the specific heat of lead decreases from 300 K to 4 K by two orders of magnitudes.

(Fig. 5) ErNiCo is used for regeneration at the cooler's lowest temperatures and is placed near the cold tip.

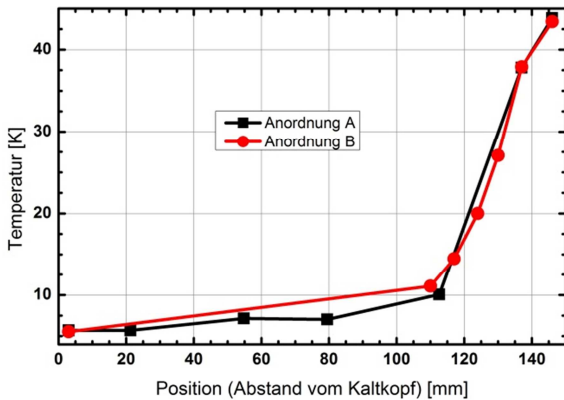


Fig. 3: Temperature distribution at the 2<sup>nd</sup> before the reconstruction. The dots in profile A and profile B are indicating the different spatial distribution of the measurement points. The temperature gradient at the coldest 75 % of this regenerator is very low because the regeneration is very ineffective.

At the warm end of this stage the successfully used lead wire mesh screens are installed because of their high specific heat in the temperature range above 14 K. Between these two materials ErNi is located.

With this setup we have reached temperatures below 4 K first time ever for a coaxial design. Furthermore we will optimize working parameters to increase the cooling power at 4.2 K.

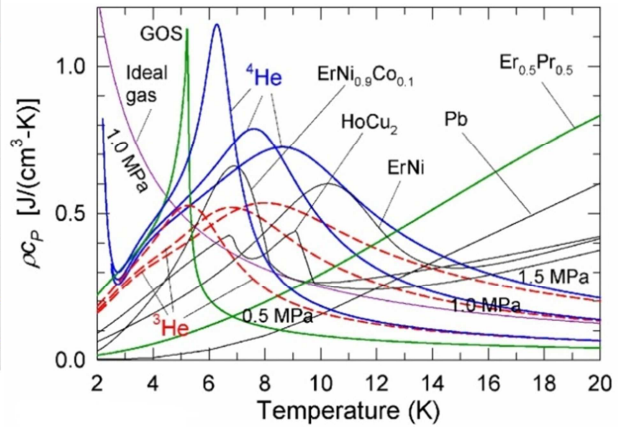


Fig. 4: Diagram of the specific volumetric heat capacity of different rare-earth compounds [4]. The comparison to ordinary materials like lead shows the high proportion of heat capacity resulting from the magnetic system.

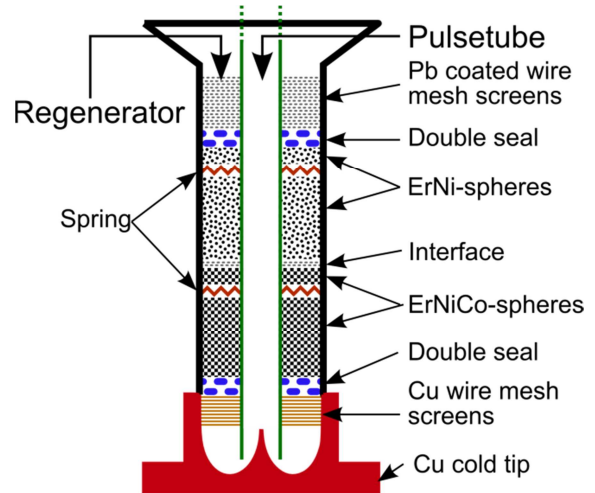


Fig. 5: Sectional schematic view of the new 2<sup>nd</sup> stage.

## References

- [1] Köttig, T., "Dünnschichtsysteme für die effektive Tieftemperaturregeneration," Ph.D. thesis, Friedrich-Schiller-Universität, Jena, DE (2007).
- [2] Köttig, T., "Untersuchungen zum Aufbau leistungsstarker coaxialer Pulsationsröhrenkühler," Diploma thesis, Friedrich-Schiller-Universität, Jena DE (2004), p. 23.
- [3] Ackermann, R.A., *Cryogenic Regenerative Heat Exchangers*, Plenum Press, NY (1997), pp. 90–101.
- [4] Radebough, R., Huang, Y., O'Gallagher, A., and Gary, J., "Calculated Performance of Low-Porosity Regenerators at 4 K with He-4 and He-3," *Cryocoolers 15*, ICC Press, Boulder CO (2009), p. 332



# Josephson junctions with different transparency distribution functions

S. Schmidt, V. Shaternik<sup>1,2</sup>, A. Shapovalov<sup>1,2</sup>, S. Larkin<sup>2</sup>, S. Döring, F. Schmidl, V. Tympel and P. Seidel

<sup>1</sup> G.V. Kurdyumov Institute for Metal Physics, National Academy of Science of Ukraine, 252680 Kyiv, Ukraine  
<sup>2</sup> Concern "Nauka", Dovnar-Zapolskii street 2/20, 03116 Kyiv, Ukraine

Josephson junctions are an effective tool to investigate all kinds of superconductors and their fundamental properties.

Consisting of two superconductors being separated by a barrier layer, it is important to understand exactly what happens in this barrier. Theoretical works of Shaternik et al. [1] calculated I-V characteristics of Josephson junctions with different barrier properties, i.e. different transparency parameters  $D$  (Fig. 1). Based on these calculations, we plan to investigate the properties of the barriers we use in our junction preparation in order to examine superconducting properties of iron based superconductors. [2,3] Thus, we started a collaboration between the superconductivity group of the IFK Jena and the Ukrainian Institute for Metal Physics, Kiev.

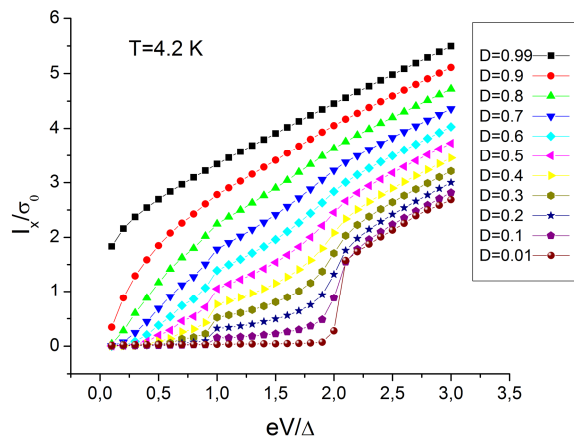


Fig. 1: I-V characteristics for different values of the barrier transparency  $D$ . Subharmonic gap structures are visible at voltage values  $2\Delta/2$  and  $2\Delta/3$ .

In November/December 2011 the first exchange of scientists from Kiev to Jena resulted in jointly produced cross-junctions of  $\text{YBa}_2\text{Cu}_3\text{O}_{7-\delta}$  (YBCO) and Pb as superconductors separated by an Au barrier. With different junction areas between

$50 \times 100 \mu\text{m}^2$  and  $200 \times 225 \mu\text{m}^2$  (see Fig. 2) the influence of the area on the junction transparency can be examined.

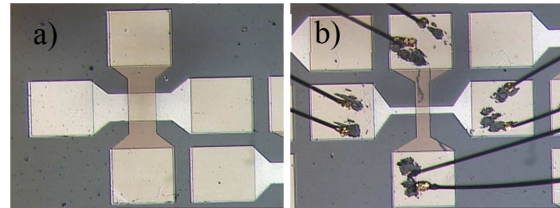


Fig. 2: a) Microscopic image of a cross-junction of YBCO (vertical) and Pb covered by In (horizontal) with a junction area of  $200 \times 200 \mu\text{m}^2$  and a gold barrier layer with a thickness of 10 nm. b) Similar junction with an area of  $50 \times 100 \mu\text{m}^2$ . Ultrasonic bonded gold wires are visible.

During the collaboration we will investigate the influence of both the thickness and the junction area on the transparency for different barrier materials (Au,  $\text{SiO}_2$ ,  $\text{TiO}_x$  in Jena,  $\text{AlO}_x$  in Kiev). Electrode materials can be YBCO, Pb (Jena) and MoRe (Kiev). Additionally, the novel superconductors  $\text{BaFe}_{1.8}\text{Co}_{0.2}\text{As}_2$  (Jena) and  $\text{MgB}_2$  (Kiev) can be used.

The junctions will be jointly produced and analysed in both institutes including the exchange of scientists.

This work was partially supported by German BMBF within project UKR 10/034, Ukrainian MES within project 426 and Landesgraduiertenförderung Thüringen.

## References

- [1] V. Shaternik, S. Larkin, V. Noskov, V. Chubatyy, V. Sizontov, A. Miroshnikov, A. Karmazin Journal of Physics: Conference Series (JPCS), 97: 012243 (2008).
- [2] S. Schmidt, S. Döring, F. Schmidl, V. Grosse, P. Seidel, K. Iida, F. Kurth, S. Haindl, I. Mönch, B. Holzapfel, Appl. Phys. Lett. 97 (2010) 172504
- [3] S. Döring, S. Schmidt, F. Schmidl, V. Tympel, S. Haindl, F. Kurth, K. Iida, I. Mönch, B. Holzapfel, P. Seidel, arXiv :1108.0851v2

# New closed cycle refrigerator system for electro-optical measurements

M. Gnauck, S. Schönherr, K. Puschkarsky

A new He-based refrigerator system consisting of a closed cycle cryostat (Janis Research CCS-450), a temperature controller (Lakeshore 336) and a water-cooled helium compressor (Cryogenics 8200) has been set up at the IFK in order to expand the temperature range for electro-optical measurements. The new system uses the Gifford-McMahon thermodynamic cycle to remove heat continuously from a solid sample mounted on a cold head and redundantizes any need for liquid nitrogen or helium. The lowest temperature achievable is about 10 K, when using a prefabricated additional radiation shield. The powerful temperature controller not only stabilizes the temperature on a mK scale but also allows setting defined temperature ramps and overcomes the former system's temperature limits of 30 and 300 K to 10 and 500 K, respectively. The cold head can be evacuated in order to avoid contamination from condensation and to minimize radiative heat input from outside (see Fig. 1). The working pressure is typically below  $1 \cdot 10^{-6}$  mbar.

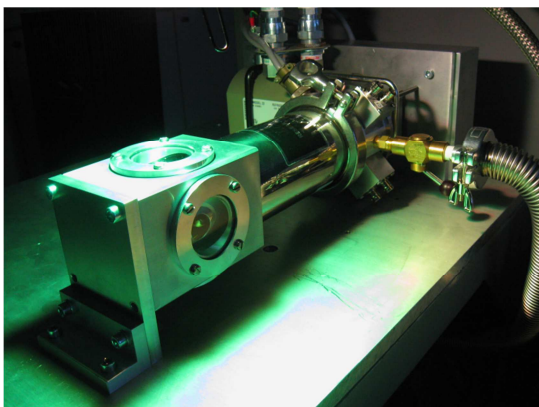


**Fig. 1:** The cryostat is by default horizontally mounted on a vibration-cushioned table and can also easily be used in a vertical setup. Here, the new cryostat is used to perform temperature dependent current voltage measurements on a  $\text{Cu(In,Ga)(Se,S)}_2$  solar cell under varied illumination conditions.

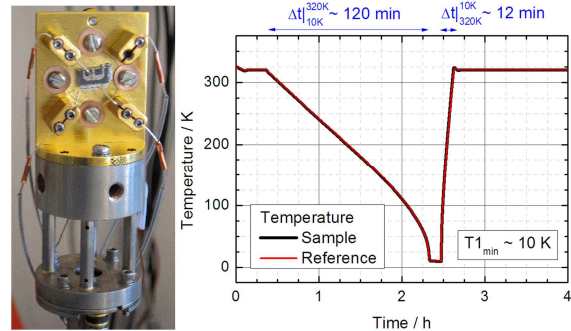


**Fig. 2:** Left: Gold-plated copper cold head assembled with a  $\text{Cu(In,Ga)(Se,S)}_2$  solar cell, which is electrically connected to the measurement equipment by two contact fingers. Right: Temperature profile of the unloaded cold head measured at its rear side (“Sample”) and a reference point some cm in distance below (“Reference”).

Versatile electro-optical measurements at different temperatures are possible now as the new cryostat is equipped with four quartz windows of 4.1 cm diameter. The electrical connection to the external measurement equipment is established by up to four contact fingers, which can be placed on the sample individually (see Fig. 2). For samples larger than  $1 \text{ cm}^2$  (max.  $10 \text{ cm}^2$ ) in lateral size only two-point measurements are operable at the moment.

With a refrigeration capacity of about half a Watt at 20 K (without any heat load) the base temperature can be reached in roughly 2 hours; whereas, the heating power is sufficient to apply 25 K/min throughout a large temperature range. By choosing one of three different output power settings virtually any intermediate cooling or heating rate can be user-defined. Additionally, a software program written in LabVIEW allows flexibly monitoring, storing and controlling the system's temperatures as well as configuring diverse settings.

## Luminescence of Ga-graded Cu(In,Ga)Se<sub>2</sub> thin-films

J. Haarstrich, M.Gnauck, H. Metzner, C. Ronning, A. Undisz\*, T. Rissom\*\*, C.A. Kaufmann\*\*, and H.W. Schock\*\*

\* Institut für Materialwissenschaft, Löbdergraben 32, 07743 Jena

\*\* Helmholtz-Zentrum Berlin für Materialien und Energie, Hahn-Meitner-Platz 1, 14109 Berlin

In today's high efficiency solar cells based on Cu(In,Ga)Se<sub>2</sub> (CIGSe) absorber layers, the ratio [Ga]/([Ga]+[In]) (GGI) varies with depth. Hence, a grading in composition and band-gap is commonly present in the layer. The band-gap variation through the addition of gallium is discussed to be beneficial for solar cell performance if it is adjusted properly [1,2]. Thus, an efficient control of the grading by suitable characterization techniques is needed.

Standard CIGSe thin-films with a thickness of about 2  $\mu\text{m}$  were prepared by multi-stage co-evaporation onto Mo-coated soda-lime glass [3]. Solar cells made from these absorbers using the standard ZnO/CdS window structure [3] show efficiencies up to 17%. The Ga-grading was measured by means of energy dispersive X-ray spectroscopy (EDS) in a transmission electron microscope (TEM). The TEM specimen was prepared by lamella preparation with a focused ion beam (FIB) system. The absolute Ga-concentration of the profile was scaled through normalization to the XRF measured integral stoichiometry of  $\text{GGI}=0.296(2)$ .

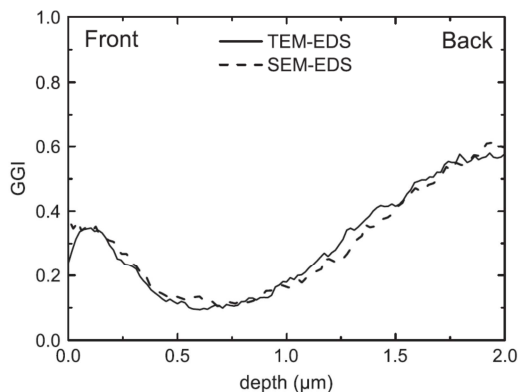


Fig. 1: The ratio GGI of a CIGSe thin-film as a function of depth as it was determined using TEM-EDS (lamella) and SEM-EDS (in cross section), respectively.

The CL measurements were performed with an acceleration voltage of 10 kV at 10 K. The spectra were obtained while scanning an area of about 400  $\mu\text{m}^2$  and, hence, represent the luminescence averaged over a large number of grains.

The determined GGI is shown as a function of depth in Fig. 1 as it was measured on a cross-section sample. The profile is in very good agreement compared to data obtained on samples with secondary ion mass spectroscopy [4], and they illustrate the Ga-grading, which is present in the CIGSe absorber layers. The grading has been identified to be due to real alloying of CuInSe<sub>2</sub> and CuGaSe<sub>2</sub> by X-ray diffraction at the very same samples [5].

Cross-section samples of complete solar cells were investigated by imaging in both secondary electron and monochromatic CL imaging mode at various detection energies ranging from 0.8 to 1.4 eV. Selected images are shown in Fig 3. and display that the 1.30 eV emission is mainly localized at the interface to the back contact. Observation of luminescence at this wavelength is possible only if the generation takes place in the back contact region. At a detection energy of 1.13 eV, signals at both the front and near the back contact region are detected, whereas at 0.97 eV a strong luminescence is observed at a broad middle region of the absorber.

In order to evaluate the changes along the vertical axis only, monochromatic CL line scans were performed by simply projecting the image data to the vertical  $z$ -axis (summing up all columns). Thus, the CL intensity at a fixed detection energy has been ex-

tracted as a function of the excitation depth from the monochromatic images shown in Fig. 2 and is displayed in Fig. 3. The profiles at 1.30 and 1.13 eV show a one- and two-peak structure, respectively, representing the luminescent layers in the corresponding images; the emission at 0.97 eV is rather broadly distributed over the complete layer, as also can be seen in Fig. 2. Depths of 690 nm ( $E_1$ ), 60 nm and 1560 nm ( $E_2$ ) as well as 1980 nm ( $E_3$ ) are obtained for the energies  $E_1$ ,  $E_2$  and  $E_3$ , respectively.

From the dominance of the emission at 0.97 eV we deduce a drift of excited carriers toward the minimum of the band-gap, which is presumed to be due to the varying electrochemical potentials within the absorber layer. This is a direct evidence for significant charge carrier motion in the CIGSe absorber being present even at low temperatures. Consequently, it is concluded that the grain-like structure observed in Fig. 2(d) may not correspond to the real grain

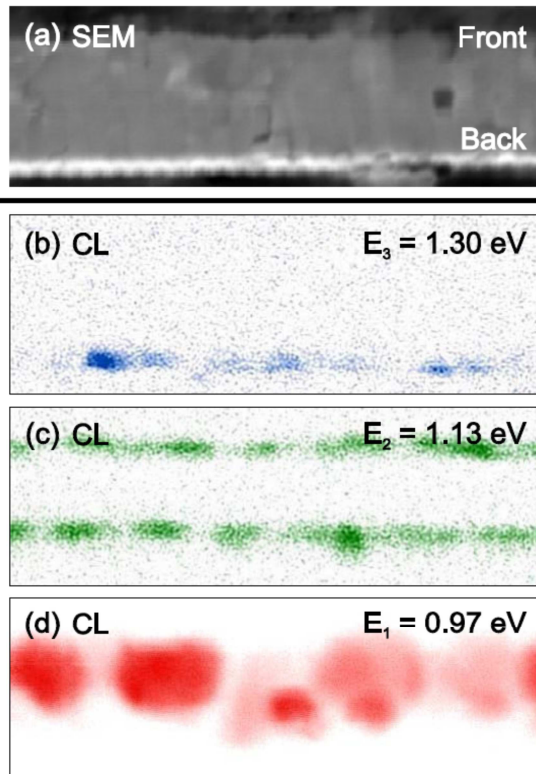


**Fig. 2:** Cross-section images of a standard CIGSe solar cell in secondary electron (a) and monochromatic CL modes (b)–(d). The CL images were detected at the fixed energies  $E_1$ ,  $E_2$  and  $E_3$ .

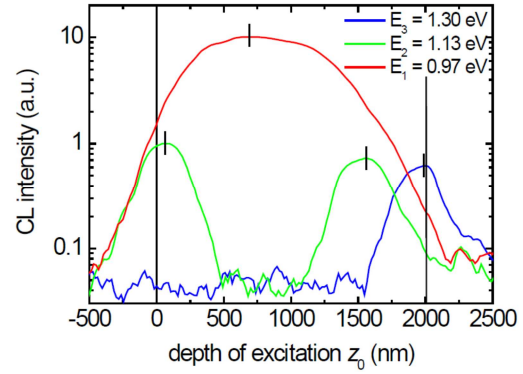


**Fig. 3:** CL depth profiles across the cross-section sample obtained from monochromatic images shown in Fig. 2. The depths of maximum intensity are marked by vertical black lines.

structure due to charge-carrier drift.

The Ga-grading in CIGSe layers is shown to strongly influence its luminescence properties. The knowledge of the Ga-grading inherent in the film is essential for understanding the luminescence signal coming from it and, hence, for an efficient control of the grading in high-efficiency solar cells by luminescence methods. Significant drift of excited charge carriers toward the minimum of the band-gap was observed, being consistent with a drift through forces induced by the vertical grading in electron affinity in the layer. Monochromatic CL imaging has been shown to be able to map the band-gap grading in CIGSe absorber layers. Disregarding the influence of the grading on the peak energy and charge carrier transport may lead to misinterpretation of luminescence spectra as found in recent literature [6,7].

## References

- [1] M. Gloeckler et al., *J. Phys. Chem. Solids* **66** (2005) 1891
- [2] M.A. Green, *Prog. Photovoltaics* **17** (2009) 57
- [3] C.A. Kaufmann et al., *Sol. Energy Mater. Sol. Cells* **93** (2009) 859
- [4] J. Windeln et al., 24th European Photovoltaic Solar Energy Conference, 2009, p. 2443
- [5] J. Haarstrich et al., *Sol. Energy Mater. Sol. Cells* **95** (2011) 1028
- [6] S. Ishizuka et al., *J. Appl. Phys.* **106** (2009) 034908
- [7] M. Pawlowski et al., *Thin Solid Films* **519** (2011) 7328

# Phosphorus doping of CdTe thin film solar cells

C. Kraft, C. Stolze, C. Heisler, C. Ronning, W. Wesch

Cadmium telluride (CdTe) is a frequently used material which can be used in its single crystalline type for detector applications in the infrared range [1] as well as in the x-ray and gamma range [2]. For this purpose it is alloyed with (Cd, Hg) Te and (Cd, Zn) Te, respectively. Polycrystalline CdTe (pc-CdTe) is commonly used as absorber material for solar cells. Due to the phase diagram, the doping or alloying of pc-CdTe is technically difficult to achieve [3]. In order to achieve in-situ doping of the polycrystalline material, a new concept for the deposition of CdTe has been developed [4]. Whereas the highest efficiency on undoped CdTe layers is nearly 17 % on a laboratory scale [5], the doping of pc-CdTe with group-V elements like nitrogen or phosphorus theoretically promises efficiencies of about 20 % [6] by increasing the intrinsic doping level of approximately  $10^{14} \text{ cm}^{-3}$  [7] by some orders of magnitude.

Undoped solar cells with absorber layers, which were produced in the new evaporation chamber show proper current-voltage-(I-V) characteristics with conversion efficiencies of almost 12 % (see Fig. 1). In the following the absorber layers were doped with different contents of phosphorus. The phosphorus is provided by a custom-built evaporation source (P-source) utilizing the inhomogeneous evaporation of GaP. The partial pressure of phosphorus can be detected by a mass spectrometer. The higher the temperature of the GaP source is chosen, the higher is the phosphorus partial pressure, and thus, the higher is the phosphorus content. The source temperature was varied between 200 °C and 800 °C wherein the absolute content of phosphorus has not

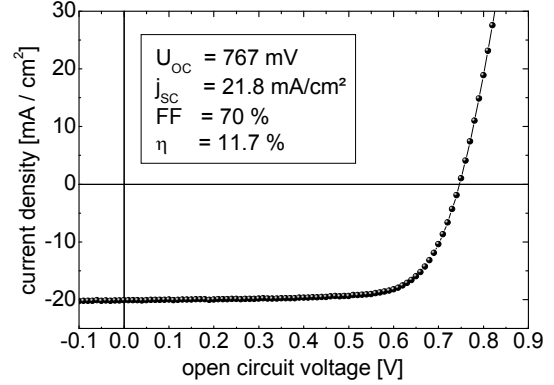


Figure 1: I-V-characteristic of a solar cell with an absorber layer which was deposited in the new evaporation device.

been measured so far. Solar cells were prepared by applying an activation step and a back contact to the absorber layers. The influence of the phosphorus content (i.e. the P-source temperature) on the efficiency of the respective solar cells is shown in Fig. 2. The figure displays the mean values and the standard deviation of the efficiencies of several contacts from one solar cell. For P-source temperatures of up to 300 °C no sig-

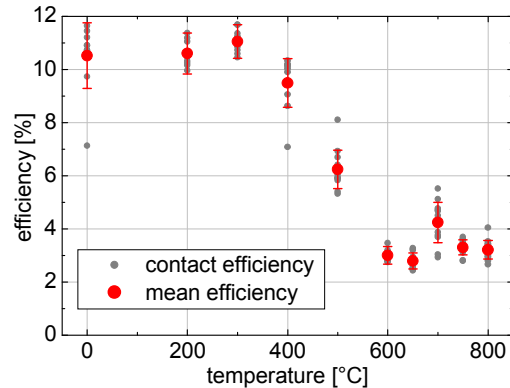


Figure 2: Shape of the efficiency of in-situ phosphorus doped CdTe solar cells. The shapes of the single parameters  $V_{OC}$ ,  $J_{SC}$  and FF show comparable characteristics.

nificant change in the I-V-characteristics can be measured. For temperatures of 400 °C a small decrease and for temperatures of over 500 °C an abrupt and strong

decrease of the efficiency is observed. Obviously, the phosphorus doping has a strong influence on the I-V-characteristics of the solar cells. Even though the phosphorus incorporation induces low efficiencies, the diode characteristics of the cells are remarkable, since the well-known roll over effect of the dark characteristics is the more pronounced, the higher the phosphorus content should be due to the higher P-source temperature (data not shown). That implies that the Schottky barrier at the back contact is increased due to the phosphorus incorporation. Under illumination, however, the roll over vanishes for all of the observed I-V-characteristics (see [8]). The reason for that behaviour possibly is the illumination dependent behaviour of the incorporated charge carriers. They act as acceptor-like defects which are activated under illumination and thus reduce the back contact barrier. That assumption can be verified by the measurement of the external quantum efficiency (EQE). If there are illumination activated defects near the back contact, a raise of the EQE for higher wavelengths can be estimated [9]. Fig. 3 shows that the quantum efficiencies do not change for P-source temperatures of less than 400 °C but then strongly decrease. Additionally, it can be observed for higher P-source temperatures, that the EQE is actually rising with higher wavelengths.

In conclusion it can be stated, that the incorporation of phosphorus strongly influences the electrical characteristics of the CdTe layers. However, the detailed depth-dependent behaviour of phosphorus in CdTe still has to be investigated by means of SIMS, capacitance-voltage measurements and space-resolved Photoluminescence and Cathodoluminescence measurements.

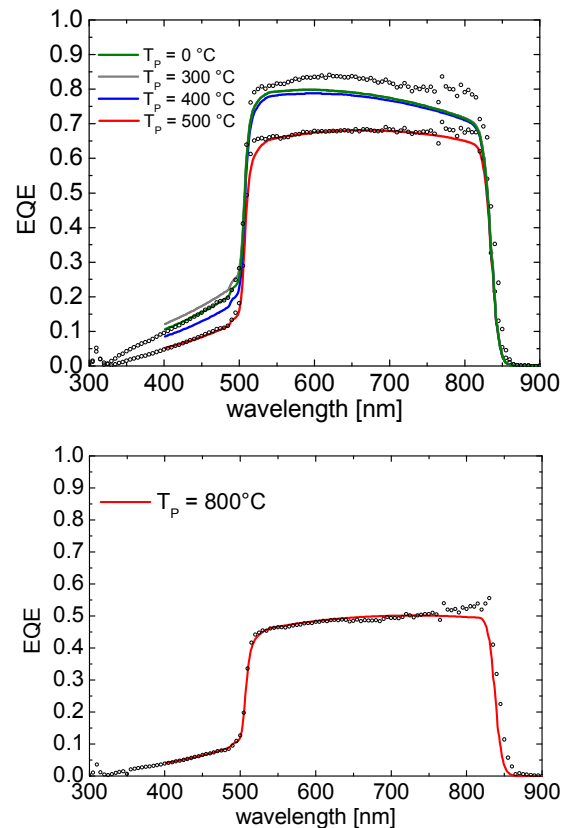


Figure 3: External quantum efficiency of differently phosphorus doped samples compared to the respective fitted spectra.

## References

- [1] W.D. Lawson et al., *Journal of Physics and Chemistry of Solids* 9 (1959) 325.
- [2] T.E. Schlesinger et al., *Materials Science and Engineering* 32 (2001) 103.
- [3] C. Kraft et al., *Phosphorus Implanted Cadmium Telluride Solar Cells*, IFK annual report (2010).
- [4] C. Kraft et al., *Design of a High Vacuum Chamber for Cadmium Telluride Evaporation and Doping*, IFK annual report (2009).
- [5] W. Wu et al., in *17th EPSEC* (IEEE Press, Munich, Germany, 2001) pp. 22-26.
- [6] J.R. Sites, J. Pan, *Thin Solid Films*, 515 (2007) 6099.
- [7] U. Reislöhner et al., *Thin Solid Films* 515 (2007) 6175.
- [8] C. Stolze, Bachelor Thesis, *Phosphordotierung von CdTe-Dünnschichtsolarzellen*, Jena 2011.
- [9] M. Köntges et al. *Thin Solid Films* 403 (2002), 280.

# Photoluminescence of the back and front side of Cu(In,Ga)Se<sub>2</sub> absorbers

S. Schönherr, J. Haarstrich, H. Metzner, C. Ronning, T. Rissom\*, C.A. Kaufmann\*,  
H.W. Schock\*

\* Helmholtz-Zentrum Berlin für Materialien und Energie, Hahn-Meitner-Platz 1, 14109 Berlin

In high efficiency Cu(In,Ga)Se<sub>2</sub> solar cells the ratio  $[Ga]/([Ga]+[In])$  (GGI) varies with depth and a grading in composition is present. Therefore, the grading in composition also introduces a grading in the band-gap (CuInGaSe<sub>2</sub>  $E_g=1.049\text{eV}$ , CuGaSe<sub>2</sub>  $E_g=1.7305\text{eV}$  [1]). Hence, a detailed study of the band-gap variation through the addition of gallium is needed by different characterization techniques. The gallium grading as function of the depth has been measured previously by EDS measurements [2]. The shape of the grading shows an increased GGI at the front and the back where the gallium concentration is higher at the back side of the absorber. Cathodoluminescence spectra shows a corresponding behaviour with a higher photon energy at the back of the layer [2]. This peak shift was also seen in photoluminescence (PL) studies but wasn't investigated in detail [6, 7]. In this study, the effect of the Ga-grading on the photoluminescence (PL) properties of CIGSe is investigated. In addition the CIGSe layers were excited by a tuneable light source and photoluminescence excitation spectra were calculated for different detection energies.

CIGSe thin-films with a thickness of about 2  $\mu\text{m}$  were prepared by multi-stage co-evaporation onto Mo-coated soda-lime glass with a measured GGI=0.269. Solar cells made from these absorbers using the standard ZnO/CdS window structure how efficiencies up to 17%. [3]

In photoluminescence method, electron-hole pairs are excited by light sources with non-varying excitation energy and their radiative recombination is observed spectrally. In contrast, photoluminescence excita-

tion method uses spectral tuneable light sources and their radiative recombination carried out at fixed detection energy. The samples were mounted in a LHe flow cryostat and studied by 3.5 K. Photoluminescence spectra were measured from the front and the back site of the Cu(In,Ga)Se<sub>2</sub> absorber layers by different spectral illumination of a Xe-flash lamp.

The Photoluminescence spectra shown in Fig. 1 on a logarithmic scale were detected on standard samples in front and back geometry.

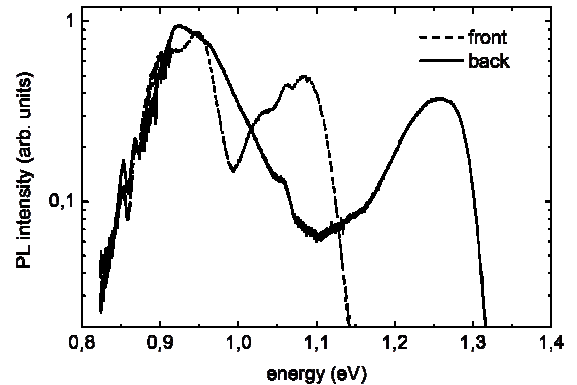


Fig. 1: Photoluminescence spectra measured at 3.5K and illuminated by 600nm from front and back-sides of CIGSe layers

There is not a single peak as known from previous luminescence of Cu-poor CIGSe material [4]. The front side spectrum is dominated by two emission peaks  $E_1=0.946\text{ eV}$  and  $E_2=1.082\text{ eV}$ . The first one ( $E_1$ ) roughly corresponds to the DA1-transition (donor-acceptor-transition) of pure CuInSe<sub>2</sub> (GGI=0) [2, 5]. The second emission ( $E_2$ ) can be assigned to the DA1-transition with a GGI of around 0.3 [2]. Additional peaks are present at  $E_3=0.908\text{ eV}$ ,  $E_4=1.031\text{ eV}$  and  $E_5=1.062\text{ eV}$  where  $E_4$  and  $E_5$  could also be assigned to the DA1-transition with a GGI lower 0.3. Excitation from the back of

the layer yields a second peak at  $E_6=1.257$  eV, corresponding to a GGI of roughly 0.55.

Photoluminescence spectra from the back side of a CIGSe layer were measured under different excitation wavelengths. For normalization the Xe-flash lamp spectrum was characterized in detail by single spectra at the corresponding wavelengths and the respective intensity was determined by inte-

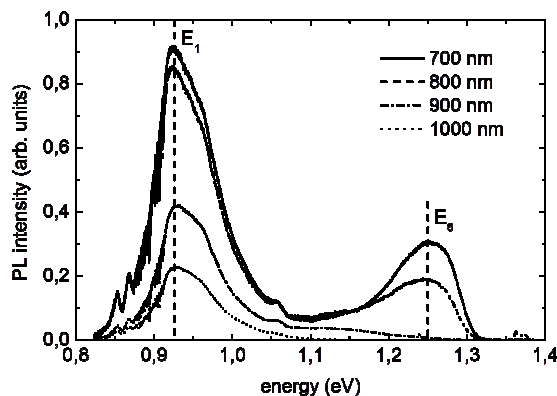


Fig 2: Photoluminescence spectra from the back side of a CIGSe layer measured at 3.5K with different excitation wavelengths

gration of the intensity.

The photoluminescence spectra under different excitation wavelengths are exemplarily shown in figure 2 with four different excitation wavelengths. As seen the spectrum intensity decreases completely with increasing excitation wavelength. At low wavelengths the two dominating peaks are present as seen in figure 1. However the separate peak energies strongly decrease with increasing excitation wavelengths, first the peak at  $E_6=1,257$  eV, next  $E_1=0.946$ . As can be seen that the detected peak intensity fall too zero although the excitation energy is still greater than the peak energy. Hence, the absorption doesn't occur in the same stats as they recombine. The main part of the absorption proceeds via the band-gap. At low temperature as used 3.5 K, the generated carrier falls more quickly into donor and acceptor stats than they recombine via band-to-band recombination.

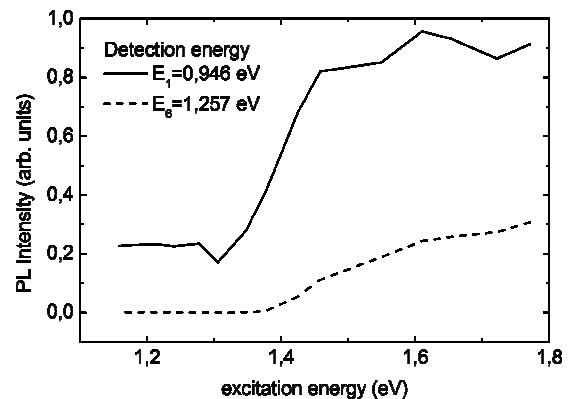


Fig 3: Photoluminescence excitation spectra of the back side of a CIGSe layer measured at 3.5K at different detection energies

With the measured spectra at different excitation wavelengths it was possible to compile photoluminescence excitation spectra at arbitrarily detection energies. In figure 3 the typical peak energies  $E_1$  and  $E_6$  were chosen and evaluated as function of the excitation energy. The accuracy is in the same magnitude of the noise. As expected the peak intensity increases with increasing excitation energy. Both curves decreases simultaneously till the curve of the detection energy  $E_6$  has fallen to zero. At this point the detection energy of the DA1-transition with a GGI of 0.3 reaches a constant level till the excitation energy becomes too small.

## References

- [1] A.V. Mudryi, I.V. Bodnar, V.F. Gremenok, I.A. Victorov, A.I. Patuk and I.A. Shakin, *Solar Energy Materials and Solar Cells* **53** (1998) 247-253
- [2] J. Haarstrich, H. Metzner, C. Ronning, A. Undisz, T. Risam, C.A. Kaufmann, H.W. Schock, *Thin Solid Films* (2012) doi:10.1016/j.tsf.2011.12.2012
- [3] C.A. Kaufmann, R. Caballero, T. Unold, R. Hesse, R. Klenk, S. Schorr, M. Nichterwitz, H.-W. Schock, *Sol. Energy Mater. Sol. Cells* **93** (2009) 859
- [4] S. Shirakata, K. Ohkubo, Y. Ishii, T. Nakada, *Solar Energy Materials & Solar Cells* **93** (2009) 988-992
- [5] S. Siebentritt, N. Rega, A. Zajogin, M.Ch. Lux-Steiner, *phys. stat. sol. (c)* **1**, No. 9, 2304- 2310 (2004)
- [6] M. Park, S. Ahn, J. Yun, J. Gwak, A. Cho, S. Ahn, K. Shin, D. Nam, H. Cheong, K. Yoon, *Journal of Alloys and Compounds* **513** (2012) 68- 74
- [7] M. Venkatachalam, M.D. Kannan, S. Jayakumar, R. Balasundaraprabhu, N. Muthukumarasamy, *Thin Solid Films* **516** (2008) 6848-6852



# Organic Heteroepitaxy of PTCDA and SnPc on Single Crystalline Silver

Marco Grünewald, Roman Forker, and Torsten Fritz

In recent years organic thin films have been established in applications such as light emitting diodes (OLED), field effect transistors (OFET) and photovoltaic devices [1-3]. The understanding of the interaction mechanisms within a molecular layer but also at metal-organic and organic-organic interfaces is of fundamental importance to improve the efficiency of organic semiconductor components in the future.

The electronic as well as the optical properties of thin organic layers are determined significantly by the molecular arrangement. In order to analyze the complex molecular interaction mechanisms affecting the properties of the thin film we focus on model systems composed of highly-ordered ultra-thin molecular layers of the dye molecules 3,4,9,10-perylene-tetracarboxylic-dianhydride (PTCDA) and tin(II)-phthalocyanine (SnPc) prepared by molecular beam epitaxy (OMBE). Those molecules are suitable as they are known for an epitaxial growth on single crystalline silver [4,5].

Our group established an *in situ* optical absorption spectroscopy for the determination of optical properties of thin organic films known as Differential Reflectance Spectroscopy (DRS) [6]. The measured quantity, the differential reflectance spectrum (DRS), is rather

simple:

$$DRS := \frac{R(E, d) - R(E, d = 0)}{R(E, d = 0)} \quad (1)$$

where  $R(E, d)$  denotes the reflectance of the substrate inclusive the thin film with a thickness  $d$ . Accordingly,  $R(E, d = 0)$  can be understood as the reflectance of the pristine substrate depending on the photon energy  $E$ . As both the signal height and the spectral shape of the DRS strongly depend on the optical properties of the substrate, it is far from trivial to interpret the DR spectra itself in terms of light absorption. Instead of this, a numerical algorithm [7] has been developed by us in order to extract the real and imaginary part of the complex dielectric function  $\hat{\epsilon} = \epsilon' - i\epsilon''$  of the thin film.

On the way to organic heterostructures, a one monolayer (ML) thin film of PTCDA and SnPc on Ag(111) have been investigated optically. One obtains almost identical, nearly structureless and rather broad  $\epsilon''$  spectra within the first monolayer in contrast to the monomer (single molecule) spectra of the respective molecules as shown together in Fig. 2. The considered molecules are already known for a strong electronic interaction with an Ag(111) surface according to a hybridization of the metal wavefunction and the molecular orbitals [8,9]. Hence, the molecules which are in contact with an Ag(111) surface does not behave like PTCDA or SnPc monomers anymore.

Surprisingly, in the second monolayer the situation changes dramatically. Regardless of which of those molecules are present in the first monolayer, the molecules in the second monolayer are efficiently electronically and optically decoupled

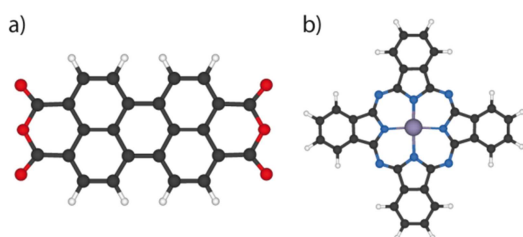


**Fig. 1:** The used molecular substances: **a)** 3,4,9,10-perylene-tetracarboxylic-dianhydride (PTCDA) and **b)** tin(II)-phthalocyanine (SnPc)

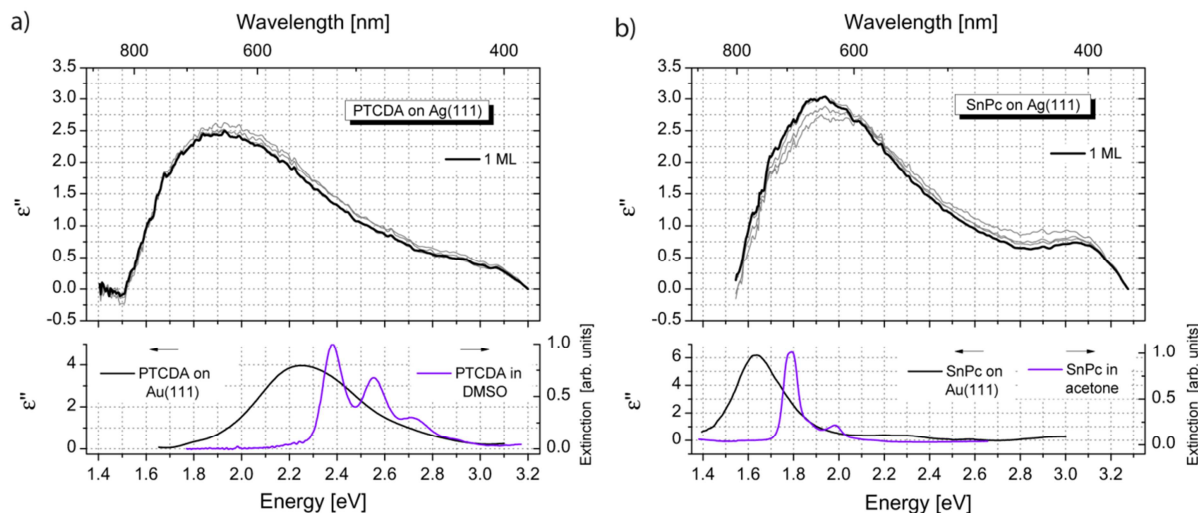


**Fig. 2:** The imaginary part  $\epsilon''$  of the dielectric function (top panel) of **a)** a 1 ML PTCDA and **b)** a 1 ML SnPc film on Ag(111) is shown together with extinction spectra of the respective molecules in solution (bottom panel). A strong metal-molecule interaction is manifested in broad and structureless  $\epsilon''$  spectra. In contrast to this, the interaction is weak in case of PTCDA and SnPc on Au(111): There, the  $\epsilon''$  spectra are energetically related to the monomer features but broadened likewise.

from the metal substrate as well as from the first monolayer. Therefore, a monomer spectrum is obtained initially in the 2<sup>nd</sup> monolayer as shown in Fig. 3 using the example SnPc on a one monolayer PTCDA film on Ag(111).

Arising from a layer-by-layer growth the monomer features are present until the first monolayer of SnPc is completed, and subsequently a formation of aggregates occurs during the deposition of further

SnPc molecules. For a film thickness beyond 4 ML the spectra converges asymptotically into the well-known phthalocyanine bulk spectrum [3].

The present work gives an insight into the complex interaction mechanisms at metal-organic and organic-organic interfaces. For instance, an interlayer of molecules, not necessarily the same species, modifies the electronic structure of metal surfaces comprehensively and provides a great potential to affect further molecular layers electronically (and thus optically) and structurally as well.

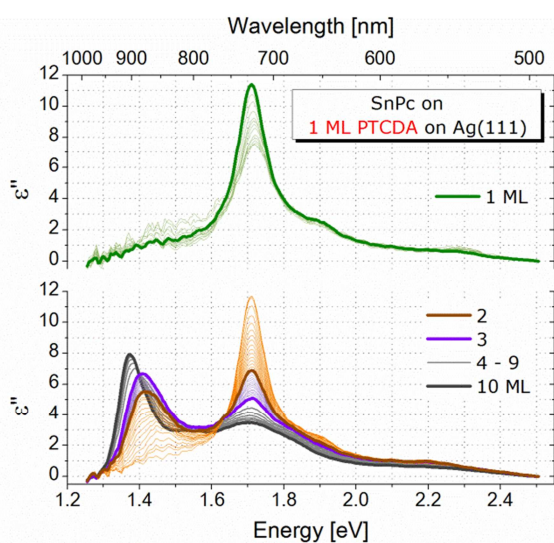


**Fig. 3:** The imaginary part  $\epsilon''$  of the dielectric function of a SnPc layer on a 1 ML PTCDA film on Ag(111) over a wide film thickness range covering submonolayers up to 10 ML.

## References

- [1] S. Liu *et al.*, *Adv. Mater.* **21**, 1217-1232 (2009).
- [2] N.R. Armstrong *et al.*, *Macromol. Rapid Commun.* **30**, 717-731 (2009).
- [3] B. Rand *et al.*, *Appl. Phys. Lett.*, **87**, 33508 (2005).
- [4] C. Stadler *et al.*, *Nat. Phys.* **5**, 153-158 (2009).
- [5] L. Kilian *et al.*, *Surf. Sci.* **573**, 359-378 (2004).
- [6] R. Forker *et al.*, *PCCP* **11**, 2142 (2009)
- [7] R. Nitsche *et al.*, *Phys. Rev. B* **70**, 195432 (2004).
- [8] M. Häming *et al.*, 174 (2009).
- [9] M. Häming *et al.*, *Surf. Sci.* **604** (2010).

# Quantification of LEED Measurements for Investigations of Organic Thin Films

Falko Sojka, Matthias Meissner, Marco Gruenewald, Roman Forker, and Torsten Fritz

Low Energy Electron Diffraction (LEED) on epitaxial layers is a powerful tool to examine long-range ordering at the interface. However, due to limitations like distortion of the LEED images, often additional efforts have to be made in order to derive precise epitaxial relations.

Often, the potentially high accuracy of LEED instruments is not reached, due to the neglect of systematic errors which can actually be accounted for.

We developed and implemented an algorithm to determine and correct systematic distortions in LEED-images. The procedure is independent of the design of the device (i.e., conv. LEED, MCP-LEED, SPA-LEED). Therefore, only a calibration sample with a well-known structure and a suitably high number of diffraction spots, i.e. Si(111)-7x7 (Figure 1), is required. Exemplarily, we will discuss results obtained for an MCP-LEED from Omicron [1].

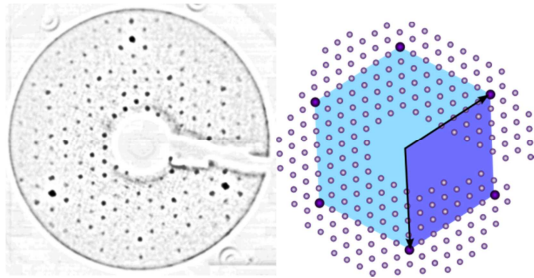


Fig. 1: LEED image of Si(111)-7x7 at 75.2 eV (left) and geometric simulation (right).

We first distinguish between a radially symmetric and an asymmetric distortion. A **radial symmetric distortion** is generally present, e.g. caused by the lens of the recording camera. Figure 2 shows the measured radial symmetric distortion. A distinction has to be made between measurements with and without

suppressor. The results show that this radial symmetric distortion is not only of optical origin.

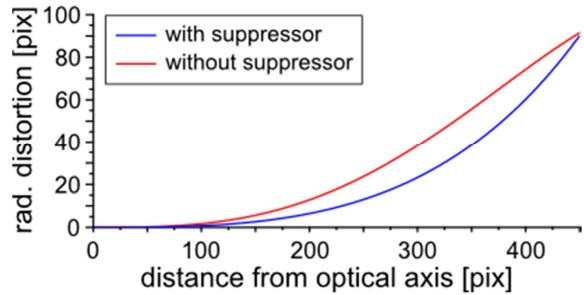


Fig. 2: Radial symmetric distortion for two different suppressor settings.

A measurable **asymmetric distortion** arises only in measurements with suppressor. Figure 3 shows the measured asymmetric distortion as a vector field.

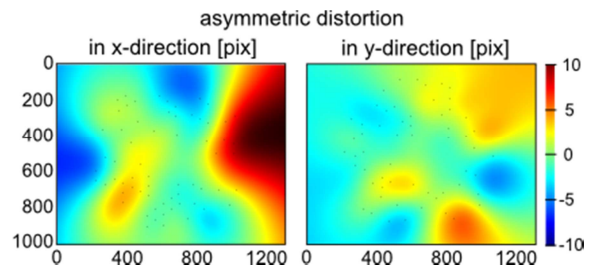
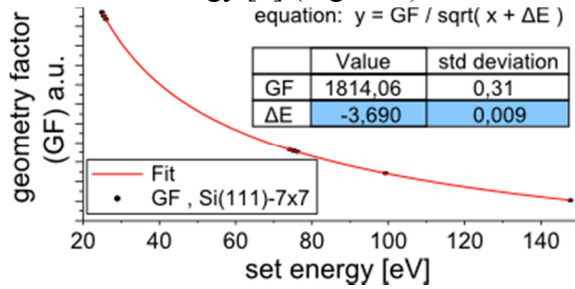


Fig. 3: Asymmetric distortion.

The diameter of the LEED screen in an image is about 950 pixels. The average discrete asymmetric distortion was more than 3.5 pixels. After correction of the LEED images, the remaining inaccuracy is less than 2 pixels.

One other systematic error that can occur is the **energy offset**. A difference  $\Delta E = (-3.690 \pm 0.009)$  eV between the true kinetic energy of the electrons and the set acceleration voltage was found. This offset is specific to each device and can only be determined through a series of measurements with a calibration sample at different energies. The size of the reciprocal lattice

imaged is proportional to the reciprocal root of the energy [2] (Figure 4).



**Fig. 4:** Determination of the energy offset. The geometry factor ( $GF$ ) is proportional to the size of the reciprocal lattice imaged.

Additionally, we found an **axial distortion** which arises if a sample surface is tilted during the measurement. This axial distortion can be described theoretically with the Ewald Construction, and thus it is possible to correct those measurements.

Figure 5 shows our *ansatz* of the description. The reciprocal lattice rods are aligned vertically to the sample surface and are tilted with the sample. Thus, the rods are not perpendicular to the plane of the screen anymore.

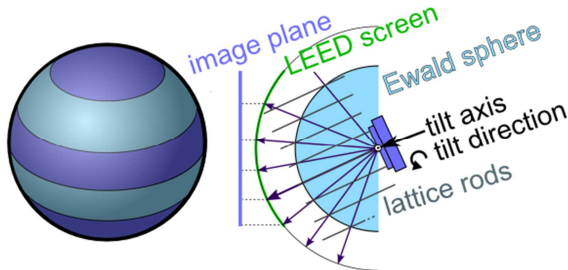


**Fig. 5:** Ewald construction considering a tilted surface (right) and projection of a tilted, striped ball to illustrate the axial distortion (left).

Consequently, the reciprocal lattice imaging will be compressed nonlinearly along the tilt direction. In addition, the imaging is symmetrically curved to the tilt direction. The strength of the distortion depends on the geometry of the device and the tilt angle. After the determination of two geometry parameters and the tilt angle, the LEED image can be corrected.

With respect to all these systematic errors, a correction of the LEED images is

practicable. After that, a relative accuracy of the lattice parameter determination better than 1% can be achieved.

The knowledge gained was applied to determine the lattice of a PTCDA phase on epitaxial graphene accurately, which was recently discovered by M. Meissner in 2010. LEED images of this phase were corrected for all of these systematic errors and subsequently analyzed, using a homemade computer software. This type of analysis is faster and protects against subjective influences caused by the experimenter.

For these phase we found the epitaxial matrix to be

$$C = \begin{pmatrix} 1.76 \pm 0.03 & 3.98 \pm 0.05 \\ -8.80 \pm 0.12 & 6.93 \pm 0.11 \end{pmatrix}.$$

Within the margin of error this constitutes a Point-on-Line phase [3] of PTCDA on graphene with the second column consisting of integers. The unit cell has the dimensions  $a_1 = (12.42 \pm 0.10) \text{ \AA}$ ,  $a_2 = (19.56 \pm 0.21) \text{ \AA}$ .

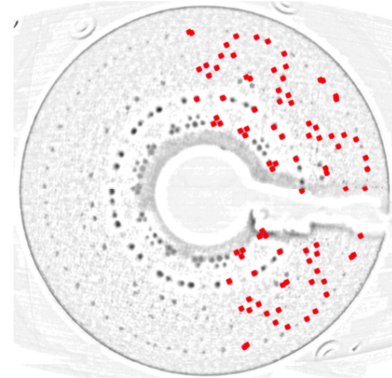


**Fig. 6:** LEED image of PTCDA at 36.0 eV. The red simulation describes the structure discovered by Meissner. Simulation with *LeedSim* [4].

## References

- [1] Omicron NanoTechnology: *MCP-LEED Optics and Electron Gun: User's Guide 1.0*, (2006).
- [2] S. C. B. Mannsfeld: *Diplomarbeit*, TU Dresden (1999).
- [3] S. C. B. Mannsfeld, K. Leo, and T. Fritz, *Phys. Rev. Lett.* **94**, 056104 (2005).
- [4] S. C. B. Mannsfeld: *LeedSim* (2010).

# Enhanced photoluminescence from Si nanocrystals deposited on ZnO Nanowires

K. Potrick, R. Röder, A. Thielmann, C. Ronning, and F. Huisken

Silicon nanocrystals (Si NCs) in the size range of 3 to 8 nm show photoluminescence (PL) in the visible to near infrared range with high quantum efficiency [1]. The PL is governed by the radiative recombination of quantum-confined (QC) excitons. This makes Si NCs a model system for the study of QC PL of an indirect semiconductor. Moreover, nanostructured silicon is an interesting material for various practical applications.

Studying the interaction of Si NCs with other nanostructures leads to a better understanding of the fundamental processes involved and paves the way to the design and fabrication of devices for practical applications. In the present project, we investigated the role of zinc oxide nanowires (ZnO NWs) on the PL properties of Si NCs.

The Si NCs were prepared by laser-induced pyrolysis of silane in a cluster beam apparatus and deposited under vacuum on ZnO NWs with defect-rich surfaces grown on a Si wafer by a vapor-liquid-solid process. Simultaneously, the Si NCs were deposited on a fused silica (FS) window covering half of the ZnO NWs and serving as a reference sample. The deposition time of 3 h resulted in a layer thickness of approximately 350 nm. In Fig. 1, a photograph of the samples under UV light (406 nm) is shown together with a SEM image of the ZnO NW substrate.

The PL of these samples is studied in the frequency and time domains. As excitation sources, a continuous-wave diode laser (Coherent, model Cube 405-50C) operating at  $\lambda = 406$  nm and the fourth harmonic of a pulsed Nd:YAG laser (266 nm, 20 Hz, 5 ns pulse width) are used. The emitted light

is collected with a lens adapted to an optical fiber and analyzed with a spectrometer (Ocean Optics, model QE65000) or a monochromator equipped with a photomultiplier tube.

The PL spectra shown in Fig. 2 are corrected for the system's sensitivity and collected under the same conditions at room temperature with an integration time of 200 ms under excitation with the diode laser operated with an intensity of 73 mW/cm<sup>2</sup>. The measured PL intensity (integrated area under the PL curve) arising from the Si NCs on the ZnO NW substrate (dark solid line) is 7.7 times higher than the intensity of the Si NCs on the FS substrate (dashed line). Whereas the shape of the PL curves remains unchanged, only a slight blue shift of 13 nm from 798 to 785 nm is observed. Also shown is the PL arising from surface defects of the ZnO NWs measured on the ZnO NW substrate in the area that was protected from Si NC deposition by the FS window (light solid line).

One process possibly responsible for the enhancement of the Si NC PL is the Förster

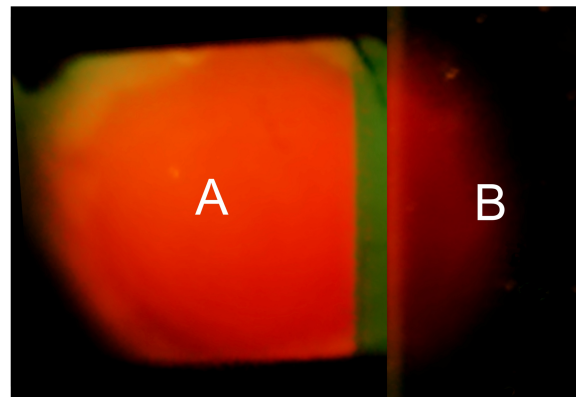


**Fig. 1:** Photograph of the two samples studied upon UV illumination. In sample A, the Si NCs are on top of a layer of ZnO NWs while, in sample B, the Si NCs are residing on a FS window. For the photo, sample B has been shifted 0.65 mm to the right relative to its position during the deposition of Si NCs.

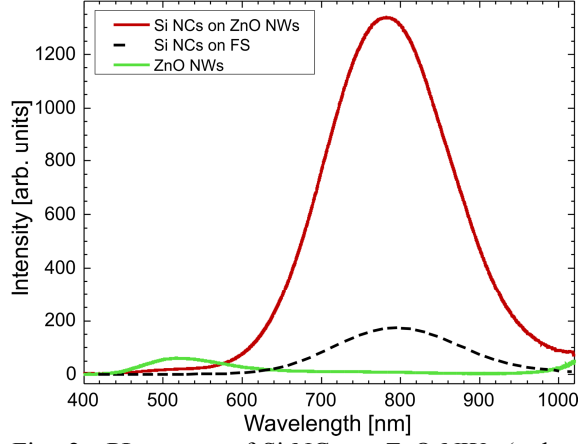


**Fig. 2:** PL spectra of Si NCs on ZnO NWs (red or dark solid line), Si NCs on FS (dashed black line), and ZnO NWs (green or light solid line).

resonance energy transfer (FRET), a non-radiative energy transfer from the surface defects of the ZnO NWs (donor) to the Si NCs (acceptor) by dipole-dipole interaction. A typical signature of energy transfer is an increased decay rate of the donor PL as it acts as an additional channel of relaxation. In the presence of the acceptor, the decay rate of the donor will be  $k_{DA} = k_D + k_T$ , with  $k_D$  and  $k_T$  being the decay rate in absence of the acceptor and the energy transfer rate, respectively. The normalized decay curves are shown in Fig. 3. For these measurements, the pulsed Nd:YAG laser served as excitation source. In the presence of the Si NCs, the decay rate of the ZnO defects is increased from  $k_D = [(12.2 \pm 0.1) \mu\text{s}]^{-1}$  to  $k_{DA} = [(10.6 \pm 0.1) \mu\text{s}]^{-1}$ . Therefore, the transfer rate is calculated to be  $k_T = [(80.8 \pm 0.2) \mu\text{s}]^{-1}$ . The measured decay rates can also be used to determine the efficiency of the energy transfer

$$E = 1 - \frac{k_D}{k_{DA}}$$

to be  $(13 \pm 2) \%$ . Another parameter used to characterize FRET is the Förster distance given by

$$R_0 = 0.0211 (\kappa^2 n^{-4} Q_D J)^{\frac{1}{6}}$$

with  $\kappa^2 = 2/3$  for randomly orientated transition dipoles of the donor and acceptor. The refractive index is assumed to be  $n = 1$

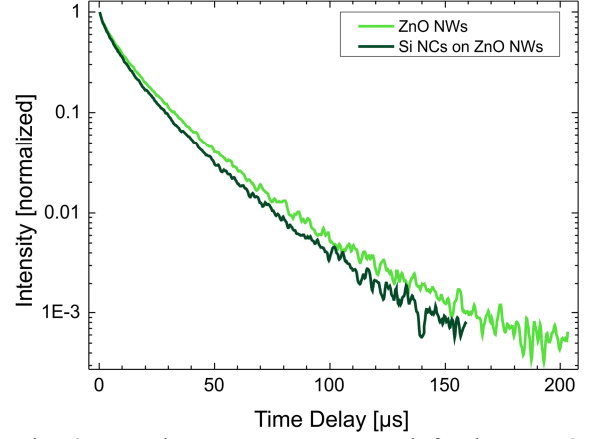


**Fig. 3:** PL decay curves measured for bare ZnO NWs (light green line) and ZnO NWs covered by Si NCs (dark green line) at  $\lambda_{em} = 520$  nm.

and the quantum yield of the donor is  $Q_D = 0.018$  [2]. The overlap integral  $J$  describes the spectral overlap between the donor emission and the acceptor absorption. With these quantities, the value of the Förster distance is evaluated to be  $R_0 = 4.0$  nm. Knowing  $R_0$ , one can also calculate the donor-acceptor distance

$$r_{DA} = \left( k_D \frac{R_0^6}{k_T} \right)^{\frac{1}{6}}$$

being equal to 5.5 nm. This value is somewhat larger than the minimal distance between the ZnO defects and the Si NCs, estimated as the sum of the Si NCs' radius,  $r_{NC} = 2.9$  nm, and the distance of the defects from the ZnO NW surface,  $r_{defect} = 1.6$  nm [3].

In conclusion, the deposition of Si NCs on ZnO NWs results in a 7.7-fold enhancement of the PL of the Si NCs and in a faster decay of the ZnO NWs' defect PL. If compared with the fourfold enhancement observed for Si NCs interacting with a plasmonic nanoporous gold structure [4], this can be considered as a promising result.

## References

- [1] K. Potrick *et al.*, Appl. Phys. Lett. **98**, 83111 (2011).
- [2] A. Dev *et al.*, Nanotechnology **21**, 65709 (2010).
- [3] A. Makhal *et al.*, Nanotechnology **21**, 265703 (2010).
- [4] J. S. Biteen *et al.*, Nano Letters **9**, 1768 (2005).

## Formation of GEMS from interstellar silicate dust

C. Jäger, T. Sabri, F. Huisken, Th. Henning\*, and E. Wendler

\*Max-Planck-Institut für Astronomie, Königstuhl 17, 69117 Heidelberg

Glass with embedded metal and sulfide grains (GEMS) are the most abundant isotopically anomalous grains in interplanetary dust particles, but their presolar origin is not completely proven [1,2]. Cosmic silicates are mainly formed via gas-phase condensation in circumstellar shells of evolved oxygen-rich stars. Different silicates produced in our laboratory and resembling the silicate materials identified in evolved stars has been used to study the formation of GEMS from presolar or circumstellar silicates by ion irradiation. Cosmic abundant ions such as  $H^+$  and  $He^+$  with low and high energy and heavier  $Ar^+$  ions have been applied to simulate the processing of silicate in the interstellar medium.

In our laboratory, different silicates have been produced by melting and quenching techniques or by gas-phase condensation techniques such as laser ablation. In this process, the freshly condensed grains were adiabatically extracted through a nozzle and a skimmer from the condensation zone and finally deposited with a definite layer thickness on glassy carbon substrates. For the irradiation experiments, the 400 keV implanter ‘Romeo’ has been applied. In a first series of irradiation experiments, the produced glassy samples were exposed to 95 and 190 keV  $H^+$  bombardment. Reflection spectroscopy in the IR range has been used to demonstrate the chemical and structural modifications in the implanted glassy silicate layers (see Fig. 1). The ion-induced processing in the glassy solids is correlated to the formation of a structure that consists of offended and unoffended layers. The effective dielectric function of the offended layer can be determined by the effective

medium theory, in particular by the Bruggemann model that is able to simulate the observed changes in an inhomogeneous layer consisting of a magnesium iron silicate matrix and spherical metallic iron inclusions.

$$\epsilon_{eff} = \epsilon_m + \frac{3f\epsilon_m \frac{\epsilon - \epsilon_m}{\epsilon + 2\epsilon_m}}{1 - f \frac{\epsilon - \epsilon_m}{\epsilon + 2\epsilon_m}}$$

$\epsilon_{eff}$  and  $\epsilon$  are the dielectric functions of the effective medium and of the spherical inclusions, respectively. The quantity  $f$  represents the filling factor of the layer.

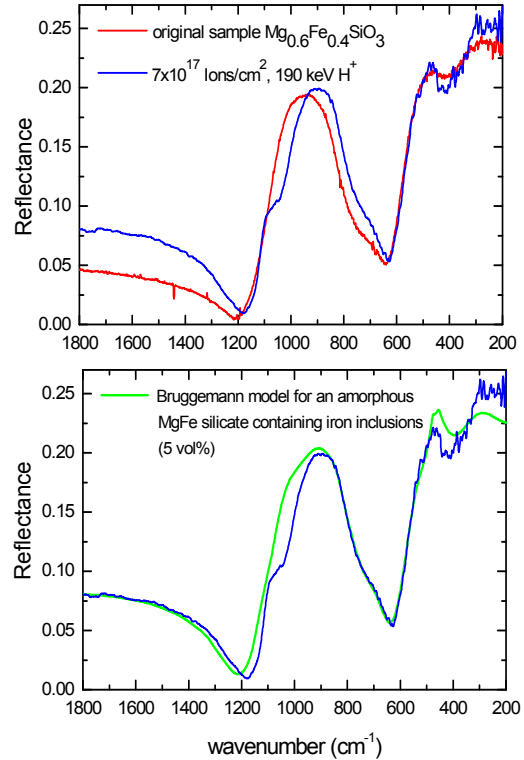


**Fig. 1:** The upper panel shows the IR reflection spectra of non- and ion-irradiated  $Mg_{0.6}Fe_{0.4}SiO_3$  glass. The lower panel displays the fit of the reflectance spectrum of the irradiated silicate with a 3-layer structure consisting of an around 800 nm undisturbed layer of  $Mg_{0.6}Fe_{0.4}SiO_3$  (L1), a 250 nm layer containing iron inclusions and finally an extended non-offended layer L1.

The layer thicknesses of the offended layers were adapted to the calculated penetration depth of the 95 and 190 keV protons in the irradiation experiments. The performed ion-irradiation experiments have revealed consistent modifications in the IR spectra of all irradiated silicates. Fig. 1 shows the modification of the reflectivity of a silicate glass due to ion irradiation with  $1.0 \cdot 10^{17}$  protons/cm<sup>2</sup>. The increase of the reflectivity at wave numbers smaller than 1200 cm<sup>-1</sup> can be explained with the formation of iron inclusions and the measured spectrum can be reproduced with a silicate containing 5 vol% of spherical iron particles. The IR results of these studies clearly show the reduction of the incorporated ferrous or ferric ions due to H<sup>+</sup> irradiation. High-resolution transmission electron microscopy studies (HRTEM) of the irradiated silicate splats have proven the existence of 2-3 nm sized metallic iron inclusions. A second series of bombardment experiments has been performed by using a two-beam irradiation chamber which is coupled to the beam lines of a 400 kV implanter and a 3 MV Tandron accelerator for in situ ion implantation and Rutherford backscattering spectroscopy (RBS). Amorphous nanometer-sized olivine particles deposited on glassy carbon substrates were irradiated with 90 keV Ar<sup>+</sup> ions at 16 and 300 K, respectively. The study has been conducted in four steps with a total dose of  $1.1 \cdot 10^{16}$  Ar<sup>+</sup> ions/cm<sup>2</sup>. In addition, the processing of olivine particles by 10 keV protons (total dose of  $1 \cdot 10^{17}$  H<sup>+</sup> ions/cm<sup>2</sup>, T=16 K) has been studied. The applied dose corresponds to the number of ions accelerated in one shock wave in the interstellar medium [3]. Between individual irradiation steps, RBS measurements with 2.5 MeV helium ions were performed. The RBS spectra taken after the individual irradiation steps show the increase

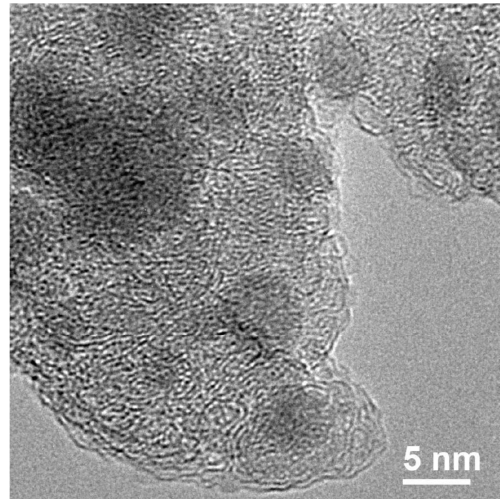


**Fig. 2:** HRTEM micrograph of MgFeSiO<sub>4</sub> particles processed by irradiation with 10 keV H<sup>+</sup> ions. The dark spots represent metallic iron inclusions.

of iron with respect to oxygen, magnesium, and silicon. HRTEM analysis of the irradiated silicate grains (see Fig. 2) show the formation of metallic iron inclusions in the Ar<sup>+</sup> and in the H<sup>+</sup> irradiated silicate samples. The quantitative EDX analysis shows the depletion of oxygen, Mg, and Si relative to iron in the remaining Fe-Mg silicate surrounding the iron inclusions. The same composition can be observed in the presolar GEMS [4]. The reduction of iron as well as the depletion of Mg and Fe relative to silicon can be explained with reduction and sputtering processes. The study clearly demonstrates that ion-induced processing of circumstellar silicates produce GEMS-like silicates, an abundant material that influenced the planet formation process of our solar system.

This work was supported by the DFG grant Hu 474/23-1 within SPP 1385 “The first 10 Million Years of the Solar System—a Planetary Materials Approach”.

## References

- [1] J. Bradley et al. *Science* **307**, 244 (2005)
- [2] P. Hoppe, Origin and early evolution of comet nuclei, Balsiger et al. (eds.), Springer Science (2008)
- [3] A. Jones, *Astrophys. J.* **469**, 740 (1996)
- [4] J. Matzel et al. *LPS XXXIX*, Abs. 2525 (2008)



# Structural modifications of low-energy heavy-ion irradiated germanium

T. Steinbach, J. Wernecke, P. Kluth\*, M. C. Ridgway\*, and W. Wesch

\*Australian National University, Research School of Physics and Engineering, Canberra, Australia

In many crystalline semiconductors ion irradiation with energies of several hundred keV (nuclear energy deposition,  $\epsilon_n$ ) results in amorphization of the material at certain ion fluences. In some semiconductors (e.g., GaSb [1], Ge [2]) further irradiation leads to void formation within the amorphous layer and transformation into a porous structure. The properties of porous semiconductors may differ significantly from their corresponding bulk materials. The utilization of such differences promotes the application of porous structures in advanced technologies [3,4]. Recently, ion beam induced void formation caused by high ion energy irradiation [5] was explained by a shock wave mechanism as a result of high electronic energy deposition [6]. However, the mechanism as well as the parameters for void formation at low ion energies, where  $\epsilon_n$  dominates, are still discussed. In order to get a deeper insight into the mechanism based on nuclear processes the effect was investigated as function of the irradiation parameters (ion species, nuclear energy

deposition, incidence angle and temperature) [7].

Two orders above the amorphization threshold an extreme ion beam-induced volume expansion  $\Delta z$  was observed for all irradiation conditions used. As shown in Fig. 1, the fluence dependence of the step height exhibits three nearly linear regions of  $\Delta z$  [7]. Cs-TEM and -SEM investigations reveal that the structural modification begins with the formation of a distinct porous layer at the surface, which expands in the underlying a-Ge layer with increasing fluence. In addition, at a threshold fluence (region II, cp. Fig. 1, steep slope) buried isolated spherical voids were formed within the previously featureless amorphous Ge layer, having sizes of 5 to 25 nm (cp. Fig. 2). For all iodine irradiations, i.e. independent of energy and incidence angle, the buried voids are located in the depth of the projected ion range. However, ion irradiation with Au und Ag ions results in a comparable volume expansion but not in the formation of buried voids. This leads to the conclusion that chemical properties of the irradiated ions are responsible for the formation of a buried porous layer [7]. Ongo-

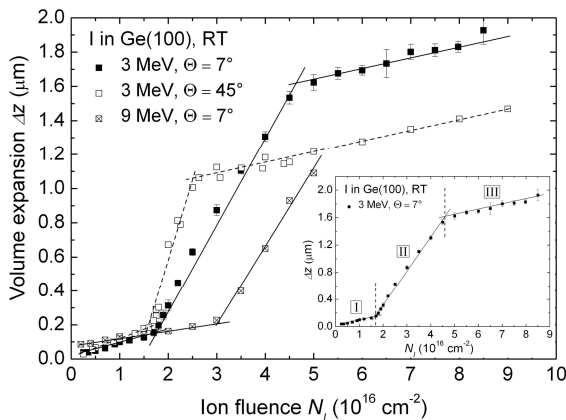


Fig. 1 Volume expansion  $\Delta z$  as a function of fluence  $N_i$  for irradiated germanium with 3 and 9 MeV I ions under an angle of  $\Theta = 7^\circ$  and  $45^\circ$ , respectively. The lines are linear approximations indicating three regions along the fluence axis [7].

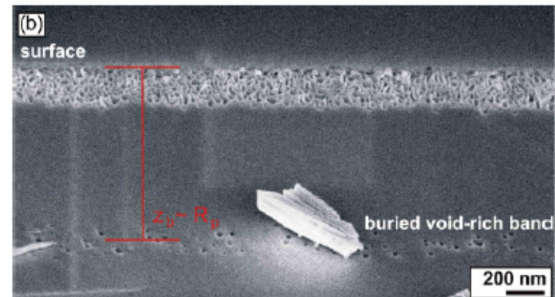


Fig. 2 Cs-SEM image showing the formation of a nanoporous structure at the surface and the formation of buried voids within the amorphous Ge layer for a sample irradiated with 3 MeV I ions under  $\Theta = 7^\circ$  and with a fluence  $N_i = 1.8 \times 10^{16} \text{ cm}^{-2}$

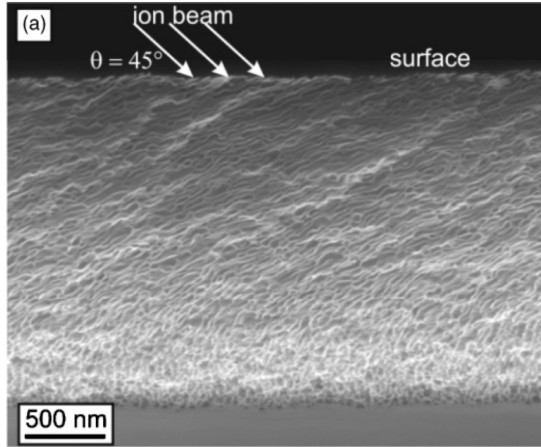


Fig. 3 For samples irradiated with 3 MeV I,  $\Theta = 45^\circ$ , and high ion fluences, a movement of the extended porous layer into the direction of the ion beam projection is visible in the cs-SEM [7].

ing irradiation results in the formation of a buried porous layer and broadening of both porous layers. At high fluences, surface and buried porous layer grow together which is demonstrated in Fig. 3. In contrast to perpendicular irradiations, the irradiation under  $45^\circ$  shows a tendency of alignment of the porous structure which may be due to movement of the layer into the direction of the ion beam projection onto the sample surface (cp. Fig. 3) [7].

All these effects are well reproducible and the analysis of the porous layer thickness  $d_p$  obtained for different irradiation conditions point up, that  $d_p$  is only a linear function of the normalized ion fluence [7]. This implies that the void formation is determined solely by the nuclear energy deposition. The whole mechanism which leads to the observed structural changes is discussed based on the approach of energetically favorable agglomeration of ion-induced vacancy like defects caused by the nuclear energy deposition. Based on this mechanism and the fact that buried voids are formed in the depth of the projected ion range, we conclude that chemical properties of the irradiated ions are responsible for the formation of buried porous layers [7].

In addition, for all nonperpendicular ion irradiations a nonsaturating irreversible plas-

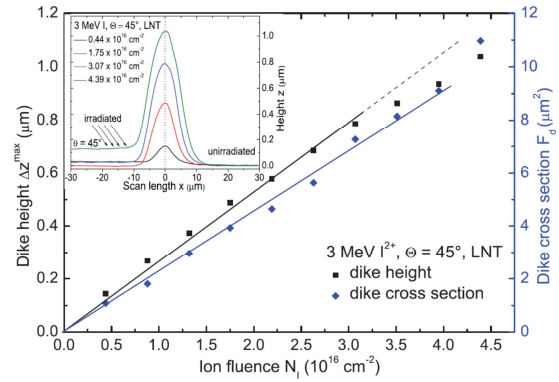


Fig. 4 Dike height  $\Delta z^{\max}$  and dike cross section  $F_d$  for Ge irradiated with 3 MeV I and under  $\Theta = 45^\circ$  as a function of ion fluence  $N_I$ . Data were fitted linearly. Additionally, the inset illustrates the dike formation for nonperpendicular ion irradiation of Ge as measured by the surface profilometer [7].

tic flow was observed (cp. Fig. 3). Profilometric measurements (cp. Fig. 4) reveal a dike formation at the boundary to the unirradiated material, which increases linearly with increasing ion fluence [7]. Such a dike formation was observed for SHI irradiations as a direct consequence of plastic deformation (hammering effect), i.e. lateral mass transport into the direction of the beam projection [8].

The research was supported by the Bundesministerium für Bildung und Forschung (Contract No. 05KK7SJ1) and Deutscher Akademischer Austausch Dienst (Contract No. D/07/15034).

## References

- [1] C.C. Jacobi, T. Steinbach and W. Wesch, Nucl. Instr. Meth. B 272, 326 (2012).
- [2] B. R. Appleton, O. W. Holland, J. Narayan, O. E. Schow, J. S. Williams, K. T. Short, and E. Lawson, Appl. Phys. Lett. 41, 711 (1982).
- [3] H. Föll, J. Carstensen, and S. Frey, J. Nanomat. 2006, 1 (2006).
- [4] D. Sun, A. Riley, A. Cadby, E. Richman, S. Korlann, and S. Tolbert, Nature 411, 1126 (2006).
- [5] T. Steinbach, C.S. Schnohr, P. Kluth, R. Giulian, L.L.Araujo, D.J.Sprouster, M.C.Ridgway, and W. Wesch, Phys. Rev. B 83, 054113 (2011).
- [6] K. Gärtner, J. Jöhrens, T. Steinbach, C.S. Schnohr, M.C. Ridgway, W. Wesch, Phys. Rev. B 83, 224106 (2011).
- [7] T. Steinbach, J. Wernecke, P. Kluth, M.C. Ridgway, and W. Wesch, Phys. Rev. B 84, 104108 (2011).
- [8] A. Gutzmann and S. Klaumünzer, Nucl. Instrum. Methods Phys. Res. Sect. B 127/128, 12 (1997).

# Void formation in a-Ge due to high electronic energy deposition

K. Gärtner, J. Jöhrens, T. Steinbach, C. S. Schnohr, M. C. Ridgway\*, and W. Wesch

\*Australian National University, Research School of Physics and Engineering, Canberra, Australia

Swift heavy ion irradiation of a-Ge causes the formation of voids and results in an intensive volume expansion  $\Delta z$ . Independent of the irradiation conditions the relative step height  $\Delta z/d$  ( $d$  refers to the amorphous layer thickness) depends linearly on the ion fluence  $N_I$  (cp. Fig. 1). However, the slope  $\alpha_{\text{EXP}} = (\Delta z/d)/N_I$  is a linear function of the electronic energy deposition  $\epsilon_e$  (cp. inset of Fig. 1) and the extrapolation of the regression line reveals the existence of a threshold value of about  $\epsilon_e^{\text{EXP}} = 10.5 \text{ keV nm}^{-1}$  above which the void formation in a-Ge begins [1]. To get a deeper insight into the mechanism of ion beam induced void formation in a-Ge the effect was investigated by means of molecular dynamics computer simulation [2]. The MD-simulations were done with a standard MD code. A given ion penetrates the MD cell in the  $z$ -direction at a stochastic position. All atoms in a so called deposition cylinder with a radius  $r_{\text{dep}}$  receive additional kinetic energy. The total amount of kinetic energy given in the region  $r < r_{\text{dep}}$  is

$\Delta E_{\text{kin}} = \epsilon_{\text{MD}} d$  with  $\epsilon_{\text{MD}} = g \epsilon_e$ , where  $\epsilon_{\text{MD}}$  is the part of  $\epsilon_e$  which is converted into atomic motion and  $d$  is the  $z$  extension of the initial MD cell. The ratio  $g < 1$  is unknown and used here as a free parameter.

In Fig. 2 representative snapshots of the MD-cell are shown for different times after energy deposition. It can be seen that the average mass densities  $\rho$  within the deposition cylinder (highlighted region in (a)) change dramatically. At about 1.5 ps,  $\rho$  is reduced to about 60% within  $r_{\text{dep}}$ , whereas  $\rho$  does not change remarkably for  $r > r_{\text{dep}}$ . A latent and stable void becomes more and more sharp with increasing time. As a consequence, the relative swelling in  $z$ -direction increases and reaches a constant value of about 7% at 50 ps [2].

Considering a sequence of ions (time interval between ion impacts: 100 ps) at different randomly chosen impact positions results in a sponge like structure as shown in Fig. 3. A sequence of ions leads to effects

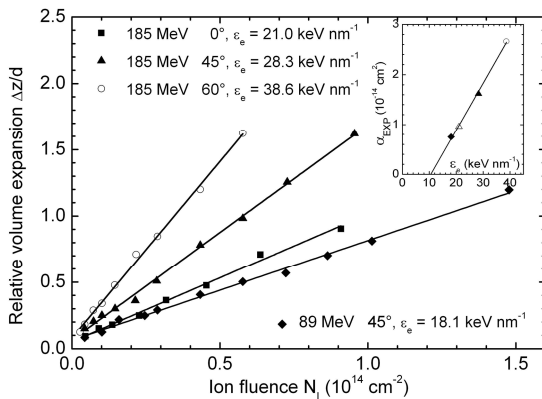


Fig. 1 The relative swelling  $\Delta z/d$  of an a-Ge layer due to the irradiation with Au ions as a function of the fluence  $N_I$ . The inset shows the slopes  $\alpha_{\text{EXP}}$  as a function of the electronic energy deposition  $\epsilon_e$ . The linear fits are given by the lines [1].

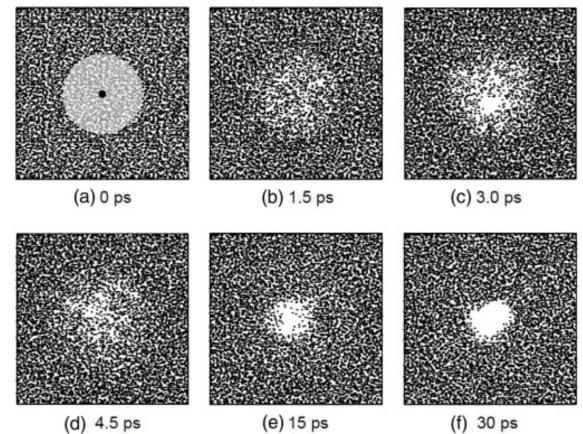


Fig. 2 The top views of the configurations of the atoms in the MD cell at different times after energy deposition. In (a), the impact position of the ion is marked by the full dot and all the atoms within the deposition cylinder ( $r_{\text{dep}} = 20 \text{ \AA}$ ) are highlighted [2].

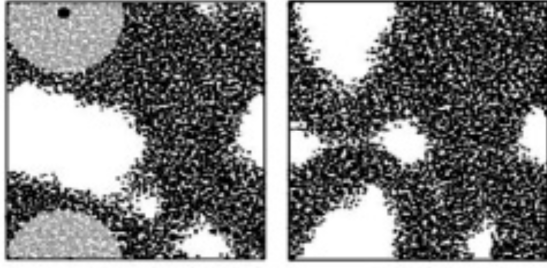


Fig. 3 The top views of the configurations of the atoms in the MD cell after 17 energy depositions [2].

like formation of new voids or the grow of a preexisting void as well as shrinking of voids. However, the processes of void formation or void growth dominate, so that a continuous volume expansion with an increasing amount of energy deposition is observed. For different values of  $\epsilon_{MD}$ , it is demonstrated that the relative volume expansion of the MD cell increases linearly with increasing ion fluence. Hence, the linear dependence of the volume expansion on the fluence is in good agreement with the experimental results [1]. In Fig. 4 the slopes  $\alpha_{MD}$  which were determined similar to the experimental value  $\alpha_{EXP}$  are depicted for different sizes of the MD cell as a function of  $\epsilon_{MD}$ . The slope of the swelling shows a linear dependence providing a threshold value which convergences with increasing size of the MD cell at  $\epsilon_{MD} = 2.2 \text{ keV nm}^{-1}$ . From this value and the experimentally determined value  $\epsilon_e^{EXP}$  follows  $g = 0.21$  for the relative part of  $\epsilon_e$  which is converted into atomic motion. The value thus obtained for  $g$  is of the same order of magnitude as mentioned in the literature [3].

Further investigation of the evolution of local densities and temperatures definitely show that acoustic waves are generated by high energy deposition. A determination of the wave front velocity (e.g. studying the evolution of the temperature wave front) reveals that the wave front moves with supersonic velocity at first and from about

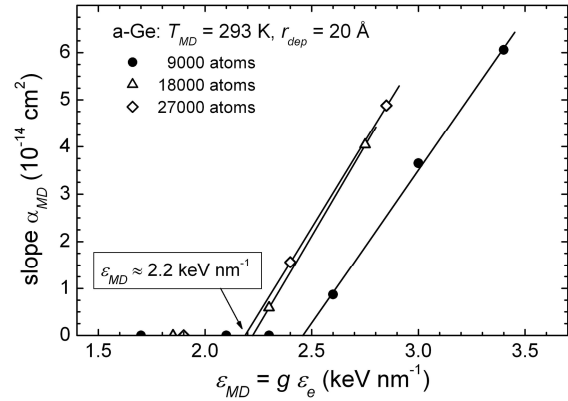


Fig. 4 The slopes of the swelling as a function of the energy loss  $\epsilon$  for different sizes of the MD-cell. The existence of a threshold value, which convergences with increasing cell size, is evident [2].

1.35 ps it propagates as an ordinary sound wave with exactly the measured sound velocity of a-Ge [4] which are both characteristic features of a shock wave [5]. Hence, our simulations clearly demonstrate for the first time that the experimentally proven void formation in SHI irradiated a-Ge can be explained by a shock wave mechanism as a result of the high electronic energy deposition [2].

The research was supported by the Bundesministerium für Bildung und Forschung (BMBF, Contract No. 05KK7SJ1) and Deutscher Akademischer Austausch Dienst (DAAD, Contract No. D/07/15034).

## References

- [1] T. Steinbach, C. S. Schnorr, P. Kluth, R. Giulian, L. L. Araujo, D. J. Sprouster, M. C. Ridgway, and W. Wesch, Phys. Rev. B 83, 054113 (2011).
- [2] K. Gärtner, J. Jöhrens, T. Steinbach, C. S. Schnorr, M. C. Ridgway, W. Wesch, Phys. Rev. B 83, 224106 (2011).
- [3] G. Szenes, Z. E. Horvath, B. Pecz, F. Paszti, and L. Toth, Phys. Rev. B 65, 045206 (2002).
- [4] I. Cox-Smith, H. Liang, and R. Dillon, J. Vac. Sci. Technol. A 3, 674 (1985).
- [5] G. Carter, Radiat. Eff. Lett. 43, 193 (1979).

# Composition-dependent atomic-scale structure of Cu(In,Ga)Se<sub>2</sub>

H. Kämmer, T. Steinbach, C. Stephan\*, S. Schorr\* and C. S. Schnohr

\*Helmholtz-Zentrum Berlin für Materialien und Energie, Hahn-Meitner-Platz 1, 14109 Berlin

Atomic-scale structural parameters often show a strong influence on important material properties. For CuInSe<sub>2</sub> and CuGaSe<sub>2</sub>, the band gap energy depends in a crucial way on the position of the Se anion within the unit cell [1]. Both compounds crystallize in the chalcopyrite type crystal structure (space group  $I\bar{4}2d$ ) which can be derived from the zincblende type crystal structure (space group  $F\bar{4}3m$ ) by populating the cation positions in an ordered manner with Cu and group-III atoms. This leads to a doubling of the unit cell in  $c$ -direction as shown schematically in Fig. 1. Other non-cubic features of the structure are a tetragonal distortion  $\eta=c/2a$  unequal to one, where  $a$  and  $c$  denote the lattice constants, and a displacement of the anion from the ideal lattice site due to the different properties of the neighbouring cations.

The mixed compound, Cu(In,Ga)Se<sub>2</sub>, also crystallizes in the chalcopyrite structure and the lattice constants vary linearly with composition between the values of the ternary compounds [2]. However, the group-III lattice positions are occupied randomly by In and Ga atoms leading to different first

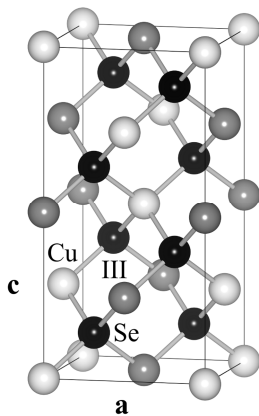


Fig. 1: Schematic showing the chalcopyrite type crystal structure of Cu(In,Ga)Se<sub>2</sub>.

nearest neighbour configurations around the Se anions. It is well known for other mixed compounds such as (In,Ga)P that the anion position depends sensitively on the first nearest neighbour environment [3]. Given the remarkable influence of the anion position on the band gap, the atomic-scale structure of Cu(In,Ga)Se<sub>2</sub> has thus been studied as a function of composition using extended x-ray absorption fine structure spectroscopy (EXAFS).

Cu(In,Ga)Se<sub>2</sub> powder samples with varying In/III = In/(In+Ga) ratio were synthesized by solid state reaction [4]. The elemental composition was determined using wavelength dispersive x-ray analysis. While the long-range crystallographic structure can be determined very precisely using x-ray or neutron diffraction, EXAFS provides information about the short-range environment of a particular atomic species. EXAFS measurements of the Cu, Ga and In K-edges corresponding to edge energies of 8.979, 10.367 and 27.940 keV, respectively, were performed in transmission mode at Beamline C of HASYLAB (DESY) in Hamburg. Spectra were recorded at a temperature of  $17 \pm 1$  K in order to minimize thermal vibrations of the atoms.

The data were processed and analysed using the IFEFFIT code [5] together with the user interfaces ATHENA and ARTEMIS [6]. After background subtraction and Fourier transformation over a photoelectron wave number range of  $k=3-15 \text{ \AA}^{-1}$ , the first nearest neighbour scattering contribution was fitted over a radial range of  $R=1.4-2.9 \text{ \AA}$  for the Cu and Ga K-edges and  $R=1.5-3.0 \text{ \AA}$  for the In K-edge using multiple  $k$ -weights of 2, 3 and 4. Phase shifts

and scattering amplitudes were calculated using FEFF9 [7] while the amplitude reduction factor  $S_0^2$  and the threshold energy  $E_0$  were fixed to average values determined from all samples. The mean value  $R$  and the standard deviation  $\sigma^2$  of the first nearest neighbour distance distribution were fitted whereas the coordination number was fixed to four. The element-specific bond lengths  $R_{Cu-Se}$ ,  $R_{Ga-Se}$  and  $R_{In-Se}$  thus obtained are plotted versus the In/III ratio in Fig. 2. The overall uncertainties amount to  $\pm 0.002 \text{ \AA}$ . The  $\sigma^2$  values (not shown) range from 2.5 to  $3.9 \times 10^{-3} \text{ \AA}^2$ , typical for low temperature measurements.

For  $\text{CuGaSe}_2$ ,  $R_{Ga-Se}$  and  $R_{Cu-Se}$  are almost identical corresponding to an anion position very close to the ideal lattice site in good agreement with neutron powder diffraction studies [4]. For  $\text{CuInSe}_2$ ,  $R_{In-Se}$  is much larger than  $R_{Cu-Se}$  corresponding to a significant displacement of the anion from the ideal lattice site again in good agreement with diffraction studies [4].

For the mixed  $\text{Cu(In,Ga)Se}_2$  compounds, the element-specific bond lengths measured with EXAFS remain close to their ternary values over the whole compositional range. This behaviour is very similar to that observed for other mixed compounds such as  $(\text{In,Ga})\text{P}$  and can be explained by the fact that bond bending is energetically favoured over bond stretching in these tetrahedrally coordinated systems [3]. The weighted average of the Ga-Se and In-Se bond lengths,  $R_{III-Se}$ , shows a linear increase with increasing In/III ratio again in perfect accord with neutron diffraction studies [3] which measure the *average* group-III-Se first nearest neighbour distance.

An earlier EXAFS study on  $\text{Cu(In,Ga)Se}_2$  by Antonioli *et al.* [8] found a somewhat different behaviour than that discussed above, however, the present study is deemed more precise as  $R_{In-Se}$  was deter-

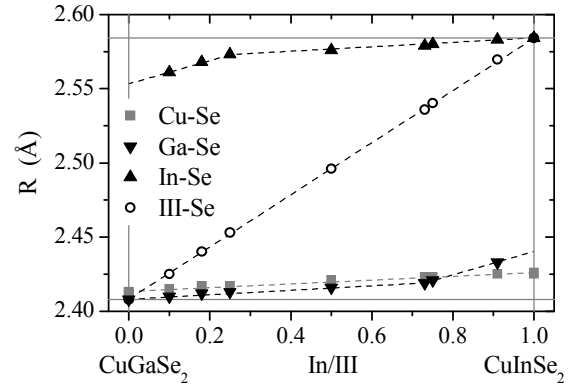


Fig. 2: Element-specific bond lengths  $R$  (mean value of the first nearest neighbour distance distribution) measured at the Cu, Ga and In K-edges at 17 K as a function of the  $\text{In/III} = \text{In}/(\text{In}+\text{Ga})$  ratio of  $\text{Cu(In,Ga)Se}_2$ .

mined directly from a measurement of the In K-edge at very low temperature and the uncertainty of all bond length values was properly evaluated.

Based on these element-specific bond lengths, the various first nearest neighbour configurations were modelled using a simple valence force field approach. The resulting anion position strongly depends on the nature of the surrounding atoms. This variation of the atomic-scale structure in mixed systems such as  $\text{Cu(In,Ga)Se}_2$  or  $(\text{In,Ga})\text{P}$  constitutes one origin of the nonlinear change in the band gap with composition also known as band gap bowing [9].

## References

- [1] S.-H. Wei *et al.*, Phys. Rev. B **58**, R1710 (1998).
- [2] M. R. Balboul *et al.*, Appl. Phys. A **92**, 557 (2008).
- [3] C. S. Schnohr *et al.*, Phys. Rev. B **78**, 115201 (2008).
- [4] C. Stephan, PhD thesis, Freie Universität Berlin/Helmholtz-Zentrum Berlin, Germany (2011).
- [5] M. Newville, J. Synchrotron Radiat. **8**, 322 (2001).
- [6] B. Ravel, M. Newville, J. Synchrotron Radiat. **12**, 537 (2005).
- [7] J. J. Rehr *et al.*, Phys. Chem. Chem. Phys. **12**, 5503 (2010).
- [8] G. Antonioli *et al.*, J. Physique **47**, 431 (1986).
- [9] S.-H. Wei, A. Zunger, J. Appl. Phys. **78**, 3846 (1995).

# Qualitative analysis of diamond like carbon layers

J. Sommerfeld, M. Wille, T. Dörfer\*, and C. Ronning

\* *Institute for Physical Chemistry, University of Jena*

Motivated by the idea to investigate the interaction of diamond like carbon (DLC) layers with medically relevant adsorbents such as human plasma fibrinogen (HPF), we aimed for DLC substrates with varied properties. The key property of DLC is the  $sp^3$  content of the carbon bonding, which determines the “diamond likeness” of the sample.

The DLC layers were synthesized via mass separated ion beam deposition (MSIBD), which is described in detail in the annual report 2008, page 80-81. This setup allows a controlled variation of the acceleration that is applied to the used carbon ion beam. Since the  $sp^3$  content of the DLC layers strongly depends of the carbon ion energies [1], a determination of the actual ion energy was necessary. The referring determination is possible by guiding the ion beam through an additional electric field where the ions are deflected depending on their energy [2]. Therefore, we mounted a cylindrical capacitor with tunable voltage (ESA) into the deposition chamber. The ion beam was guided into the deposition chamber as usual and eventually entered the capacitor. The capacitor is designed in the way that the required voltage for the ions to pass is directly proportional to twice the ion energy ( $U_{\text{cond}} = 2 \cdot E_{\text{ion}}$ ). Figure 1 presents the dependency of the ion current at the sample on the capacitor voltage for a variety of ion acceleration voltages (250, 500, 750, 1000 V).

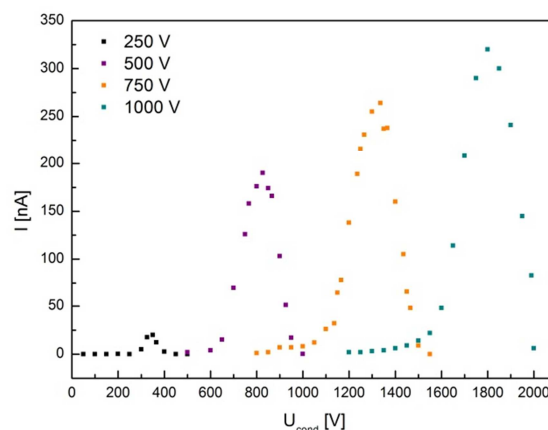


Fig. 1: Current of the carbon ion beam with different acceleration voltages that was guided through a capacitor with varied electrical fields.

We found the linear correlation that is shown in figure 2 by examining each peak in figure 1 linked to the respective capacitor voltage with the ion energy. By applying a linear fit, it was possible to determine the energy the ions had when they left the source, respectively before they entered the acceleration unit.

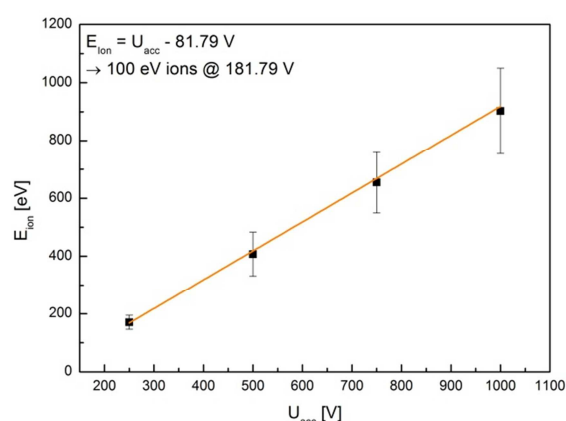


Fig. 2: Carbon ion energy dependency on the applied acceleration. Due to the fit, the ions have an initial energy of 82 eV when they are extracted.

Consequently, the offset of the initial energy of the carbon ions is  $82 \pm 10$  eV. These measurements were also done for

different source parameters (not shown here), but no significant influence was found. In general, the highest  $sp^3$  content can be achieved with ion energies around 100 eV. Consequently, a voltage of 182 eV has to be applied in order to obtain a maximum  $sp^3$  content of about 80%.

We performed UV (244 nm) Raman measurements on synthesized carbon thin films using the ion energies described above. Whereas VIS Raman spectroscopy only excites the  $sp^2$  vibrations at  $1580\text{ cm}^{-1}$  (G mode) and  $1400\text{ cm}^{-1}$  (D mode), UV Raman also interacts with the  $sp^3$  phase of the layer at  $1100\text{ cm}^{-1}$  (T mode). Though literature [3,4,5], is quite contradicting concerning the evaluation of the obtained results, we made use of fitting the Breit-Wigner-Fano (BWF) function describing the spectral intensity as

$$I(\omega) = \frac{I_0 [1 + \frac{2(\omega - \omega_0)^2}{q\Gamma}]^2}{1 + [\frac{2(\omega - \omega_0)}{\Gamma}]^2} + a \cdot \omega + b \quad (1).$$

Hereby,  $I_0$  is the maximum intensity,  $\Gamma$  is the FWHM,  $q$  is the skewness factor, and the factors  $a$  and  $b$  describe the background. As it can be seen in figure 3a, the Raman spectra differ slightly for DLC layers that were produced using varied carbon ion energies. Since the T peak is hardly to be seen due to an overlap with a substrate (Si) related peak at  $1050\text{ cm}^{-1}$ , we mostly focused on the evaluation of the BWF fit in the range of the D and G peak. The obtained skewness factor  $q$  is plotted in figure 3b. According to Gilkes et al. [3], a  $q$  value of -12 for ion energies of about 500 eV can be related to a  $sp^3$  content of 70–90%. For ion energies 100 and 1000 eV, we found lower  $q$  values of -6.5 to -8.5, respectively, that correlate with an  $sp^3$  content of 60-80%. Only for very low ion energies (40 and 60 eV), the  $q$  factor increased to almost -4, which indicates a  $sp^3$  content of less than 50%.

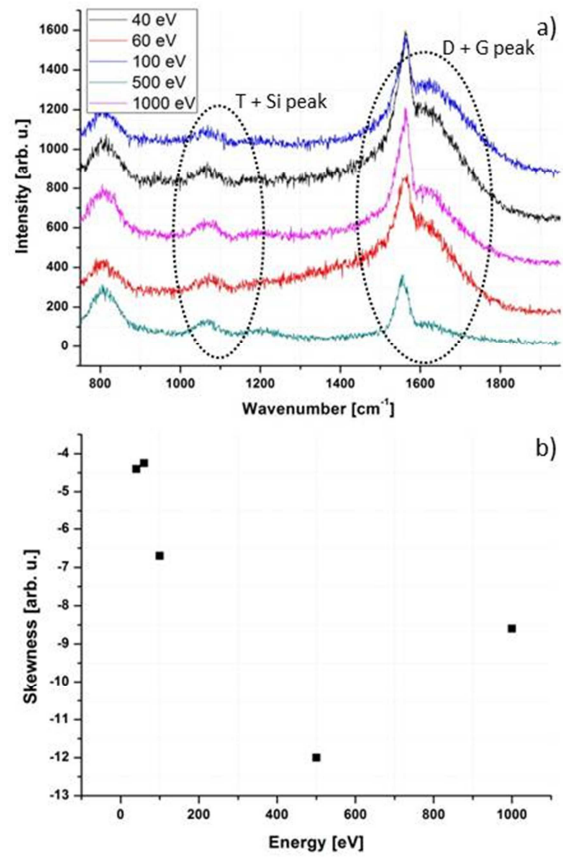


**Fig. 3:** a) UV Raman (244 nm) spectra of DLC layers that were prepared with different ion energies. b) Skewness factor of the BWF fit in the range of  $1300 - 1700\text{ cm}^{-1}$  for the different layers. Minimum Skewness factor was achieved for DLC layers.

In summary, we were able to determine the initial energy of carbon ions that are used to synthesize DLC layers via MSIBD. By tuning the energy of the carbon ions, the  $sp^3$  content can be varied and thus one of the key properties of DLC.

## References

- [1] C. Ronning. *Applied Physics A* **77**, 39 (2003).
- [2] H. Stillrich, Diplomarbeit, Georg-August-Universität zu Göttingen, 2003.
- [3] K. W. R. Gilkes et al., *Journal of Applied Physics* **87**, 7283 (2000).
- [4] A. C. Ferrari et al., *Physical Review B* **62**, 11089 (2000).
- [5] S. Praver et al., *Diamond and Related Materials* **5**, 433 (1996).



# Persistent Ion Beam Induced Conductivity in Zinc Oxide

A. Johannes, R. Niepelt, M. Gnauck, and C. Ronning

Metal oxides in general and ZnO thin films in particular have already shown a good ultra-violet (UV) [1] and gas-sensing [2] ability due to the instability of oxygen at the surface [3-5]. As the surface influence is increased in nanowires, greatly enhanced sensitivity is expected from nanowire devices [6]. Although the conductivity of ZnO can easily be increased by three orders of magnitude by UV excitation, the current only returns to the relaxed value very slowly due to the known Persistent Photo Conduction (PPC) effect [6].

In this work, we report that an analogue Persistent Ion beam induced Conduction (PIC) arises during ion irradiation [7]. PIC may allow single ion detection in individual ZnO nanowires, as well as countable doping with single dopants into ZnO nanowires. The strongly localized energy deposition of a single ion impact can result in a change in the properties of the entire device, providing a localized probe to understand the underlying excitation mechanisms.

The typical lifetime of charge carriers in ZnO nanostructures is in the order of 100 ps. To contribute to a persistent current increase, excited charge carriers have to populate distinct, stable states. According to Prades et al. [4] these are surface-oxygen bound states. For PIC discussed in this work, ions instead of UV photons generate electron hole pairs in the semiconductor.

Figure 1 shows the typical, strongly asymmetrical I-V characteristics and a SEM image of such a single nanowire device, as manufactured. The asymmetry, caused by high Schottky barriers forming between the

intrinsic ZnO and the Ti/Au contacts, is often only exposed when measuring the characteristics across a sufficiently large voltage range, at least larger than the 3,4 V corresponding to the band gap of ZnO.

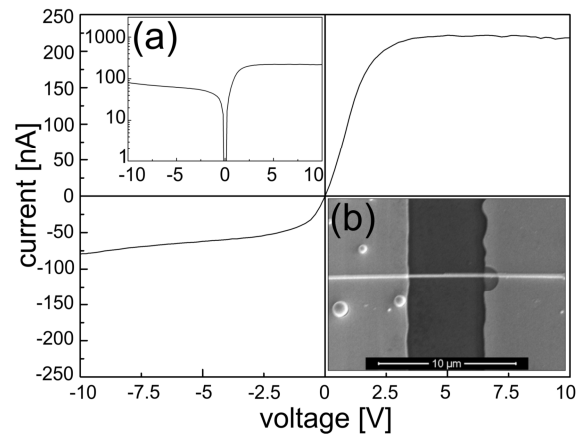


**Fig. 1:**  $I$ - $V$  response of a typical device investigated [in inset (a) as a logarithmic plot]. The device characteristics are dominated by the Schottky contacts formed between each end of the ZnO nanowire and the Ti/Au contact pads. Inset (b) shows an SEM image of a ZnO nanowire device investigated.

Figure 2 shows the current through a ZnO nanowire device during implantation, this time at a minimal ion current of  $\sim 5 \text{ pAcm}^{-2}$  terbium ions. This corresponds to an estimated one impingement per three seconds exposure. A fully relaxed device with low initial conductivity of  $\sim 0,5 \text{ nA}$  increases its conductivity to  $6 \text{ nA}$  in distinct steps during  $\sim 350 \text{ s}$  of exposure. Terbium was used for this implantation to show that the PIC effect is not at all ion specific and because rare earths show interesting optical properties in ZnO.

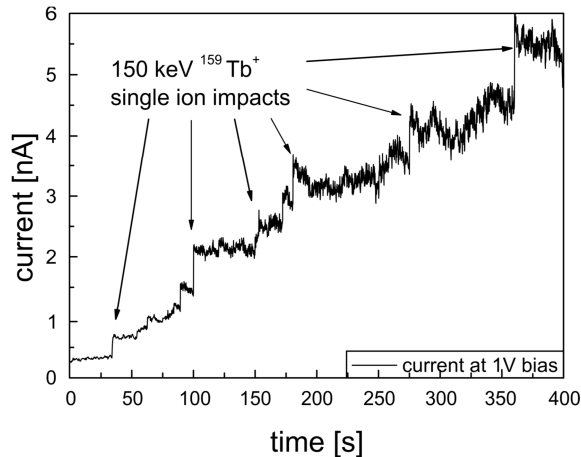


Fig. 2: Current through a nanowire device at 1V during strongly attenuated ion beam exposure (ion current  $5 \text{ pA/cm}^2$ ). The single incidences of increasing conductivity indicate sufficient sensitivity of relaxed devices to detect single ions.

Each impinging ion has 150 keV of energy. The absolute maximum number of charge carriers which can be generated with this energy is  $2 \times 150 \text{ keV} / 3.4 \text{ eV} \sim 90\,000$  ( $2 \times \text{ion energy} / \text{band gap}$ ). Note that this is a gross overestimation of the charge carriers. We find, that an ion current of  $5 \text{ pAcm}^{-2}$  thus generates a maximum charge carrier density of  $2 \times 10^7 \text{ cm}^{-3}$ , assuming a lifetime of 100 ps. With a mobility of  $20 \text{ Vscm}^{-2}$  [5] and a bias of 1V across the nanowire length of  $5 \text{ }\mu\text{m}$  this amounts to a directly ion induced current of less than 1 fA, far less than the observed current change. Although it was already clear, that the charge carriers generated by ion excitation do not have a sufficient life time to contribute directly to persistent conductivity changes, this estimation shows the exaggerated current excitation efficiency of PIC in ZnO. Similar results have been published for the PPC effect (see for eg. [5]).

It was estimated that about 30-40 ions would impinge the exposed nanowire, however only 9 distinct events could be detected. This may be attributed to some ions merely glancing off the nanowires. Also, the devices'  $I$ - $V$  characteristics are domina-

ted by Schottky barriers, so that any changes in these areas will have the greatest effects. It is plausible, that the area near the metal contacts, where the Schottky barriers are formed, responds more sensitively to excitation. Ions impinging the center of the nanowire device would then be largely without effect.

In conclusion, PIC has been shown to exist as an effect in ZnO closely related to PPC. Excitation efficiency, decay rates and chemical sensitivity of both effects match. The PIC effect is predicted to also occur in all other materials that exhibit PPC, as the energy brought into the material by ions can activate metastable states similarly to photons. PIC can thus help to expand the understanding of other materials' response to external excitation. PIC can potentially lead to countable implantation in ZnO and other materials showing PPC. ZnO nanowires provide a large set of parameters of which some are difficult to even control qualitatively. However, the pronounced sensitivity of ZnO nanowire devices shown and exploited in this work will surely lead to superior sensing applications.

## References

- [1] N. W. Emanetoglu, J. Zhu, Y. Chen, J. Zhong, Y. Chen, and Y. Lu, *Appl. Phys. Lett.* **85**, 3702 (2004).
- [2] G. Sberveglieri, *Sens. Actuators B* **23**, 103 (1995).
- [3] Y. Li, F. Della Valle, M. Simonnet, I. Yamada, and J.-J. Delaunay, *Appl. Phys. Lett.* **94**, 023110 (2009).
- [4] J. D. Prades, F. Hernandez-Ramirez, R. Jimenez-Diaz, M. Manzanares, T. Andreu, A. Cirera, A. Romano Rodriguez, and J. R. Morante, *Nanotechnology* **19**, 465501 (2008).
- [5] J. Bao, I. Shalish, Z. Su, R. Gurwitz, F. Capasso, X. Wang, and Z. Ren, *Nanoscale Res. Lett.* **6**, 404 (2011).
- [6] G. Shen, P.-C. Chen, K. Ryu, and C. Zhou, *J. Mater. Chem.* **19**, 828 (2009).
- [7] A. Johannes, R. Niepelt, M. Gnauck, C. Ronning *Appl. Phys. Lett.* **99**, 252105 (2011).

# Highly Mn doped GaAs nanowires by ion implantation

C. Borschel, M.E. Messing<sup>1</sup>, K. Mergenthaler<sup>1</sup>, M.T. Borgström<sup>1</sup>, W. Paschoal Jr.<sup>1</sup>, J. Walentin<sup>1</sup>, S. Kumar<sup>1</sup>, K. Deppert<sup>1</sup>, C.M. Canali<sup>2</sup>, H. Pettersson<sup>1,3</sup>, L. Samuelson<sup>1</sup>, C. Ronning

1) Solid State Physics/The Nanometer Structure Consortium, Lund University, Sweden

2) Division of Physics, School of Comp. Science, Physics and Math., Linnæus University, Kalmar, Sweden

3) Dept. of Mathematics, Physics and Electrical Engineering, Halmstad University, Sweden

Current electronics uses only the charge of the electron for information processing. Enhanced functionality might be achieved by making use of the electron spin as well. *Dilute magnetic semiconductors* (DMS) are of high interest to combine conventional semiconductor electronics with spintronic functionality. One prominent DMS material is highly Mn doped GaAs, where substitutional Mn on Ga sites provides not only the magnetic moments from its unpaired 3d electrons but also acts as an acceptor, providing the charge carriers to couple the magnetic moments.  $\text{Ga}_{1-x}\text{Mn}_x\text{As}$  thin films exhibit ferromagnetism with  $x$  in the order of a few percent [1]. Creating DMS nanowires (NW) opens the door to including spintronic functionality in the wide range of NW based devices. However, the low solubility of transition metals in III-V semiconductors caused all attempts to grow highly Mn doped single crystalline GaAs NW to suffer from strong MnAs segregation [2]. In order to circumvent this problem, we used ion implantation under enhanced dynamic annealing conditions for the incorporation of Mn into undoped GaAs nanowires [3]. Solubility limits are easily overcome, since the ion energies used in implantation are far beyond thermal energies.

GaAs nanowires with diameters in the range from 40-60 nm were grown via MOVPE, details in reference [4]. Mn ions were implanted with energies in the range from 40 to 60 keV. Computer simulations of the implantation process were performed using the new in-house developed computer

code *iradina* [5], in order to obtain the distribution of implanted Mn ions in the NWs.

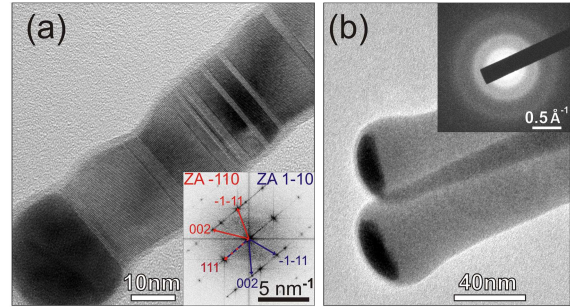
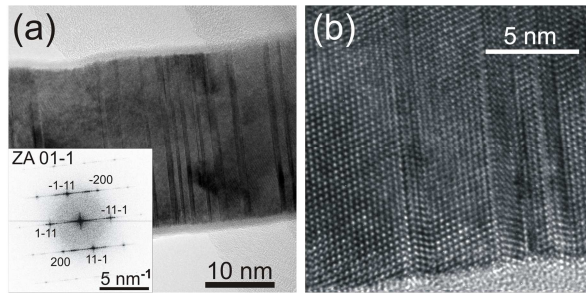


Fig. 1: (a) TEM image of as-grown highly crystalline nanowire with twins. Inset shows FFT. (b) Nanowires implanted with  $1 \cdot 10^{16}$  Mn ions/cm<sup>2</sup> at 40 keV. The electron diffraction pattern shows amorphous rings.

When implanting Mn at room temperature the nanowires became mostly amorphized, because of the introduced ion beam damage, see TEM images in Figure 1. Subsequent annealing in vacuum lead to polycrystalline NWs or to the decomposition of the NWs due to loss of arsenic. Thus, it was tried to anneal them in arsine atmosphere in a second set of experiments, as was reported successful for Zn doped GaAs NW [6]. However, the Mn doped GaAs NW always became polycrystalline or still decomposed during annealing in arsine.

A fraction of the ion beam induced point defects already anneals out during implantation due to the energy deposited by the ions. This so called *dynamic annealing* is enhanced in nanowires due to the reduced dimensionality and respective slower dissipation of heat. In order to preserve the crystalline structure of the NWs while implanting, we further increased the dynamic annealing by heating the samples to higher base temperatures during the implantation

process. Indeed, the GaAs nanowires remain crystalline, when implanting Mn at temperatures above 150 °C. Excellent crystallinity was achieved at 250 °C as illustrated in Figure 2. The twins are observed like in the non-implanted nanowires, showing that the crystal structure is preserved during implantation.



**Fig 2:** TEM images of GaAs NW implanted with  $1 \cdot 10^{16}$  Mn ions/cm<sup>2</sup> with 50 keV at 250°C. (a) Nanowire with FFT as inset, (b) HR-TEM image showing crystallinity and original twin structure.

The concentration of implanted Mn atoms in the GaAs nanowires was determined to  $x \approx 0.04$ – $0.06$  using energy dispersive X-ray spectroscopy (EDX), proving that the Mn does not diffuse out of the NW at the high implantation temperatures. Furthermore, the determined concentration is in good agreement with the simulation results from *iradina*.

The highly Mn doped nanowires were mechanically transferred to insulating substrates in order to investigate the transport properties. Pd/Zn/Pd contacts were defined on the nanowires using electron beam lithography. The conductivity of the Mn doped nanowires is increased by about 5 orders of magnitude compared to undoped NWs due to the Mn acceptor states. However, the estimated hole concentration of about  $10^{17}/\text{cm}^3$  is still much lower than expected from the Mn doping concentration. Probably, the acceptors are partly compensated by donors and defects (Mn interstitials and  $\text{As}_{\text{Ga}}$  antisites generated by the ion implantation).

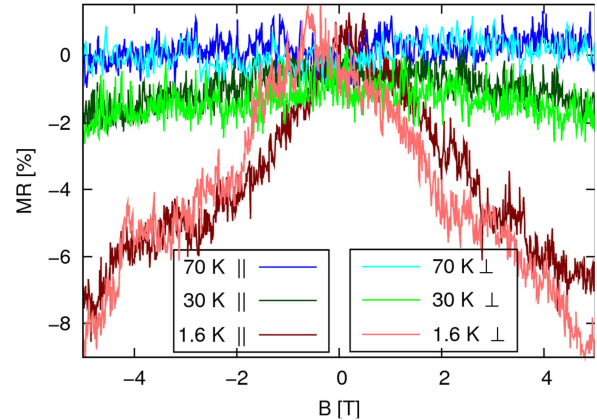


**Fig 3:** Magnetoresistance of a contacted nanowire measured at different temperatures with the magnetic field parallel (||) and perpendicular (⊥) to the nanowire axis.

The nanowires exhibit a negative magnetoresistance (MR) at temperatures below 50 K, see Figure 3. The negative MR may be caused by a reduction of spin disorder scattering and the suppression of Anderson localization of holes. The lack of any hysteresis effects, saturation and any anisotropy point to a paramagnetic rather than ferromagnetic state of the nanowires. Apparently, the low hole concentration is not sufficient to couple the Mn spins. Increasing the carrier concentration will be targeted by future experiments.

To conclude, we have achieved highly Mn doped, highly crystalline GaAs nanowires via ion implantation at elevated temperatures. The nanowires are paramagnetic probably due to the insufficient hole concentration. Nevertheless, ion beam implantation with dynamic annealing is shown to be a promising method for transition metal doping of III-V semiconductor nanostructures.

## References

- [1] H. Ohno *et al.*, Appl. Phys. Lett. **363**, 69 (1996)
- [2] A. Rudolph *et al.*, Nano Letters **9**, 3860 (2009)
- [3] C. Borschel *et al.*, Nano Letters **11**, 3935 (2011)
- [4] A. Mikkelsen, et al., Nat. Mater. **3**, 519 (2004)
- [5] C. Borschel and C. Ronning, Nucl. Instr. Meth. B, **269**, 2133 (2011), see also [www.iradina.de](http://www.iradina.de)
- [6] D. Stichtenoth *et al.*, Appl. Phys. Lett. **92**, 163107 (2008)

# Determination of GaAs nanowire minority carrier diffusion lengths via EBIC from axial pn-junctions

R. Niepelt, C. Gutsche\*, M. Gnauck, A. Lysov\*, W. Prost\*, F.-J. Tegude\*, and C. Ronning

\*Solid State Electronics Department and CeNIDE, University of Duisburg-Essen  
Lotharstr. 55, 47048 Duisburg, Germany

The minority carrier diffusion lengths of electrons and holes in GaAs nanowires were determined in axial pn-junctions using electron beam induced current (EBIC) measurements. The carrier dynamics can be studied directly at the core element of nanowire solar cells and light emitting diodes: the pn-junction. Carrier diffusion lengths, which can be extracted from the exponential decay of the generated current on both sides of the junction, are orders of magnitude lower compared to bulk material due to surface recombination. Estimating the surface recombination velocities from the diameter-dependence of the diffusion length indicates a non-abrupt pn-junction in essential agreement with the actual model of dopant incorporation during the Au-assisted vapor-liquid-solid nanowire growth mechanism.

GaAs nanowire pn-junctions were synthesized via molecular organic vapour phase epitaxy (MOVPE) with Diethylzinc (DEZn) and Tetraethyltin (TESn) serving as dopant

precursors for the p and n-type part, resulting in a respective carrier concentration of  $N_A = 1.6 \cdot 10^{19} \text{ cm}^{-3}$  and  $N_D = 1 \cdot 10^{18} \text{ cm}^{-3}$  [1]. The determination of minority carrier diffusion lengths via spatially resolved EBIC or photocurrent measurements was shown for Si nanowire Schottky junctions [2,3]. However, diffusion length measurements directly on an axial pn-junction have not been conducted so far.

The geometry investigated in this study is sketched in Figure 1 a. As it is shown in Figure 1 b, only minority carriers contribute to the induced current when reaching the junction region. The EBIC signal along the nanowire decays via

$$I = I_0 \cdot e^{-\frac{x}{L_i}} \quad (1)$$

where  $I_0$  is the maximal intensity,  $x$  is the distance from the junction and  $L_{D,i}$  is the minority carrier diffusion length for electrons and holes following

$$L_{D,i} = \sqrt{D_i \cdot \tau_i} \quad (2)$$

with  $D_i$  and  $\tau_i$  as the respective diffusion

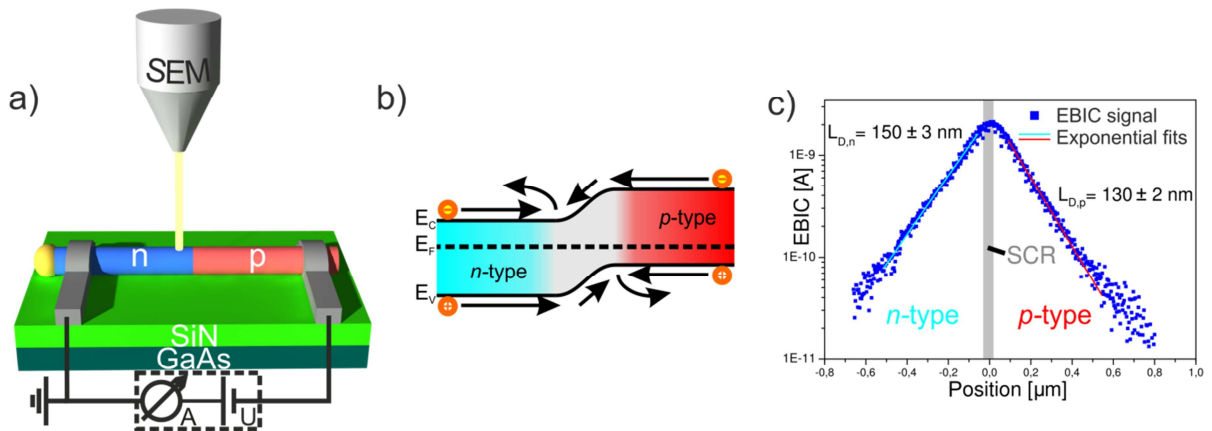


Fig. 1: a) EBIC measurement setup scheme using single axial nanowire pn-junctions. b) Schematic band diagram of the respective pn-diode. During the measurement, both majority and minority carriers can diffuse to the junction. Only the respective minority carriers are collected, whereas the majority carriers of both sides are repulsed. c) EBIC signal along the wire axis. The minority carrier diffusion lengths of both, electrons and holes, are extracted by analyzing the exponential decay of the current signal.

coefficient and carrier recombination lifetime. Scanning a nanowire with an axial pn-junction allows to extract both electron and hole diffusion lengths on the respective p- and n-type side of the junction simultaneously, as shown in Figure 1 c.

It is important that the device is investigated under low injection conditions (LIC) [4]. Otherwise, one might measure an ambipolar diffusion length of both minority and majority carriers. With the typical electron current (40 pA) and acceleration voltage (10 keV) used, LIC are assured.

The dependence between the measured minority carrier diffusion length and the nanowire diameter allows extracting the surface recombination velocities (SRV)  $S_i$ . From the measurements of  $L_i$  an effective carrier lifetime  $\tau_i^*$  can be obtained, connected with  $S_i$  and the bulk lifetime  $\tau_B$  via

$$\frac{1}{\tau_i^*} = \frac{1}{\tau_B} + \frac{4 \cdot S_i}{d} \quad (3)$$

where  $d$  denotes the nanowire diameter [2]. EBIC measurements were carried out on 4 different nanowire pn-diodes with diameters ranging from approximately 100 nm to 300 nm. Identical I-V characteristics have been recorded before and after the measurements to exclude any damage effects caused by the electron beam. The minority carrier diffusion lengths of both, electrons and holes, are plotted in Figure 2 and are monotonically increasing the nanowire diameter. The diffusion lengths are significantly small and about 10-fold lower compared to minority carrier diffusion lengths of bulk GaAs [5,6]. The expected diffusion length trends for distinct values of  $S$  are also plotted in Figure 2. The curves have been fitted by adjusting  $S$ . The resulting SRV ( $S_p = 4 \cdot 10^6 \text{ cm/s}$ ,  $S_n = 3 \cdot 10^5 \text{ cm/s}$ ) are comparable to values measured in GaAs bulk samples [7,8]. While  $S$  is almost identical to the bulk value for the p-type side of

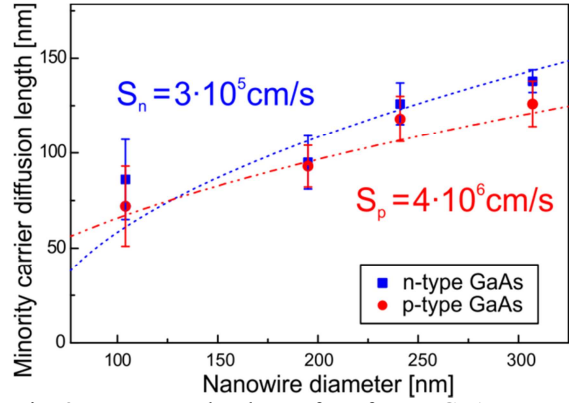


Fig. 2: Measured values of  $L_D$  for pn-GaAs nanowires as a function of diameter. The dashed lines are showing the theoretical progression of the diameter dependence for the stated surface recombination velocities. For the calculation depletion layers with 29.6 nm (n-type) and 6.8 nm (p-type) width were taken in account.

the nanowire, it is one order of magnitude smaller than expected for the estimated carrier concentration on the n-type side. Thus, it is likely that the doping level in the n-type part near the junction is lower than expected, caused by the synthesis method. When the dopant source is switched from p to n rapidly during growth, it still takes some time to reach a high doping level in the catalyst and therefore the n-doped nanowire part, which finally leads to an axially graded dopant profile.

## References

- [1] Regolin I, Gutsche C, Lysov A, Blekker K, Li Z-A, Spasova M, Prost W and Tegude F-J *J.Cryst. Growth* **315**, 143 (2011)
- [2] Dan Y, Seo K, Takei K, Meza J H, Javey A and Crozier K B *Nano Lett.* **11**, 2527 (2011)
- [3] Allen J E, Hermesath E R, Perea D E, Lensch-Falk J L, Li Z Y, Yin F, Gass M H, Wang P, Bleloch A L, Palmer R E and Lauhon L J *Nature Nanotechnology* **3**, 168 (2008)
- [4] Cavalcoli D and Cavallini A *Mater. Sci. Eng., B* **24**, 98 (1994)
- [5] Klein C A *J. Appl. Phys.* **39**, 4 (1968)
- [6] Wright D R, Oliver P E, Prentice T and Steward V W *J.Cryst. Growth* **55**, 183 (1981)
- [7] Ito H and Ishibashi T *Jpn. J. Appl. Phys.* **33**, 88 (1994)
- [8] Jastrzebski L, Lagowski J and Gatos H C *Appl. Phys. Lett.* **27**, 537 (1975)

# DNA modification of zinc oxide nanowires for sensing application

I. Slowik, B. Seise\*, C. Leiterer\*, R. Niepelt\*, W. Fritzsche\*, and C. Ronning\*

\*Institut für PhotonischTechnologien e.V., Jena , A.-Einstein-Str. 9, 07745 Jena

Here, we present a promising alternative approach to conventional fluorescence labeled DNA sensors [1]. Bottom up fabricated ZnO nanowires (ZnONW) were chemically modified to attach probe DNA on the surface of the nanowire. Successful binding and hybridization with the complementary DNA was shown using fluorescence labeled target DNA. Due to the quasi-one-dimensional geometry of the nanowires and the large surface-to-volume ratio, surface-induced effects can have a major impact on the electrical transport properties. Changes in surface composition lead to significant changes in nanowire conductivity. The effect can be utilized to create an electrical device out of biofunctionalized nanowires for specific sensing of biomolecules with high sensitivity.

The ZnONW samples were synthesized via vapor-liquid-solid (VLS) process at 1350°C and 100 mbar for ~ 30 min, which provides good crystal properties due to the high growth temperature. The ZnONW evolve in a typical spaghetti-like structure with wire diameters around 100 nm and wire lengths up to some tens of µm. In order to be able to perform a silanization reaction on the NW surface the samples were chemically activated using oxygen plasma etching at a pressure of 1,6 mbar and 380 W for at least 30 min. The silanization of the NW surface was performed at 70 °C for 3 h using glycidoxypropyltrimethoxysilane (GOPS) in water-free toluene. Afterwards the samples were washed several times in pure toluene and dried with compressed air. For the immobilization of the capture DNA to the NW surface silanized with GOPS, amino-modified oligonucleotides

are used. The amino-group is located on the 5'-terminus of the oligonucleotides and forms a stable attachment of the capture DNA to the surface. The terminal amino-modified oligonucleotides are applied with a concentration of 10 µM in 5 x PBS (pH 7.4) and dropped on the NW until desiccation. Subsequently the NWs were washed afterwards in 15 mM tris-HCl (pH 8.0) and dried using compressed air. In order to proof the ability of the NW to act as a substrate for the sequence specific detection of DNA, a DNA hybridization reaction was performed at room temperature in 5 x PBS for at least 2 hrs. Several control samples have been prepared with fluorescence labeled DNA in order to investigate the character and stability of attachment between DNA and ZnONW.

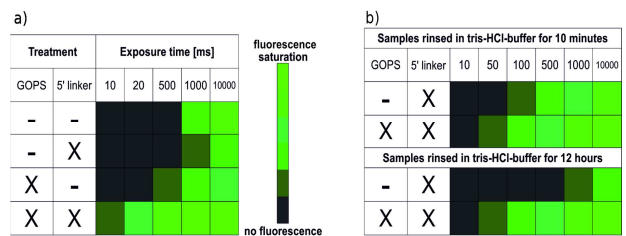


Fig. 1: In (a) a comparison of a sample with GOPS and a sample without GOPS rinsed in tris-HCl-buffer solution for different periods of time is presented. In (b) the fluorescence intensities of various control samples are compared in the same way.

The fluorescence intensities of various control samples are compared in Figure 1(a). In order to quantify the intensities of different fluorescent samples, all signals have been integrated for different lengths of time and the resulting apparent magnitudes have been classified into six levels of fluorescence intensity between no fluorescence at all and fluorescence saturation. It

obvious from figure 1 that the fluorescence is most pronounced in the case of GOPS treatment and DNA with amino linker. All the other control samples show significant less fluorescence, indicating that the strongest binding of the DNA to the nanowire is only achieved with both coupling groups present (epoxy group at GOPS and amino group at DNA) in order to form a covalent binding.

A comparison of a sample with GOPS and a sample without GOPS is presented in Figure 1(b). Both samples were biofunctionalized with DNA and amino linker. The samples have been rinsed in Tris-HCl buffer solution for 10 min and then measured. As expected, the silanized sample is showing the stronger fluorescence. However, after rinsing both samples for another 12 h, the fluorescence of the sample silanized with GOPS and then functionalized has not dropped; whereas, the fluorescence of the control sample is less present than before. This also indicates a comparatively stable, presumably covalent bond between the DNA and nanowire.

Furthermore, we show the successful detection of a complementary target DNA on the surface of single ZnONW [2]. The capture DNA was immobilized as described in the experimental section. Complementary capture DNA is immobilized onto the NW. The Cy3-labelled target DNA is used in the following hybridization reaction to proof the successful binding. Also non-complementary capture DNA is immobilized onto the NW. The Cy3-labelled target DNA is used in the subsequent hybridization reaction to proof absence of significant non specific binding as an important feature for future application. In fig. 2 ZnONW with the non-complementary capture DNA show no detectable fluorescence, whilst NW with complementary capture DNA show a bright fluorescence signal comparable with the signal of the Cy3-labeled capture DNA. Therefore, a

highly efficient hybridization to the modified NW was achieved. With these results the sequence specific DNA recognition and the efficient DNA hybridization on ZnONW is demonstrated.

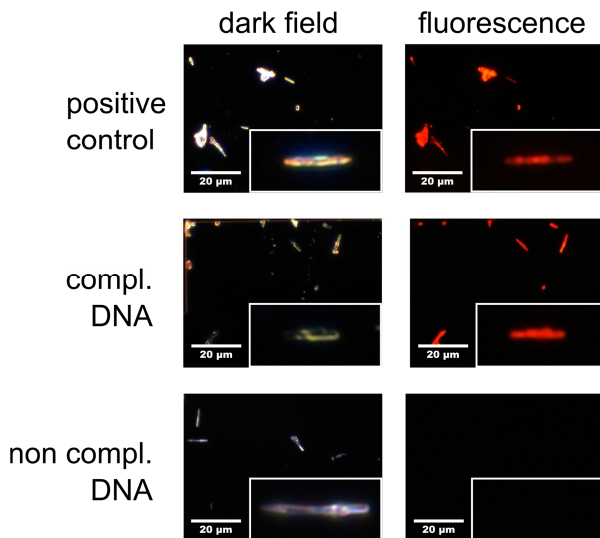


**Fig. 2:** Dark field and fluorescence measurements of ZnONW modified with DNA are compared to show that the immobilization and hybridization of DNA occurs on the NW. Insets are showing single ZnONW. A strong fluorescence signal for the positive control and the complementary target DNA is visible. Non-complementary target DNA shows no signal.

It was shown that amino-modified DNA could be immobilized onto ZnONW using standard silane chemistry. Moreover, it could be demonstrated that the DNA immobilized on ZnONW serve as basis for following DNA hybridization experiments. The successful detection of complementary DNA was presented, while non-complementary DNA shows no detectable signal. With these results we showed the applicability of ZnONW, for the development of label free DNA detectors.

## References

- [1] R. Niepelt et al., *Nanoscale Research Letters* **6**, 511 (2011)
- [2] C. Leiterer et al., *Journal of Biophotonics* (submitted)



# Nano-X-ray absorption spectroscopy of single Co-implanted ZnO nanowires

S. Geburt, J. Segura-Riuz\*, G. Martínez-Criado\*, M. H. Chu\* and C. Ronning

\*European Synchrotron Radiation Facility, Experiments Division, 38043 Grenoble, France

Doping of semiconductor nanostructures is the key feature to modify and enhance their optical, electrical and magnetical properties [1]. Unfortunately, doping during growth is a difficult task owing to the sensitive growth conditions. Ion implantation of nanostructures was proven as a reliable method to overcome all the limitations [2]. But the ion beam treatment has a severe impact on the crystal structure and the shape of nanostructure [3] leading to an appropriate method reducing the damage, usually reached by thermal annealing. Therefore, it has to be investigated if the nanostructures behave like their bulk counterparts or if ion beam and annealing treatment leads to inhomogeneous concentrations, dopant segregation and/or secondary phase formation.

A suitable method is needed for direct probing of a nano-sized sample volume with a stoichiometric sensitivity better than 0.3 at.% in combination with structural information like microstructure, valence states and lattice disorder information on the nanometer scale. Nano-X-ray absorption spectroscopy including X-ray fluorescence (XRF), X-ray absorption near edge spectroscopy (XANES) and extended X-ray absorption fine structure spectroscopy (EXAFS) have been successfully applied for the stoichiometric and structural investigation of single ZnO nanowires [4,5] implanted with  $1.55 \cdot 10^{16} \text{ cm}^{-2}$  Co (60-300 keV), corresponding to a nominal concentration of 0.6 at% obtained from simulations using the iradina code [6]. Subsequent annealing at 750°C for 240 min in air was performed to recover the implantation damage.

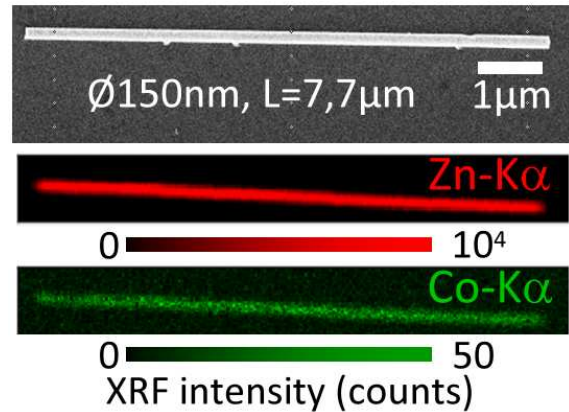


Fig. 1: SEM and nano-XRF mapping images of a single Co-implanted ZnO nanowire: The Zn and Co show a clear correlation. No cluster or segregations were found meaning that homogenous doping was achieved.

The nano-X-ray spectroscopy was performed at the ID22 NI beamline of the ESRF. The monochromatic X-ray beam was focused by a pair of Kirkpatrick-Baez mirrors to a spot size of  $100 \times 100 \text{ nm}^2$  with  $\sim 10^{11}$  ph/s flux. The XRF signal was obtained using a Si drift detector. The XRF maps were collected with 12 keV X-ray energy and a pixel size of  $25 \times 25 \text{ nm}^2$ .

The Zn-K $\alpha$  signal (Fig. 1) clearly reproduces the nanowire shape obtained from SEM images. For Co, the same elemental distribution and no hints for inhomogeneity within the detection limit were found, which suggest a co-localization of Zn and Co within the nanowire [4]. The Co concentration was determined to  $0.3 \pm 0.1$  at.%. Due to the high spatial confinement of the X-ray beam, XANES spectra recorded in XRF mode with a step size of 1 eV could be taken at several positions on the nanowire (Fig. 2). The Zn K-edge signal reflects the spectral features of wurtzite ZnO. No signature of metallic Zn precipitates were observed, the line shape and peak en-

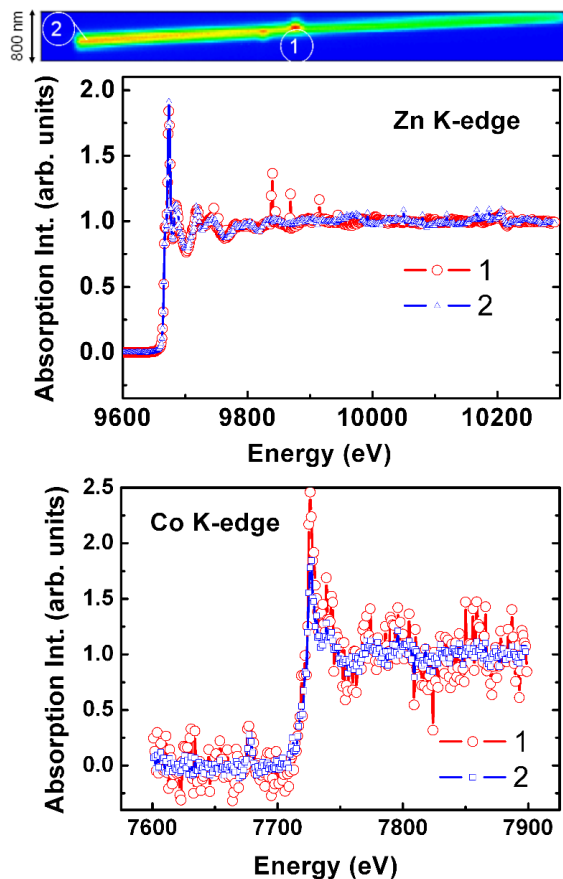


Fig. 2: XANES measurements at different points on the nanowire: The Co K-edge reproduces well the oscillations of the Zn signal indicating  $\text{Co}^{2+}$  ions incorporated substitutional on Zn sites in wurtzite host lattice.

ergies suggest a nearly perfect structural order of the implanted nanowire [5]. The XANES data of the Co K-edge reproduces well the oscillations of the Zn K-edge, therefore the Co ions seem to be incorporated on Zn sites in the wurtzite host lattice. Considering the chemical composition, the spectra were compared to metallic Co, mixed valence  $\text{Co}_3\text{O}_4$  and a high quality ZnCoO film. No contributions for metallic and/or mixed valence contributions were observed suggesting an oxidation state of 2+ for the Co ions.

The local structure was probed using EXAFS around the Zn K-edge at several positions on the nanowire. Data analysis of the oscillations accompanied by their best fits was carried out in the interval  $0\text{-}8.1 \text{ \AA}^{-1}$ . The fit routine included a nearest neighbor

shell of 4 O atoms and 12 second nearest neighbor shell of Zn atoms. The interatomic distances and Debye-Waller factors were obtained from the fits. For several probing points, no change in the interatomic distances compared to pure ZnO were found giving evidence for an undisturbed lattice around the Zn site without any signs of amorphization. The increased Debye-Waller factors compared to the undoped material can be partly explained by the weaker binding of the substitutional Co ions to the lattice. The data suggest a nearly complete recovery of the implantation defects with no hints for secondary phases, vacancy accumulations or interstitials.

The results were further confirmed by TEM investigations showing single crystalline Co-implanted ZnO nanowires with a nearly perfect lattice. The spacing of the (0002)-planed obtained by FFT is 0.52 nm and in good agreement with literature values for ZnO. Only in some nanowires, defects like stacking faults or dislocations were found with can further explain the increased Debye-Waller factors determined by EXAFS. Nano-X-ray absorption spectroscopy was proven to be a valuable method for the correlation of stoichiometric and structural properties of single implanted nanowires on the nanometer scale.

## References

- [1] C. Ronning et al. *Mat. Sci. Eng. R.* **70**, 30 (2010)
- [2] C. Ronning et al. *Phys. Stat. Sol. B* **10**, 2329 (2010)
- [3] C. Borschel, PhD thesis, Uni Jena 2011.
- [4] M. H. Chu et al. *Phys. Stat. Sol. RRL* **5** (8), 283 (2011)
- [5] J. Segura-Ruiz et al. *Nanolett.* **11**(12), 5322 (2011)
- [6] C. Borschel, *NIM B* **269**, 2133 (2011)

# Contacting of ZnO nanowires by dielectrophoresis and electrical characterization

D. Cammi, I. Slowik, R. Niepelt, U. Schröder\*, M. Gnauck, and C. Ronning

*\*Institut für Photonische Technologien, Jena*

ZnO nanowires are promising candidates for the realization of nanoscale devices, such as field effect transistor, photodetectors, chemical and bio-chemical sensors. One of the most challenging issues for the large-scale production of these NW-based devices is the manipulation and the alignment of nanowires between metal electrodes. For this purpose, several techniques have been exploited in the last years. Among these dielectrophoresis, a standard method used for moving neutral particles suspended in a medium using a nonuniform electric field, presents several promising features. In the present report, we describe the successful contacting of ZnO nanowires using dielectrophoresis in isopropanol along with the electrical characterization.

Applying a nonuniform electric field between electrodes, the induced polarization on ZnO nanowires dispersed in a liquid medium will induce a movement toward the direction of the highest field gradient [1]. The resulting force:

depends on the electric field gradient and the complex dielectric functions of the nanowire and the medium via the Clausius-Mossotti factor:

$$F_{DEP} = \frac{1}{2} \nabla \cdot \text{Re}[\chi] E^2$$

Zinc oxide nanowires have been grown from ZnO powder (99.99% purity) on silicon substrates in a vapor-liquid solid growth process [2]. The substrates were

subsequently immersed in few cubic millimetres of isopropyl alcohol and ultrasonicated for 4-5 seconds to disperse NWs in the liquid. A droplet was deposited on a prepatterned commercial chip with electrodes in nichel-chromium alloy and an alternating voltage ( $V_{pp} = 5V$ ) has been applied. We considered different values of the electric field frequency in order to maximize the Clausius-Mossotti factor and consequently the dielectrophoresis force. The successful contact of nanowires between electrodes has been checked using an optical microscope. The subsequent electrical characterization has been performed using a Source-measure Unit (SMU) Keithley Model 237.

A calculation of the Clausius-Mossotti factor shows that the dielectrophoresis force starts to decrease above 10 kHz, as evident in Fig 1. To check the reliability of the theoretical model we varied the frequency from 1 kHz to 10 MHz and we found that above 10 kHz the number of contacted nanowires is very low, according to the calcu-

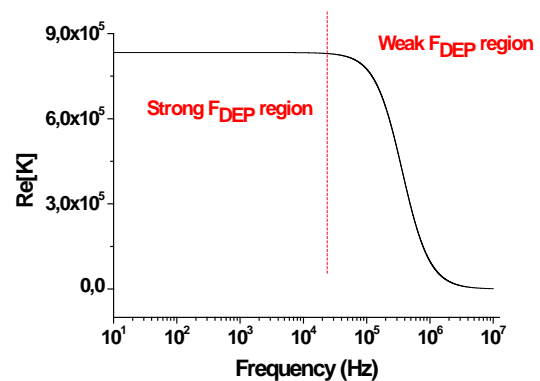


Fig. 1: Real part of the Clausius Mossotti factor as a function of the electric field frequency. Above 10 kHz the dielectrophoresis force acting on the nanowires decrease considerably.

lated graph (Fig 2). The experimental results disagree with the expected behavior at 1 kHz, probably because a more sophisticated model should be taken into account for the low frequency region. Thus we chose 10 kHz as the best value for the frequency. The typical I-V characteristic of the contacted nanowires in the dark shows mainly a rectifying behavior, as appears in Fig. 2, with different heights of the Schottky barriers on both sides of the metal-semiconductor-metal structure. The curve obtained under UV illumination is instead more symmetrical and the value of the current is considerable higher. This is due to desorption of oxygen from the nanowire surface: in the dark oxygen molecules adsorb on the surface, trapping electrons from the conduction band and thus decreasing the carrier density and the mobility of the nanowire. Under UV illumination, the photogenerated holes discharge the ad-

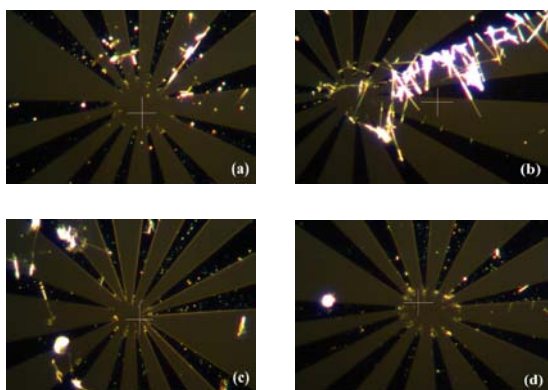


Fig. 2: Dark-field images of the contacted NWs with different electric field frequencies: 1 kHz (a), 10 kHz (b), 100 kHz (c), 1 MHz (d). Using 10 kHz is clearly the best value.

sorbed oxygen, and the consequent release of electrons contributes to the strong increase of conductivity. The decay of the current after switching off the above-gap illumination (inset of Fig 3) is very slow and strongly depends on the oxygen re-adsorption mechanism on the nanowire sur-

face, although a complete understanding of this effect has not completely achieved yet [3,4].

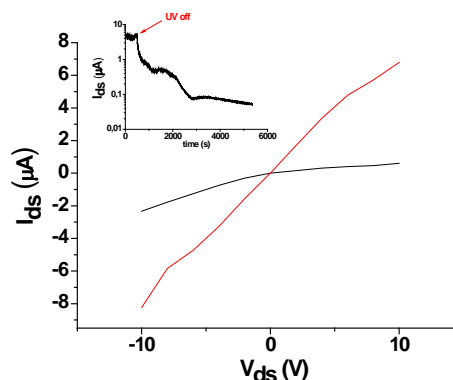


Fig. 3: I-V characteristic in the dark (black) and under UV illumination (red) of nanowire contacted by dielectrophoresis. The inset shows the decay of photoconductivity ( $V_{ds} = 5$  V, measurements performed in air)

In conclusion, we demonstrated the successful contacting of ZnO nanowires by means of dielectrophoresis in isopropyl alcohol. The electrical characterization confirmed the expected characteristic of Schottky barrier between the electrodes and the semiconductor and the persistent of photoconductivity. Thus, dielectrophoresis represents a promising alternative to the photolithography process, because allows to save some steps that may alter the surface properties of the nanowires.

#### References:

- [1] H.A. Pohl, "Dielectrophoresis: the behaviour of neutral matter in nonuniform electric fields" Cambridge University Press, 1978
- [2] U. Schröder, Diploma thesis, FSU 2010
- [3] Bao et al., Nanoscale Research Letters **6** (2011) 404
- [4] Prades et al., Nanotechnology **19** (2008) 465501

# Realization and measurement of planar, edge-type and grain boundary Josephson junctions based on iron pnictide superconductors for examination of their order parameter symmetry

S. Döring, S. Schmidt, F. Schmidl, V. Tympel, K. Iida<sup>1</sup>, S. Haindl<sup>1</sup>, F. Kurth<sup>1</sup>, J. Hänisch<sup>1</sup>, T. Thersleff<sup>1</sup>, L. Schultz<sup>1</sup>, I. Mönch<sup>2</sup>, B. Holzapfel<sup>1</sup> and P. Seidel

<sup>1</sup> Institute for Metallic Materials, IFW Dresden, Helmholtzstraße 20, D-01069 Dresden Germany

<sup>2</sup> Institute for Integrative Nanosciences, IFW Dresden, Helmholtzstraße 20, D-01069 Dresden Germany

Since the discovery of the iron-based superconductors in 2008, many works were performed to investigate their order parameter. Most investigations using point-contact Andreev Reflexion studies or tunnelling spectroscopy obtained differing information about the gap number and their symmetry [1]

For the electron-doped material  $\text{BaFe}_{2-x}\text{Co}_x\text{As}_2$  there is a proposal from Mazin [2] about the order parameter, assuming one (or more) hole-like gap(s) at the  $\Gamma$ -point and one (or more) electron-like gap(s) at the M-point. This is called  $s_{\pm}$ -symmetry. Most experiments performed are sensitive to the order parameter amplitude but not to its phase. A geometry for a device which allows phase-sensitive tests on an iron-pnictide was proposed by Parker and Mazin [3] and is shown in fig. 1.

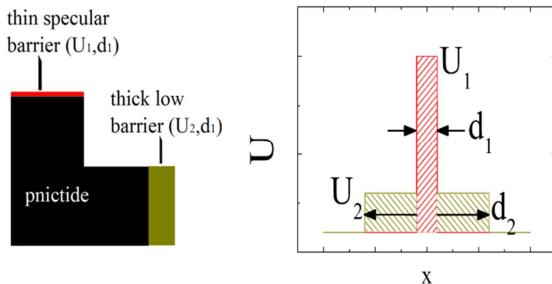


**Fig 1:** Left: A schematic view of possible tunnelling geometry for phase-sensitive tests of order parameter symmetry of iron pnictide. Right: Explanation of the respective barrier parameters.

Such a device contains two interfaces with different barriers in ab-plane and c-axis direction. In one direction, there is a thin specular barrier, allowing a current

transport, which is dominated by electrons. In the other direction, there is a thicker barrier ( $\geq 2$  nm) with finite height. This one suppresses the tunnelling of electrons by many magnitudes, while the hole transport stays comparatively uninfluenced. The behaviour is vice versa for a hole-doped material.

We plan to realize these devices by using a combination of different junction types. Previously, we worked on single-junctions in one direction, c-axis, or ab-plane, respectively.

The first junction type was a planar one for measuring in c-axis direction, using a 5 nm gold layer as barrier between a Ba-122 base electrode produced by a standard pulsed laser deposition technique at IFW Dresden [4] and a PbIn counter electrode. This junction type showed clear Josephson effect (fig. 2) with  $I_C R_N$  equals  $4.4 \mu\text{V}$ . [5]

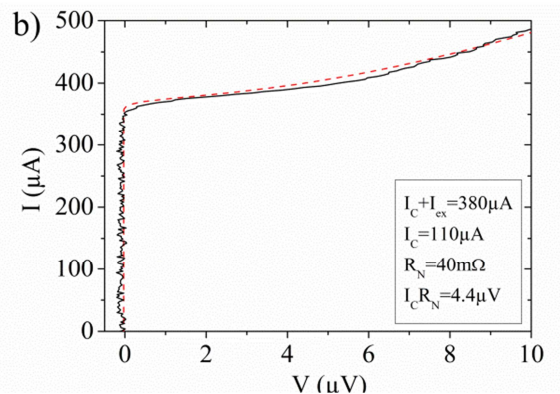


**Fig 2:**  $I$ - $V$ -characteristic of a hybrid planar SNS-Josephson junction with Ba-122 base electrode, a 5 nm gold barrier and a PbIn counter electrode at  $T = 4.2$  K. [5]

The second type was an edge junction in ab-plane direction, also with PbIn as counter electrode. Instead of an artificial barrier, the interface properties between the electrodes were changed to obtain a different coupling/weak link. The edge junction type also showed a critical Josephson current (fig. 3) and an  $I_C R_N$  product of  $10 \mu\text{V}$ .

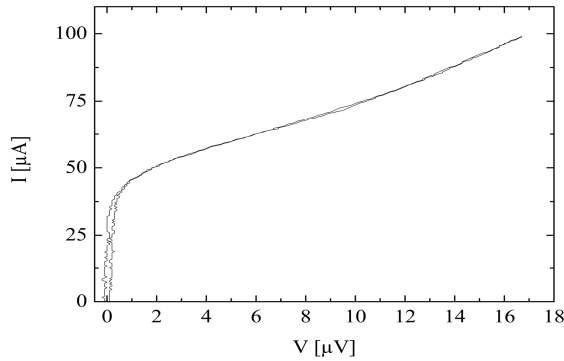


**Fig. 3:**  $I$ - $V$ -characteristic of a hybrid edge Josephson junction with Ba-122 base electrode, an interface engineered barrier and a PbIn counter electrode at  $T = 4.2 \text{ K}$ .

A third type of junction was realized on a MgO bicrystal substrate [6]. The Josephson behaviour is most probably caused by the grain boundary within Ba-122 (see fig. 4). This junction type has an  $I_C R_N$  product of about  $20 \mu\text{V}$ .

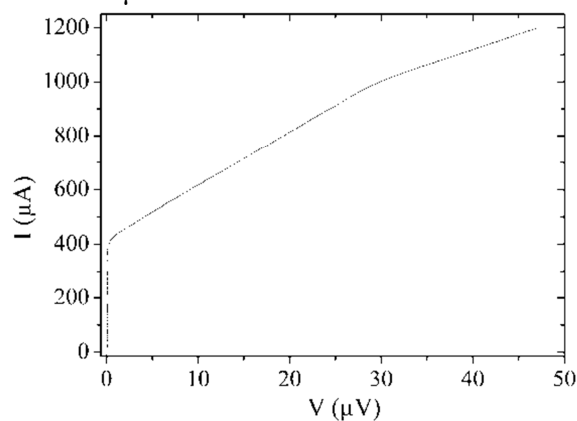


**Fig. 4:**  $I$ - $V$ -characteristic of grain-boundary junction within Ba-122 at  $T = 4.2 \text{ K}$ .

Now we have three completely different types of Josephson junctions. There is a planar one, with a normal conductor thick barrier and transport along the  $c$ -axis and two junctions with transport within the ab-

plane across thin barriers. We showed that any of these junction types can be prepared and measured as single type device.

This is the base to prepare a device similar to the proposed one in [3]. One possibility is a combination of the planar and the edge junction as shown in fig. 5. Also possible is the use of a bicrystal substrate for combining a planar junction with gold barrier and a grain-boundary junction.

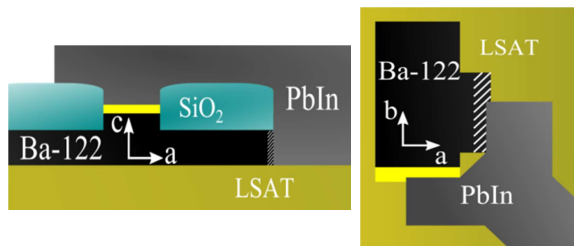


**Fig. 5:** Schematic views of a possible layout for a phase-sensitive device, containing a planar SNS-junction and an edge junction. Left: cross-section view. Right: top view. [7]

The future work will be a complete characterization of each single junction type, to obtain exact parameters for the dimensions of a combined device and finally a mask design to prepare such a device and performing measurements on it.

This work was partially supported by the DFG under SPP 1458 (project nos. SE 664/15-1 and HA 5934/3-1), the EU under project IRON-SEA (project no. FP7-28314) and the Landesgraduiertenförderung Thüringen.

## References

- [1] P. Seidel, Supercond. Sci. Technol. **24** 043001 (2011)
- [2] I.I. Mazin, Phys. Rev. Lett **101** 057003 (2008)
- [3] D. Parker and I.I. Mazin, Phys. Rev. Lett. **102** 227007 (2009)
- [4] K. Iida et al., Phys Rev B **81** 100507 (2010)
- [5] S. Schmidt et al., Appl. Phys. Lett. **97** 172504 (2010)
- [6] T. Thersleff et al., Appl. Phys. Lett. **97** 022506 (2010)
- [7] S. Döring et al., Proceedings ISS 2011 accepted by Physics Procedia

# Domain Wall Dynamics in Soft Magnetic Nanostripes

S. Glathe<sup>1</sup>, R. Mattheis<sup>1</sup>, P. Seidel

<sup>1</sup> Institute of Photonic Technology (IPHT), Albert-Einstein-Str. 9, 07745 Jena

The magnetic properties of soft magnetic nanostripes, with a cross section of e.g. 20 x 150 nm<sup>2</sup> and a length of 10 μm to 1 mm, are mainly determined by their geometry. The magnetization of such nanostripes can only be parallel to the long axis of the nanostripe, and domains of antiparallel magnetization are separated by a so-called domain wall (DW). The potential for using such systems in high density storage applications is being investigated by many groups [1-2]. We are using these structures to resolve a still unsolved problem: We develop, together with the company Novotechnik, a new sensor, that is able to count the number of rotations, is wear-free, and fulfills the true-power-on criteria for the drive-by-wire concept of the automobile industry [3-4]. For such an application a permanent magnet, mounted on the steering column, rotates over a fixed angle sensor, which determines the angular position of the magnet. However, a multi-turn sensor is indispensable when trying to distinguish between 10° and 370° or -350°.

Crucial for the above-mentioned application is the reliable control of the DW position and thus the DW movement. The permanent magnet produces a field component parallel to the nanostripe along the axis (longitudinal field,  $H_{\text{long}}$ ), which is the driving force for the DW motion. Perpendicular to this field, a transverse field component (transverse field,  $H_{\text{tr}}$ ) acts on the DW motion, too.

The dependency of the DW velocity  $v_{\text{dw}}$  on the driving field  $H_{\text{long}}$  is not linear, as intuitively expected. The reason for this is a periodic component in the forward motion of

the DW above a critical field, the so-called Walker breakdown field  $H_{\text{W}}$ . We have directly visualized this transition between a laminar and a stop-and-go movement for the first time in single shot measurements using GMR nanostripes [5].

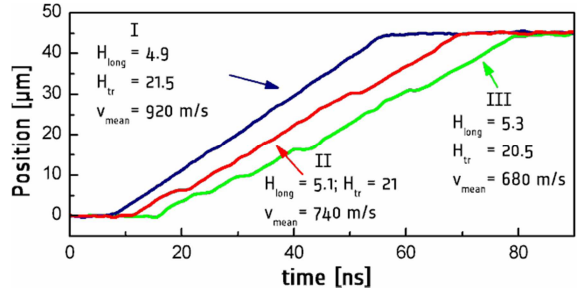


Fig. 1: Single measurements of the DW position in dependence on the time. All fields in kA/m. The three cases are shown in Fig. 2, too.

The blue curve I in Fig. 1 shows the DW motion directly below  $H_{\text{W}}$ . Increasing the driving field  $H_{\text{long}}$  even slightly (red [II] and green [III] curve) causes the mean velocity of the DW to drop due to the stops of the DW that then occur during movement. During these stopping periods the DW undergoes transformation processes. We observed that the Walker breakdown process is not periodic. Due to the edge roughness of the nanostrip, the time between the two stopping periods varies stochastically.

Fig. 2 shows the results of a systematic examination of the influence of transverse fields on the DW dynamics in a 45 μm long nanostripe [6]. The transverse field affects both the static magnetization configuration and the magnetization dynamics, which determine the DW dynamics. The influence on the static configuration appears in the dependence of the longitudinal field on the transverse field (black curve in Fig. 2). The plotted longitudinal field is required to nu-

create a DW at the coevally applied transverse field. After nucleation the DW is driven by this longitudinal field through the nanostripe.

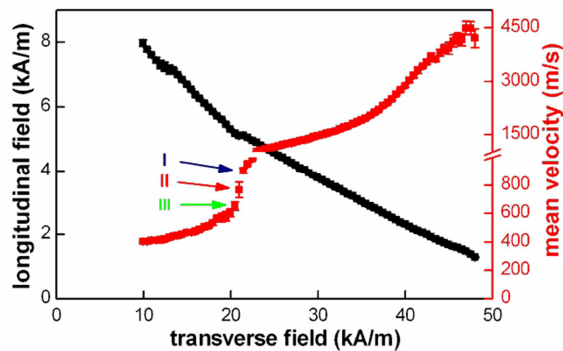


Fig. 2: Dependence of  $H_{\text{long}}$  and  $v_{\text{Dw}}$  on  $H_{\text{tr}}$

The decreasing longitudinal field with increasing transverse field can be explained by the decreasing DW angle with increasing  $H_{\text{tr}}$  and allows us to control the driving field  $H_{\text{long}}$  with  $H_{\text{tr}}$  as parameter.

The red plot in Fig. 2 shows the dependence of the DW velocity on the applied transverse field. The velocity increases nonlinearly with the transverse field. Our maximum velocity of 4500 m/s is remarkable, in particular with the very small longitudinal driving fields. These velocities are three times the maximum velocities reported earlier. These velocities can be explained by the influence of  $H_{\text{tr}}$ , which change the DW profile and thus the mobility of the DW.

In another study we discovered a new type of DW movement below the critical Walker field. This new type was discovered using the GMR single shot technology and could be verified and explained by means of micromagnetic simulations [8]. Fig. 3 shows snapshots of the simulated DW movement. The magnetization components are color coded according to the color wheel. The DW can be seen as composition of two parts, which in this case behave independently from each other. The upper part moves with a constant velocity in a steady state regime, while the lower one moves in

a periodic manner with periods when this part of the DW completely stops.

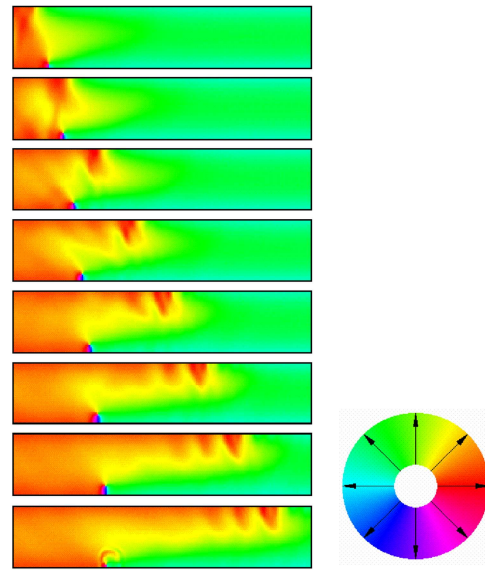


Fig. 3: Magnetization configuration according to the color wheel of the stabilized split DW. The time interval between the rows is 0.1 ns. The driving field is below the critical Walker field.

In conclusion we have shown the necessity of using single shot measurements for the characterization of DW movement in GMR nanostripes. The Walker process could be experimentally verified in single shot measurements for the first time and it was shown that this process is stochastic. Moreover the single shot technique enabled us to discover a new kind of DW movement, which could be verified and explained by micromagnetic simulations.

## References

- [1] S.S.P. Parkin et al., *Science*, **320**, 190 (2008)
- [2] R. Cowburn US020070047156 A1, US 2005\_0226103A1
- [3] M. Diegel et al., *Sensor Lett.*, **5**, 118 (2007)
- [4] M. Diegel et al., *IEEE Trans. Magn.*, **45**, 3792 (2009)
- [5] S. Glathe et al., *Appl. Phys. Lett.*, **93**, 072508 (2008)
- [6] S. Glathe et al., *Appl. Phys. Lett.*, **93**, 162505 (2008)
- [7] S. Glathe et al., *Phys. Rev. B*, **81**, 020412(R) (2010)
- [8] D. V. Berkov and N. L. Gorn, *MicroMagus*: package for micromagnetic simulations, <http://www.micromagus.de>



# Ion beam synthesis of silver clusters in lithium niobate

S. Milz, J. Rensberg, C. Ronning, and W. Wesch

In the last two decades plasmonic structures gained a lot of interest due to their wide range of possible applications, like sensing [1], fast information transfer [2] and the confinement of light [3]. Promising plasmonic structures are nanometer sized metal clusters embedded in dielectric host materials. One of the most important embedding media is lithium niobate ( $\text{LiNbO}_3$ ). Because of its unique optical properties, like large electro-optical and nonlinear optical effects, it is one of the materials of choice for the development of integrated optical devices [4]. Therefore, the combination of plasmonic structures and lithium niobate opens a wide range of new applications; one example is the increase of nonlinear refractive indices due to the incorporation of metal clusters [5].

We investigated the ion beam synthesis of silver nanoclusters in  $\text{LiNbO}_3$  for various implantation temperatures [6]. At room temperature 380 keV  $\text{Ag}^+$  ions were implanted in  $\text{LiNbO}_3$  to an ion fluence of  $1 \times 10^{17} \text{ cm}^{-2}$ . Subsequent to the ion implantation process, rapid thermal annealing was performed in order to recover the crystal

structure and to control the cluster size distribution. Post implantation annealing was carried out in a double graphite strip heater in an argon ambient at a partial pressure of 100 mbar. Each sample was successively annealed for 30 s at temperatures ranging from 573 to 1173 K in steps of 50 K. The samples were analysed after each annealing step by means of Rutherford backscattering spectroscopy in channeling configuration (RBS/C), (scanning) transmission electron microscopy (STEM/TEM) and UV-VIS spectroscopy.

The RBS/C spectra from the niobium part are shown as a function of the subsequent annealing temperature in figure 1. The initially 260 nm thick amorphous layer recrystallizes from the substrate towards the surface with increasing annealing temperature, but a heavily damaged surface layer remains. Large silver clusters formed at high annealing temperatures (see below) might be the reason for this because they stress the matrix and therefore enhance the dechanneling.

STEM images of selected annealing steps are shown in figure 2. No significant cluster growth can be seen until 873 K. Starting at 973 K, the cluster sizes increased, reaching a maximum cluster size of about 20 nm at 1173 K. The number of smaller clusters significantly decreased. This is a consequence of growth of large clusters at the expense of smaller ones due to Ostwald ripening.

The UV-VIS spectra of the silver implanted  $\text{LiNbO}_3$  samples successively annealed to 1173 K are displayed in figure 3. Note that the spectra were normalized to the same minimum value at the wavelength of 340 nm. Directly after Ag implantation at

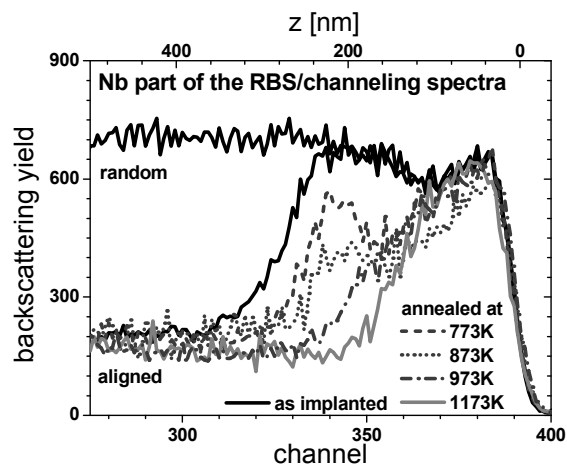


**Fig. 1:** RBS/C spectra of the Nb signal of  $\text{LiNbO}_3$  implanted with 380 keV Ag ions as a function of the annealing temperature performed in a RTA system.

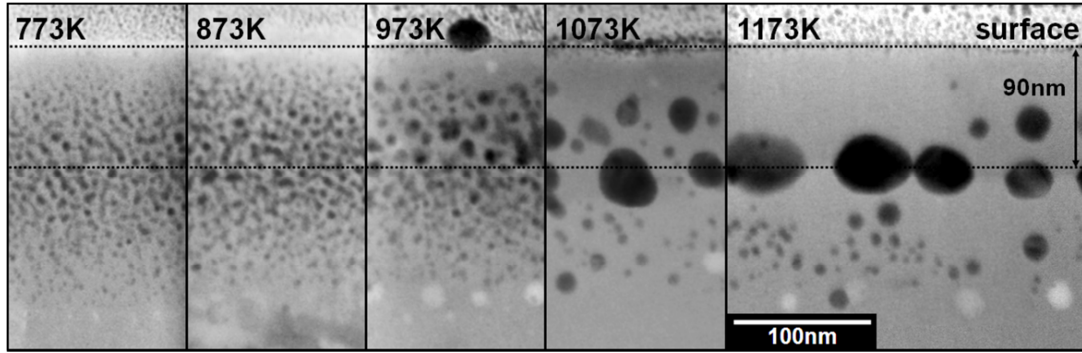


Fig. 2: STEM images of a Ag-implanted LiNbO<sub>3</sub> sample as a function of the annealing temperature.

room temperature a broad absorbance peak positioned around the wavelength of 480 nm appears in the transmission spectrum. This so called surface plasmon resonance (SPR) peak is predicted by the Mie scattering theory, which describes absorption and scattering of light by small spherical particles [7]. For the as implanted sample the SPR peak wavelength is about

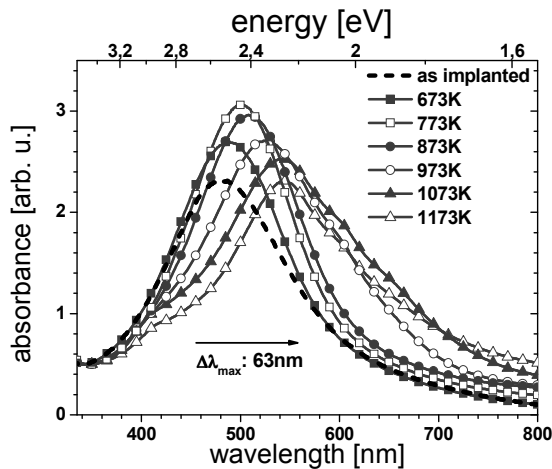


Fig. 3: UV-VIS transmission spectra for various annealing steps an Ag-implanted LiNbO<sub>3</sub> sample.

480 nm, and with increasing annealing temperatures this peak shifts towards longer wavelengths. With the knowledge that the cluster radius does not differ very much for temperatures below 887 K, (see fig. 2), only a change of the refractive index of the host matrix during the thermal annealing can explain this redshift [5,8]. This is in good agreement with our RBS investigations. In the as implanted stage the clusters are obviously embedded in amorphous or heavily

damaged LiNbO<sub>3</sub>. With increasing annealing temperature the lattice structure partly recovers, and the clusters are now embedded in partially crystalline LiNbO<sub>3</sub> with an increased refractive index. As a consequence, a red-shift of the SPR peak position is observed. At temperatures above 887 K the cluster sizes significantly increase. This can explain the further redshift.

To summarize this work, the formation of nanoclusters by means of silver implantation into lithium niobate was successfully demonstrated. Thermal annealing was performed to recrystallize the LiNbO<sub>3</sub> and increase the cluster sizes. After implantation, a SPR peak centered around 480 nm occurs and redshifts with increasing annealing temperature due to the recrystallization of LiNbO<sub>3</sub> and cluster growth.

Financial support by the Federal Ministry of Education and Research (BMBF) within the project „Photonic Nanomaterials“ (PhoNa) is acknowledged.

## References

- [1] J. Homola et al., *Sensor Actuat. B-Chem*, **54**, 3-15 (1999).
- [2] S. A. Maier, *IEEE J. Quantum Electron.*, **12**, 1671-1677 (2006)
- [3] S. A. Maier et al., *Nat. Mater.*, **2**, 229-232 (2003)
- [4] F. Chen, *J. Appl. Phys.*, **106**, 081101 (2009)
- [5] E. K. Williams et al., *Nucl. Instr. and Meth. B*, **141**, 268-273 (1998)
- [6] S. Milz et al., *Nucl. Instr. Meth. B* (2012), doi:10.1016/j.nimb.2011.11.026
- [7] G. Mie, *Ann. Phys.*, **330**, 377-445 (1908)
- [8] G. O. Amolo et al., *Nucl. Instr. and Meth. B*, **250**, 233-237 (2006)

## Damage formation in SiC ion implanted at 625 K

E. Wendler, Ph. Schöppe, Th. Bierschenk, St. Milz, W. Wesch, N.G. van der Berg\*,  
E. Friedland\*, J.B. Malherbe\*

\*Physics Department, University of Pretoria, 0002 Pretoria, South Africa

SiC is known to be a promising material for high-power and fast switching electronic systems produced by ion implantation and operating in harsh environments. Further it is a material with potential use in nuclear technologies. For both applications the interaction of SiC with energetic ions is of importance.

To study the influence of ion species on damage formation in 4H-SiC at 625 K, the results for 360 keV Ag ions are compared with that for dual Si/C ion implantation whereby firstly 105 keV Si and secondly 45 keV C ions were implanted to the same ion fluence to preserve the stoichiometry of the material.

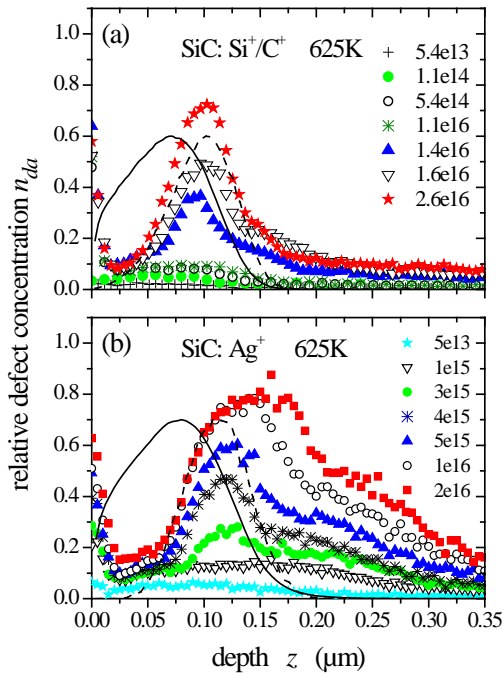


**Fig. 1:** Relative defect concentration versus depth,  $n_{da}(z)$ , (a) for dual Si/C and (b) for Ag ion implantation of SiC at 625 K. The ion fluences  $N_I$  are given in  $\text{cm}^{-2}$ . For comparison the distribution of primary displacements and implanted ions are given in arbitrary units by the solid and dashed line, respectively.

Rutherford backscattering spectrometry (RBS) in channelling configuration is used

to detect the relative concentration of displaced lattice atoms  $n_{da}$  versus depth  $z$  referred to as defect concentration in the following text [1]. Fig. 1 shows the depth dependence of the defect concentration for Ag and Si/C implanted SiC for various ion fluences. For comparison the distribution of primary displacements and implanted ions calculated with SRIM [2] are included.

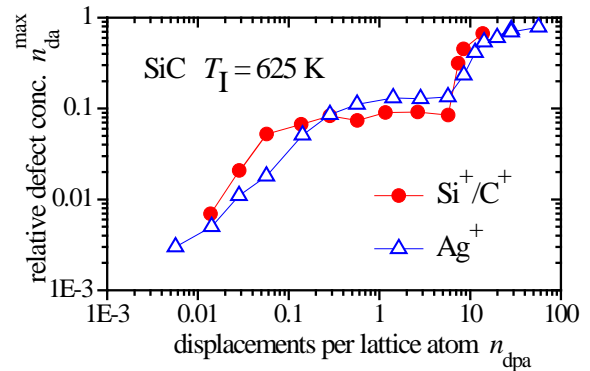


**Fig. 2:** Relative defect concentration taken at the maximum of the measured distributions,  $n_{da}^{\text{max}}$ , versus the number of displacements per lattice atom,  $n_{\text{dpa}}$ , for Si/C and Ag ion implantation of SiC at 625 K.

The damage concentration in the maximum of the measured distributions,  $n_{da}^{\text{max}}$ , is shown in Fig. 2 versus the number of displacements per lattice atom  $n_{\text{dpa}}$ . This quantity is a normalized ion fluence taking into account the energy deposited into atomic collision processes per implanted ion [3].

From Fig. 2 it can be seen that in general the same evolution of damage is found independent whether self-ions or Ag ions are implanted. The damage formation proceeds in two steps. The maximum defect concentration increases at similarly low numbers of displacements per lattice atom,  $n_{\text{dpa}}$ , for both series of implantation. A first plateau of  $n_{da}^{\text{max}}$  is observed for  $0.1 < n_{\text{dpa}} < 6$  dpa

which can be explained by a balance between defect generation and recombination. A second increase of the damage concentration occurs at  $n_{\text{dpa}} \approx 6$  dpa followed by a second plateau which is clearly visible for Ag implantation but not yet reached in the case of Si/C implantation. Saturation is reached at a value well below unity which indicates that the layers are not rendered amorphous (see also Fig. 1).

From Fig 1 it can be seen that the second increase of  $n_{\text{da}}^{\text{max}}$  starting at around 6 dpa with  $n_{\text{da}}^{\text{max}} > 0.2$  occurs at the depth of maximum ion concentration. From this observation it can be concluded that the onset of this pronounced damage formation is triggered by the implanted ions themselves. The critical fluences for this onset correspond to a relative ion concentration in the maximum of the ion distribution of 0.4% in case of Ag implantation and 0.9% Si plus 0.9% C in case of the dual implantation. For these values no significant formation of precipitates is to be expected. One possible explanation for the effect of the ions may be related to the volume introduced into the implanted layer by the implanted ions. The relative volume change  $\Delta V/V$  can be estimated and a value of about  $6 \times 10^{-3}$  is obtained in both cases [3]. Although this is only a rough estimate – the atomic radii may change depending on the charge state of the implanted species – it can be taken as a hint that an enhancement of the defect formation occurs when the relative volume increase introduced by the implanted ions exceeds some critical value. Further work is underway to prove this finding.

Information about the kind of defects produced for high ion fluences ( $n_{\text{dpa}} > 6$  dpa) is obtained from the channeling spectra and from TEM. The long artificial tails of the damage concentration shown in Fig. 1 indicate the existence of extended defects. For comparison cross section TEM images were

taken [3]. One example is shown in Fig. 3. A broad defective region can be seen. The width of this band is in agreement with the width of the corresponding damage peak measured by RBS (see Fig. 2). At larger depths the material is almost completely defect-free as demonstrated by the TEM images whereas the RBS profiles exhibit long tails which are thus obviously artificial [3]. From Fig. 3 it can be seen that the layer structure characterizing the crystalline material, is also visible within the band of defects. This means, the SiC within the defect band is still partially crystalline. Many dark structures with a size of few nanometers can be seen, which may be some kind of defect clusters. High-resolution TEM is necessary to resolve these structures.

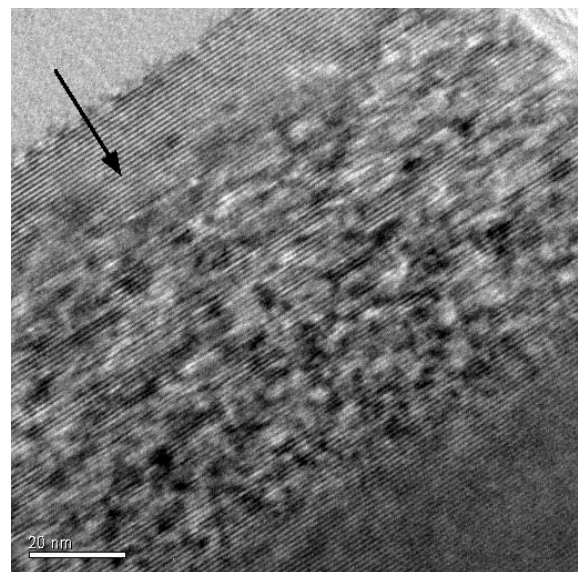


**Fig. 3:** Cross section TEM images of SiC implanted at 625 K with Si/C ions to  $2.6 \times 10^{16} \text{ cm}^{-2}$ . The given ion fluence corresponds to about 14 dpa. The arrow in the images indicates the direction of implantation.

#### References

- [1] K. Gärtner, Nucl. Instrum. and Meth. B 227 (2005) 522.
- [2] J.P. Biersack and J.F. Ziegler, *The Stopping and Ranges of Ions in Matter*, Vol. 1, Pergamon Press, Oxford, 1985 ; [www.srim.org](http://www.srim.org).
- [3] E. Wendler, Ph. Schöppe, Th. Bierschenk, St. Milz, W. Wesch, N.G. van der Berg, E. Friedland, J.B. Malherbe, Nucl. Instrum. and Meth. B 2012, in press.

# Damage formation and optical absorption in neutron irradiated SiC

E. Wendler, Th. Bierschenk, F. Felgenträger, J. Sommerfeld, W. Wesch, D. Alber\*,  
G. Bukalis\*, L.C. Prinsloo\*\*, N. van der Berg\*\*, E. Friedland\*\*, J.B. Malherbe\*\*

\*Campus Lise-Meitner, Abteilung F-A1, Elementanalytik, Helmholtz-Zentrum Berlin für Materialien und Energie GmbH, Hahn-Meitner-Platz 1, 14109 Berlin, Germany

\*\*Department of Physics, University of Pretoria, 0002 Pretoria, South Africa

Neutron irradiation of SiC was performed at the reactor BER II at the Helmholtz-Zentrum Berlin. The times of exposure varied between 1.3 and 297.7 h. To convert the times into neutron fluences  $N_n$  only epithermal and fast neutrons were taken into account (for details see [1]). The temperature during irradiation was less than 50 °C.

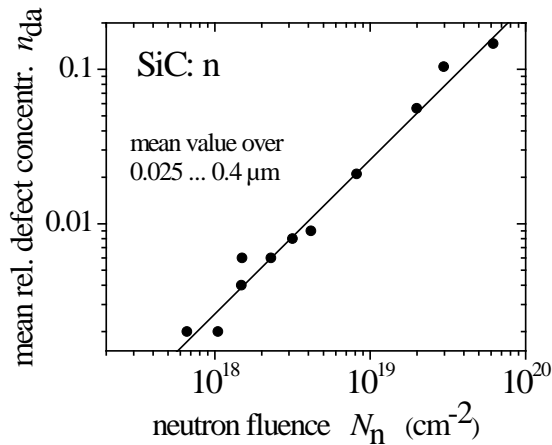


Fig. 1: Mean relative defect concentration  $n_{da}$  of neutron irradiated SiC versus the neutron fluences  $N_n$ . The line represents a linear increase of  $n_{da}$  with  $N_n$ .

Figure 1 shows the relative defect concentration  $n_{da}$  versus the neutron fluence  $N_n$ . Rutherford backscattering spectrometry was used to measure  $n_{da}$  and the given values are averaged over the first 0.4  $\mu\text{m}$  of the samples. A linear increase of the mean value  $n_{da}$  with rising neutron fluence  $N_n$  is found, which is applied to convert the neutron fluences into defect concentrations which is useful for comparison with data obtained for ion implanted SiC (see below). In Fig. 2 the spectral dependence of the absorption coefficient is shown for the neutron irradiated samples. The appearance is similar to that found for ion implanted SiC

(see [1] and references therein). The absorption coefficient versus wave number is characterized by a background increasing exponentially with increasing wave number and by a broad absorption band. The absorption band around wave numbers of  $12580\text{ cm}^{-1}$  was previously reported for neutron irradiated SiC [2] and attributed to Si vacancies. The existence of divacancies in ion irradiated SiC [3] and in neutron irradiated SiC [4] was deduced with the help of positron spectroscopy. Therefore, it can be assumed that the absorption band in SiC is caused by the divacancy  $V_{Si}V_C$ .

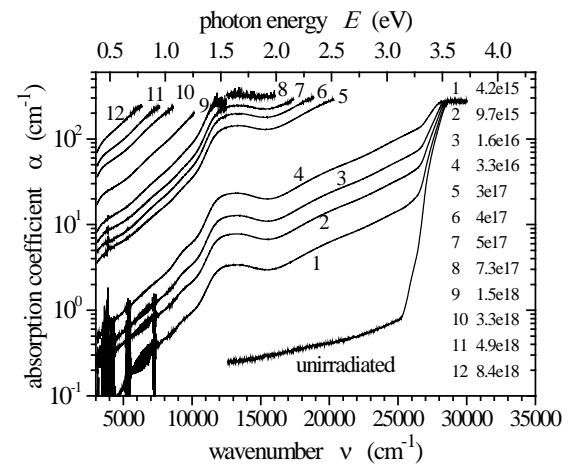


Fig. 2: Absorption coefficient  $\alpha$  versus the spectroscopic wave number  $\nu$  for neutron irradiated SiC. The neutron fluences  $N_n$  are given in  $\text{cm}^{-2}$ . For comparison the absorption coefficient of the SiC substrate is included.

In the spectral range  $16000\text{ cm}^{-1} < \nu < 25800\text{ cm}^{-1}$  the absorption coefficient follows a dependence  $\propto \exp(E/E_{01})$  with  $E_{01} = 0.7\text{ eV}$  independent of the neutron fluence. The same constant value was found for Au and Xe ions implanted into SiC at 400 °C [5]. Close to the direct band edge for  $\nu > 26600\text{ cm}^{-1}$  again an exponential in-

crease of the absorption coefficient  $\alpha$  is found represented by  $E_{02}$  which increases with increasing neutron fluence (corresponding to an increasing defect concentration) from  $E_{02} = 0.095$  eV for the lowest neutron fluence to  $E_{02} = 0.23$  eV for the highest. This latter subgap absorption tail is what is usually called Urbach tail, which exhibits tailing energies varying either with defect concentration or with temperature. The broad background tail with tailing energy  $E_{01}$ , which is typical for defective indirect semiconductors, may have a different physical origin (for details see [1]).

Figure 3 summarises the measured absorption coefficients  $\alpha$  versus the neutron fluence  $N_n$  for two different wave numbers. Additionally, the absorption coefficient in the maximum of the absorption band is shown after subtracting the background absorption. The results are compared with those obtained for B ion irradiated SiC. For both conditions a uniform almost linear dependence  $\alpha(n_{da})$  is found. This clearly confirms that the optical absorption is related to the defects produced by the irradiation with energetic particles. It also means that there is some correlation between the absorption within the band and the background absorption, which could be taken as an indication that both have the same origin. The four data points at very low concentrations belong to neutron irradiations which were performed with a significantly higher rate of thermal neutrons which were not taken into account when converting the exposure times to neutron fluences. Therefore, the systematic deviation of the data for the four lowest neutron fluences from the straight linear dependence in Fig. 3 suggests that the influence of the thermal neutrons cannot be completely neglected. A possible explanation are  $(n,\gamma)$  reactions of  $^{30}\text{Si}$  after neutron capture. The recoil energy due to the  $\gamma$

emission is large enough to cause the formation of a Frenkel defect.

From Fig. 3 it can be seen that the data for the B ion implanted samples with  $n_{da} > 0.1$  tend to deviate from the linear slope. This suggests that more complex defect structures start to form for relative defect concentrations  $n_{da} > 0.1$ , which change the optical properties in a different way.

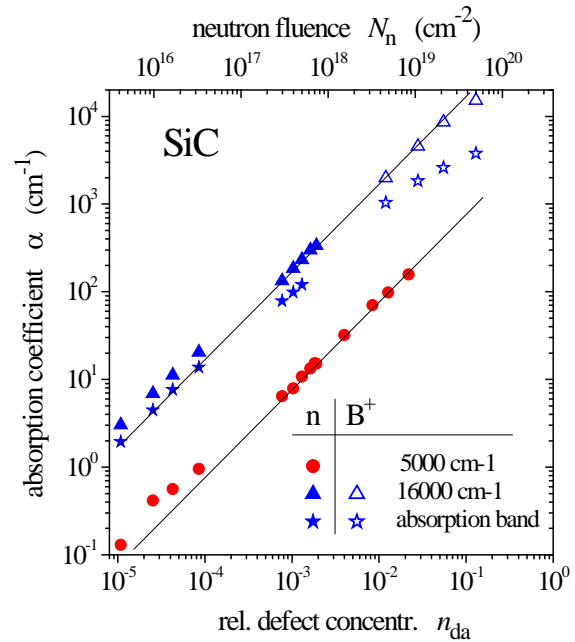


**Fig. 3:** Absorption coefficient  $\alpha$  versus the relative defect concentration  $n_{da}$  for neutron and  $\text{B}^+$  irradiated SiC. For comparison the upper abscissa gives the neutron fluences  $N_n$ .  $\alpha$  is plotted for wave numbers  $\nu = 5000 \text{ cm}^{-1}$  and  $16000 \text{ cm}^{-1}$ . Additionally the absorption in the maximum of the absorption band is shown after subtracting the background absorption. The lines indicate linear dependencies.

## References

- [1] E. Wendler, Th. Bierschenk, F. Felgenträger, J. Sommerfeld, W. Wesch, D. Alber, G. Bukalis, L.C. Prinsloo, N. van der Berg, E. Friedland, J.B. Malherbe, Nucl. Instrum. and Meth. B 2012, in press.
- [2] M. Okada, K. Atobe, M. Nakagawa, S. Kannazawa, I. Kanno, I. Kimura, Nucl. Instrum. and Methods B 166-167 (2000) 399.
- [3] G. Brauer, W. Anwand, P.G. Coleman, A.P. Knights, F. Plazaola, Y. Pacaud, W. Skorupa, J. Störmer, P. Willutzki, Phys. Rev. B 54 (1996) 3084.
- [4] Y. Liu, G. Wang, S. Wang, J. Yang, L. Chen, X. Qin, B. Song, B. Wang, X. Chen, Phys. Rev. Lett. 106 (2011) 087205.
- [5] S. Sorieul, J.-M. Costantini, L. Gosmain, G. Calas, L. Thomé, J. Phys. Condens. Materr 18 (2006) 8493.

### 3. Technical reports and equipment

#### Operation of the Ion-accelerator JULIA and the Ion-implanter ROMEO

U. Barth, F. Jehn, G. Lenk, W. Wesch, C. Ronning

The 3 MV high current tandemron accelerator **JULIA** (Jena University Laboratory for Ion Acceleration) went in operation end of 1996. Since the beginning of the routine-operation in 1997 it has been used for different types of experiments requiring a broad spectrum of ion-beams. With the exception of helium, where the duoplasmatron ion-source followed by a lithium exchange channel was used, all ions were extracted from a sputter-type ion-source. The beam-on-target-time of 1356 h was about 10% higher than in 2010. The 400 kV ion-accelerator **ROMEO** is in routine operation since 1998, here the beam-on-target-time of 1190 h was in the same order of magnitude as in the preceding years.

Both accelerators can be operated separately or in combination. The ion-beams produced until 2011 are summarized in table 1. The ion-beam currents quoted are typical values of the ion source currents used for the experiments, the maximum currents available are significantly higher for most ions.

Period	Element	Julia	Romeo
1	Hydrogen (H)	5 $\mu$ A	4 $\mu$ A
	Helium (He)	0,2 $\mu$ A	4 $\mu$ A
2	Lithium (Li)	2 $\mu$ A	1 $\mu$ A
	Boron (B)	0,2 $\mu$ A	5 $\mu$ A
	Carbon (C)	9 $\mu$ A	1 $\mu$ A
	Nitrogen (N)	10 $\mu$ A	4 $\mu$ A
	Oxygen (O)	17 $\mu$ A	2 $\mu$ A
	Flourine (F)	-	2 $\mu$ A
	Neon (Ne)	-	5 $\mu$ A
3	Sodium (Na)	-	6 $\mu$ A
	Magnesium (Mg)	-	5 $\mu$ A
	Aluminium (Al)	-	4 $\mu$ A
	Silicon (Si)	16 $\mu$ A	4 $\mu$ A
	Phosphorus (P)	-	4 $\mu$ A
	Chlorine (Cl)	-	2 $\mu$ A
	Argon (Ar)	-	20 $\mu$ A

**Table 1:** Ion-beams accelerated during 2011. The currents given are measured at the Q-Snout-Faradaycup after the low-energy mass separator (JULIA) and at the target position (ROMEO), respectively.

Period	Element	Julia	Romeo	
4	Potassium (K)	-	3 $\mu$ A	
	Calcium (Ca)	-	5 $\mu$ A	
	Titanium (Ti)	0,7 $\mu$ A	-	
	Vanadium (V)	0,2 $\mu$ A	1 $\mu$ A	
	Manganese (Mn)	0,017 $\mu$ A	5 $\mu$ A	
	Chromium (Cr)	0,2 $\mu$ A	3 $\mu$ A	
	Iron (Fe)	0,8 $\mu$ A	2 $\mu$ A	
	Cobalt (Co)	-	3 $\mu$ A	
	Nickel (Ni)	-	6 $\mu$ A	
	Copper (Cu)	0,5 $\mu$ A	-	
	Zinc (Zn)	1 $\mu$ A	6 $\mu$ A	
	Gallium (Ga)	1 $\mu$ A	3 $\mu$ A	
	Germanium (Ge)	1,6 $\mu$ A	4 $\mu$ A	
	Arsenic (As)	0,4 $\mu$ A	1 $\mu$ A	
	Selenium (Se)	0,5 $\mu$ A	1,5 $\mu$ A	
	Bromine (Br)	19 $\mu$ A	8 $\mu$ A	
	Krypton (Kr)	-	10 $\mu$ A	
	5	Rubidium (Rb)	0,075 $\mu$ A	1 $\mu$ A
		Strontium (Sr)	-	3 $\mu$ A
Yttrium (Y)		-	4 $\mu$ A	
Zirconium (Zr)		0,3 $\mu$ A	1,5 $\mu$ A	
Rhodium (Rh)		0,2 $\mu$ A	-	
Palladium (Pd)		0,095 $\mu$ A	1 $\mu$ A	
Silver (Ag)		1,6 $\mu$ A	10 $\mu$ A	
Cadmium (Cd)		-	0,8 $\mu$ A	
Indium (In)		5 $\mu$ A	8 $\mu$ A	
Tin (Sn)		-	3 $\mu$ A	
Antimony (Sb)		0,6 $\mu$ A	4 $\mu$ A	
Tellurium (Te)		-	2 $\mu$ A	
Iodine (I)		3 $\mu$ A	-	
Xenon (Xe)		-	10 $\mu$ A	
6	Caesium (Cs)	-	4 $\mu$ A	
	Barium (Ba)	-	1 $\mu$ A	
	Praseodymium (Pr)	-	1 $\mu$ A	
	Neodymium (Nd)	-	0,5 $\mu$ A	
	Samarium (Sm)	0,01 $\mu$ A	1,5 $\mu$ A	
	Europium (Eu)	0,035 $\mu$ A	2 $\mu$ A	
	Gadolinium (Gd)	0,03 $\mu$ A	-	
	Terbium (Tb)	-	3 $\mu$ A	
	Erbium (Er)	0,04 $\mu$ A	2 $\mu$ A	
	Tantalum (Ta)	0,2 $\mu$ A	2 $\mu$ A	
	Tungsten (W)	0,3 $\mu$ A	0,01 $\mu$ A	
	Osmium (Os)	0,05 $\mu$ A	-	
	Iridium (Ir)	0,3 $\mu$ A	6 $\mu$ A	
	Platinum (Pt)	0,2 $\mu$ A	-	
	Gold (Au)	24 $\mu$ A	20 $\mu$ A	
	Lead (Pb)	0,035 $\mu$ A	15 $\mu$ A	
	Bismuth (Bi)	-	3 $\mu$ A	

As in the preceding years the ion-beam facility was used by external research groups:

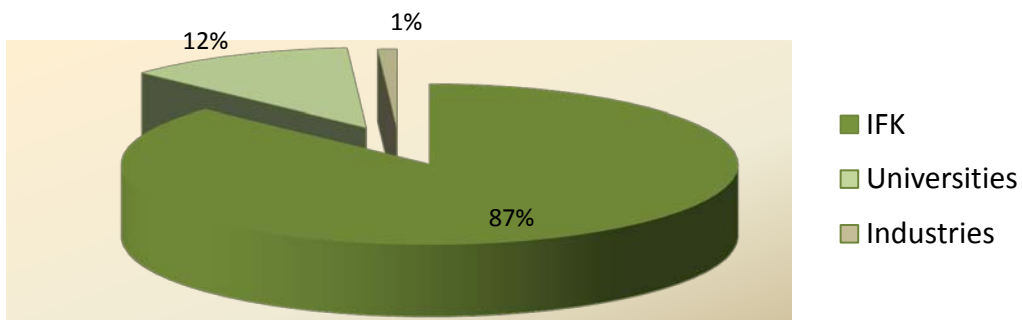
### 3MV-Tandetron „JULIA”

University Jena  
 IPHT Jena (Dr. Diegel)  
 ITN Lissabon (Dr. Lorenz)  
 University of Oslo (Dr. Azorov)  
 Firma Layertec (Herr Heyer)

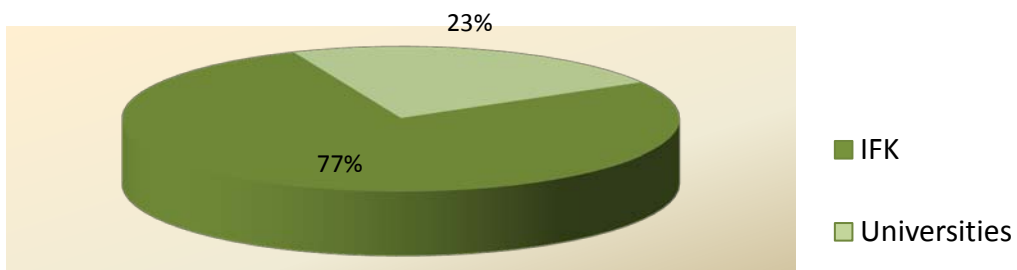
### 400kV Implanter „ROMEO“

University Jena  
 University of Pretoria (Prof. Malherbe)  
 University of Pretoria (Prof. Friedland)  
 University Minsk (Prof. Kamerow)  
 ITN Lissabon (Dr. Lorenz)  
 University of Oslo (Dr. Azorov)

### 3 MeV-Tandetron "JULIA"



### 400 kV Implanter "ROMEO"





## Cryogenic Services (TTS) 2011

All in-house customers of cryogenic liquids, which are all faculties of natural sciences, the university medical division including several hospitals, and other external scientific institutes (e.g. Institute for Photonic Technology Jena, Leibnitz Institute Hans-Knöll Jena) as well as some private customers like the Innovent e.V. Jena and some medical practices, were provided with liquid helium (LHe), high purity gases (He, N<sub>2</sub>) and with liquid nitrogen (LN<sub>2</sub>) by the Cryogenic Services. Roughly 118,000 litres of LN<sub>2</sub> were delivered by the cryogenic services in 2011. The distinct increase is a result of the stable operation of the new LN<sub>2</sub>-storage that delivered cryogenic gases for the IAAC-institute at the “Steiger”-site, which reached a stable operation mode for the first time ever.

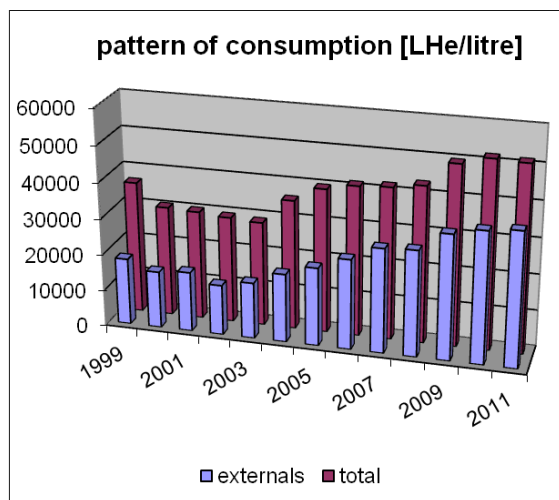


Fig. 1: Liquid helium output

As illustrated in Figure 1, the production of liquid helium (LHe) has levelled off in the recent three years. Roughly 45,000 litres of LHe were delivered in 2011 which calls for an annual gross refrigeration value of 51,500 litres.

In the period under report our focus had been on stabilizing the ongoing helium

liquefaction by performance-enhancing some circumferential sub-processes, most important the reconstruction of the whole high-pressure piping network of the TTS including a new gas management unit (Fig.2). Due to German legal requirements the old one had been licensed merely with a special continuation permit up to a pressure level of 150 bar. Therefore the storage capacity of the existing 200 bar high-pressure vessels had been restricted down to three-fourths of their real storage capacity too. Above all the equipment had been operated in a state of non-compliance to the actual legal requirements of the work safety. We acknowledge gratefully the financial backing of the task by the Technical Administration of the University with an amount of about 114,000 €

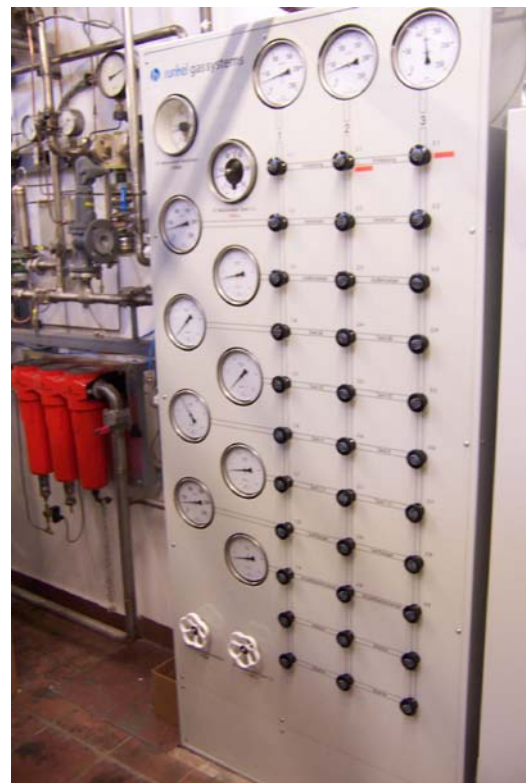


Fig. 2: Central gas management and control unit

During the whole reconstruction period the staff had managed ongoing refrigeration operations without any breakdown of the LHe-delivery.

## Equipment

### Preparation of thin films and devices

- HV evaporation facilities for thermal and electron beam evaporation and rf-sputtering with oxidation system
- UHV evaporation facilities, including electron gun and in situ RHEED system
- Equipment for laser deposition of thin crystalline films and material systems, especially high temperature superconductors (KrF excimer laser,  $\lambda = 248$  nm)
- Molecular Beam Epitaxy (MBE) facilities: MBE for silicon carbide (RIBER EVA 32 R&D)
- Organic Molecular Beam Epitaxy (OMBE) facilities including surface analysis techniques (MCP-LEED, UHV STM/AFM, RHEED) and *in situ* optical spectroscopy (PL and DRS)
- dc and rf sputtering systems for metallic (Au, Ti) and oxidic (SiO<sub>2</sub>, Ta<sub>2</sub>O<sub>5</sub>) thin films and multilayers
- Ion beam etching with Ar ions at sample temperatures down to 80 K in vacuum
- Chamber for ion- and reactive etching up to 4" wafer
- Reactive ion beam etching with sample diameters up to 6 cm
- Ultrasonic wire bonder
- Equipment for photolithographic patterning
- MBE system NEBULA for Cu(In,Ga)S<sub>2</sub> layers on 4" substrates including RHEED setup
- Two HV systems for closed-space sublimation (CSS) for deposition of CdTe layers
- RF reactive sputtering system for transparent conducting oxides (TCO's) and molybdenum
- DC sputtering system for copper and indium
- UHV system ULS400 for Cu(In,Ga)(Se,S)<sub>2</sub> on (100x100) mm<sup>2</sup> substrates
- Wet chemical processing and chemical bath deposition of photoactive layers

### Surface analysis systems

- AUGER electron spectrometer
- Surface analysis system UNISPEC with XPS, UPS, AES, LEED, STM
- Atomic force microscopes (AFM and Microstructure Measuring Device VERITEKT 3 with needle sensor)
- Surface profilometer DEKTAK 100
- Scanning electron microscopes
- Several UHV-scanning probe devices (STM, AFM)

### Electrical measurement techniques

- Electrical transport measurements (resistance, critical current density, point contact and tunneling spectroscopy)
- Hall-effect and Four-point probe equipment
- Current-voltage characteristics ( $2\text{ K} < T < 300\text{ K}$ ,  $B \leq 5\text{ T}$ )
- Current-voltage characteristics by microwave irradiation ( $2\text{ GHz} < f < 300\text{ GHz}$ )
- Noise measurements (frequency range  $60\ \mu\text{Hz} - 100\text{ kHz}$ ) at low temperatures
- LTS-SQUID characterization at 4.2 K (current-voltage, flux-voltage, noise, screening properties)
- HTS-SQUID characterization up to 100 K (current-voltage, flux-voltage, noise)

- 2 Deep level transient Fourier spectrometers (temperature range 80 K - 690 K, 30 K - 330 K)
- 3 Admittance spectrometers (frequency range 40 Hz - 100 kHz, 20 Hz - 1 MHz and 75 kHz - 30 MHz, temperature range 30 K - 690 K)
- Microwave signal generator (frequency range 1 - 20 GHz, resolution: 1 kHz)
- Electrical and optical characterization of high power diode laser arrays

### **Equipment for optical characterization**

- UV-VIS spectrometer
- FTIR spectrometer
- Cathodoluminescence at SEM, equipped for IR - UV
- Micro-Photoluminescence, IR-UV, time-resolution ~ 1 ns
- Photoluminescence excitation (PLE)
- Optical cryostats (2...300 K) for optical absorption, photoluminescence and Raman spectroscopy
- Excitation lasers in a wide range from 405-1550 nm (fiber, gas, solid state and diode lasers)
- Optical microscopes
- Magnetrelaxation of ferrofluids (MORFF) for characterization of magnetic nanoparticles

### **Equipment for electro-optical (solar) characterization**

- Solar simulator (AM 1.5) with Current-Voltage measurement
- Illuminated Current-Voltage measurements for 10 K to RT
- Quantum efficiency (EQE) measurements of solar cells

### **Equipment for thermal treatment**

- Furnace for conventional thermal treatment in inert gas atmosphere or vacuum (temperatures up to 2050 K)
- RTA apparatus (double graphite strip heater) for short time annealing (annealing time in the order of seconds, temperature range 1000 K to 1950 K, temperature rise rate 100 K s<sup>-1</sup>)

### **Elektron microscopy**

- Scanning electron microscope JEOL JSM-6490 with LaB<sub>6</sub>-cathode
- FEI field-emission electron microscope connected with FIB system

### **Ion beam techniques**

#### 3 MV Tandem accelerator "JULIA", equipped with

- Sputter ion source and Duoplasmatron source
- Universal beam line for ion implantation and ion beam analysis
- Second beam line for ion beam analysis, combined with implantation chamber of 400 kV implanter
- Irradiation chamber with cooled and heated sample holder and four axis goniometer

#### *Application:*

- Ion implantation: energy range 500 keV - 12 MeV, temperature range 15 K - 1500 K
- Ion beam analysis: RBS and PIXE in combination with channeling, ERDA

400 kV implanter “ROMEO”, equipped with

- Hot filament, hollow cathode ion source
- Irradiation chamber with cooled and heated sample holder and four axis goniometer, combined with beam line of 3 MV Tandatron accelerator

*Application:*

- Ion implantation: energy range 20 keV - 400 keV, temperature range 15 K - 1500 K
- Ion implantation at low temperatures and subsequent RBS analysis using H- or He-ions from 3 MV Tandatron accelerator

Low Energy implanter “LEILA”, equipped with

- Colutron Ion source 100-Q
- Colutron Ion Gun System G-2-D
- Irradiation chamber with heated sample holder

*Application:*

- Irradiation of surfaces: energy range sub-keV, temperature range 300 K - 750 K

Low Energy implanter “Mr. JIM Stringer”, equipped with

- Hot filament, hollow cathode ion source
- Irradiation and deposition chamber

*Application:*

- Deposition of diamond-like thin films: energy range 100eV – 30 keV, RT

Focused Ion Beam system FEI NanoLab Helios 600i

- Liquid ion source, E = 500 eV – 30 keV
- Electron microscope, E = 350 eV – 30 keV

*Application:*

- TEM-lamella preparation, etc.

**Low temperature measuring equipment**

- He-4 cryostats for temperatures down to 4.2 K
- He-4 refrigerator for the temperature range 1.3 K - 4.2 K
- He-3 cryostat for temperatures down to 300 mK
- He-3/He-4 dilution refrigerator with a base temperature of 35 mK
- He-3/He-4 dilution refrigerator with a base temperature of 7 mK
- Electronic equipment for characterization of cryoelectronic devices
- SQUID sensor systems for magnetic measurements under unshielded conditions
- SQUID sensor system for spatially resolved magnetorelaxometry
- Cryostats ( $2\text{ K} < T < 300\text{ K}$ ; optical window; magnetic field)
- Cryocoolers (Gifford-McMahon and Stirling)
- Pulse tube refrigerators (for sensor cooling)

### **SQUID application laboratories**

- Measurement system for non-destructive evaluation in unshielded environment based on high- $T_C$ -SQUID gradiometers
- Heart monitoring system for biomagnetic investigation in unshielded environment based on high- $T_C$ -SQUID gradiometers
- High precision position detection system based on low- $T_C$ -SQUIDS
- Magnet-Relaxation-Measuring System in unshielded environment for MRX and TMRX based on low- $T_C$  SQUID gradiometers

### **Clean room (number of particles/cu/t < 100)**

- Photolithography
- Wet chemical etching
- dry chemical etching (Plasma etching machine “pico”, Diener Plasma)
- minimum lateral resolution: few micrometers

### **Shielded rooms**

- Faraday room
- Magnetic shielded room

### **Laboratory for cryogenic measurement of mechanical quality factors of gravitational wave detector components**

- room temperature stability of  $\pm 0.2$  K at best
- vibration isolation (decoupled foundation)
- acoustic isolation
- remote controlled operation of the measurement equipment
- separated room for disturbing machines (e.g. pumps)
- full supply of technical media to perform cryogenic measurements

### **Laboratory for astrophysics and cluster physics**

- Supersonic jet apparatus for gas-phase spectroscopy of large molecules
- Matrix isolation UV/vis spectroscopy setup with closed-cycle cryostat
- Helium droplet apparatus for spectroscopy and reaction studies at ultra-low temperature
- Flow reactors for the production of silicon-, carbon-, and iron-based nanoparticles
- Cluster beam apparatus with laser pyrolysis source and size selection facility
- Time-of-flight mass spectrometer (TOF-MS)
- Quadrupole mass spectrometer
- Photoluminescence spectrometer for UV/vis and near IR emission wavelengths
- Atomic force microscope (AFM)
- High-pressure liquid chromatograph (HPLC)
- Pulsed and cw CO<sub>2</sub> lasers
- Single-mode Nd:YAG lasers with tunable dye lasers and frequency doubling facilities
- ArF excimer laser

## 4. Current research projects

**(A) Supported by the Bundesministerium für Bildung, Wissenschaft, Forschung und Technologie (BMBF), Bundesministerium für Wirtschaft und Arbeit (BMWi), and Bundesministerium für Umwelt, Naturschutz und Reaktorsicherheit (BMU)**

*Ioneninduzierte Strukturumbildungsprozesse in amorphen Halbleitern*

Teilprojekt 4 im Verbundprojekt „Ioneninduzierte Strukturumbildung“

Verbund Forschung mit Sonden und Ionenstrahlen im Gesamtverbund Erforschung der kondensierten Materie mit Großgeräten

Prof. Dr. W. Wesch 05K10SJ1 07/10 – 06/13

*Verbundprojekt: Computational Materials Science gestützte Optimierung des Wirkungsgrades von CIGS-Dünnschichtsolarzellen*

Prof. Dr. W. Wesch 0327665E 07/07 – 09/11

*CdTe-CdS-Solarzellen hoher Effizienz für eine verbesserte Modul-Produktionstechnologie*

Prof. Dr. W. Wesch 0329881A 09/08 – 04/13

*Strahlenschädenbildung und Diffusion energetischer Teilchen in SiC*

Dr. E. Wendler SUA 08/028 03/09 – 12/11

*Forschungsprämie*

Prof. Dr. C. Ronning 03FPB00384 04/10 – 03/11

*Toxikologische Charakterisierung von Nanomaterialien für die diagnostische Bildgebung in der Medizin – NanoMed*

Prof. Dr. P. Seidel BMBF (Ausschreibung NanoCare) 09/10 – 08/13

*Spitzenforschung und Innovation in den Neuen Ländern – Photonische Nanomaterialien*

Prof. Dr. C. Ronning PhoNa 12/09 – 11/14

*Josephsonkontakte mit variablem Durchlassvermögen*

Prof. Dr. P. Seidel BMBF (WTZ UKR 10/034) 06/11 – 05/13

**(B) Supported by the Deutsche Forschungsgemeinschaft (DFG)**

*Formation of GEMS from interstellar silicate dust*

Prof. Dr. Fr. Huisken HU 474/23-1 02/10 – 01/12

*Spektroskopische Untersuchungen an polyzyklischen aromatischen Kohlenwasserstoffen mit aliphatischen Seitengruppen*

Prof. Dr. Fr. Huisken HU 474/24-1 02/10 – 01/12

*Synthesis, processing, and spectroscopic characterization of PAHs with astrophysical impact*

Prof. Dr. Fr. Huisken HU 474/21-2 07/10 – 12/12

*Messung von Gütefaktoren bei kryogenen Temperaturen*

(Teilprojekt C4 im SFB/TR 7 „Gravitationswellenastronomie“ gemeinsam mit IAP der FSU)

Prof. Dr. P. Seidel, Dr. R. Nawrodt	DFG-SFB/TR7/C4	01/11 – 12/14
<i>Optische Eigenschaften siliziumbasierter Testmassen</i> (Teilprojekt C9 im SFB/TR 7 „Gravitationswellenastronomie“ gemeinsam mit Uni Hannover)		
Dr. R. Nawrodt	DFG-SFB/TR7	01/11 – 12/14
<i>Josephson effects at iron pnictides</i>		
Prof. Dr. P. Seidel	DFG (SPP 1458) SE 664/15-1	05/10 – 04/13
<i>Formation and Shaping of Magnetic Nano-clusters in Ion Implanted Oxides</i>		
Prof. Dr. C. Ronning	Ro1198/13-1	03/11 – 02/14
<i>Wiring quantum dots – phase separation inducing new functionality (D-A-CH)</i>		
Prof. Dr. C. Ronning	Ro1198/14-1	08/11 – 07/14
<i>Rastertunnelspektroskopie an einzelnen Molekülen in epitaktischen Nanoschichten</i>		
Prof. Dr. T. Fritz	FR 875/11	10/09 – 12/12
<i>Strukturierungsverfahren für mikro- und nanooptische Elemente in Lithiumniobat</i>		
Dr. E.-B. Kley, Prof. Dr. W. Wesch	KL1199/2-2	05/10 – 12/12

**(C) Support by the EU**

<i>Marie-Curie ITN network “Nanowiring”</i>		
Prof. Dr. C. Ronning	265073	11/10 – 10/14
<i>Marie Curie Intra-European Fellowship “Spectroscopy of cosmic dust analogs: Study of the interaction with polycyclic aromatic hydrocarbons (PAHCNP)”</i>		
Prof. Dr. Fr. Huisken	274794	10/11 – 09/13
<i>Marie-Curie ITN network “Laboratory Astrochemical Surface Science in Europe (LASSIE)”</i>		
Dr. C. Jäger	238258	02/10 – 01/14
<i>IRON-SEA - Establishing the basic science and technology for Iron-based superconducting electronics applications</i>		
Prof. Dr. P. Seidel	283141	10/11 – 09/14

**(D) Supported by the Thüringer Ministerium für Bildung, Wissenschaft und Kultur (TKBWK)**

<i>Optische und strukturelle Untersuchung ultradünner molekularer Schichten</i>		
Prof. Dr. T. Fritz	B 515-10030	09/10 – 12/11
<i>Ionenstrahlmodifikation und -analyse von Titanoberflächen</i>		
Prof. Dr. W. Wesch	02/9125 IBA Heiligenstadt	05/02 – 12/12





## 5. Publications, invited talks, and conference contributions

### 5.1 Publications in scientific journals

*Defect induced changes on the excitation-transfer dynamics in ZnS:Mn nanowires*

U. Kaiser, L. Chen, S. Geburt, C. Ronning, W. Heimbrodt  
Nanoscale Research Letters **6**, 228 (2011)

*Composition and texture of barium silicate crystals in fresnoite glass-ceramics by various scanning electron microscopic techniques*

M. Nagel, W. Wisniewski, G. Völksch, C. Borschel, C. Ronning, C. Rüssel  
CrysEngComm **13**, 3383 (2011)

*Hexagonal boron nitride nanowalls synthesized by unbalanced magnetron sputtering*

B. BenMoussa, J. D'Haen, C. Borschel, M. Saitner., Ali Soltani, V. Mortet, C. Ronning, M. D'Olieslaeger, H.-G. Boyen, K. Haenen  
MRS online Proceeding Library **1307**, mrsf10-cc06-09 (2011)

*Permanent bending and alignment of ZnO nanowires*

C. Borschel, S. Spindler, D. Lerose, A. Bochmann, S.H. Christiansen, S. Nietzsche, M. Oertel and C. Ronning  
Nanotechnology **22**, 185307 (2011)

*Temperature-dependent photoconductance of heavily doped ZnO nanowires*

D. Li, L. Zhao, R. Wu, C. Ronning, J.G. Lu  
Nano Research **4**, 1110 (2011)

*Synchrotron fluorescence nanoimaging of a single Co-implanted ZnO nanowires*

M.H. Chu, J. Segura-Ruiz, G. Martinez-Criado, P. Cloetens, I Snigireva, S. Geburt, C. Ronning  
physica status solidi RRL **5**, 283 (2011)

*Ion Beam Irradiation of Nanostructures - A 3D Monte Carlo Simulation Code*

C. Borschel, C. Ronning  
Nuclear Instruments & Methods B **269**, 2133 (2011)

*Biofunctionalization of zinc oxide nanowires for DNA sensory applications*

R. Niepelt, U.C. Schröder, J. Sommerfeld, I. Slowik, B. Rudolph, R. Möller, B. Seise, A. Csaki, W. Fritzsche, C. Ronning  
Nanoscale Research Letters **6**, 511 (2011)

*A new route toward semiconductor nanospintronics: highly Mn-doped GaAs nanowires realized by ion-implantation under dynamic annealing conditions*

C. Borschel, M.E. Messing, M. T. Borgstrom, W. Paschoal Jr, J. Wallentin, S. Kumar, K. Mergenthaler, K. Deppert, C. M. Canali, H. Pettersson, L. Samuelson, and C. Ronning  
Nano Letters **11**, 3935 (2011)

*Magneto-electronic properties of Gd-implanted tetrahedral amorphous carbon*

Li Zeng, H. Zutz, F. Hellman, E. Helgren, J.W. Ager III, C. Ronning  
Physical Review B **84**, 134419 (2011)

*Strong Molecular Fluorescence inside a Nanoscale Waveguide Gap*

V. Sorger, O. Pholchai, E. Cubukcu, R. Oulton, P. Kolchin, C. Borschel, M. Gnauck, C. Ronning, X. Zhang  
Nano Letters **11**, 4907 (2011)

*Nano-X-ray Absorption Spectroscopy of Single Co Implanted ZnO Nanowires*

J. Segura-Ruiz, G. Martínez-Criado, M.H. Chu, S. Geburt, C. Ronning  
Nano Letters **11**, 5322 (2011)

*Determination of secondary ion mass spectrometry relative sensitivity factors for polar and non-polar ZnO*

A. Laufer, N. Volbers, S. Eisermann, K. Potzger, S. Geburt, C. Ronning, B.K. Meyer  
Journal of Applied Physics **110**, 094906 (2011)

*Persistent Ion Beam Induced Conductivity in Zinc Oxide Nanowires*

A. Johannes, R. Niepelt, M. Gnauck, C. Ronning  
Applied Physics Letters **99**, 252105 (2011)

*Increased homogeneity and open-circuit voltage of Cu(In,Ga)Se<sub>2</sub> solar cells due to higher deposition temperature*

J. Haarstrich, H. Metzner, M. Oertel, C. Ronning, T. Rissom, C.A. Kaufmann, T. Unhold, H.W. Schock, J. Windeln, W. Mannstadt, and E. Rudigier-Voigt  
Solar Energy Materials and Solar Cells **95**, 1028 (2011)

*Modelling the Quantum Efficiency of cadmium telluride Solar Cells*

M. Hädrich, H. Metzner, U. Reislöhner, and C. Kraft  
Solar Energy Materials and Solar Cells **95**, 887 (2011)

*Back contact formation in thin cadmium telluride solar cells*

M. Hädrich, C. Heisler, U. Reislöhner, C. Kraft, and H. Metzner  
Thin Solid Films **519**, 7156 (2011)

*Near-interface doping by ion implantation in Cu(In,Ga)Se<sub>2</sub> solar cells*

J. Haarstrich, H. Metzner, C. Ronning, T. Rissom, C.A. Kaufmann, H.W. Schock, W. Mannstadt, E. Rudigier-Voigt, and V. Scheumann  
Thin Solid Films **519**, 7276 (2011)

*Investigation of the excitonic luminescence band of CdTe solar cells by photoluminescence and photoluminescence excitation spectroscopy*

C. Kraft, M. Hädrich, H. Metzner, U. Reislöhner, P. Schley, and R. Goldhahn  
Thin Solid Films **519**, 7173 (2011)

*Electroless Silver Plating of the Surface of Organic Semiconductors*

M. Campione, M. Parravicini, M. Moret, A. Papagni, B. Schroeter, T. Fritz  
Langmuir **27**, 12008 (2011)

*Influence of electronic energy deposition on the structural modification of swift heavy-ion-irradiated amorphous germanium layers*

T. Steinbach, C.S. Schnohr, P. Kluth, R. Giulian, L.L. Araujo, D.J. Sprouster, M.C. Ridgway, W. Wesch  
Phys. Rev. B **83**, 054113 (2011)

*Investigation of silver and iodine transport through silicon carbide layers prepared for nuclear fuel element cladding*

Friedland, N.G. van den Berg, J.B. Malherbe, J.J. Hancke, J. Barry, E. Wendler, W. Wesch  
J. of Nuclear Materials **410**, 24 (2011)

*Ion-beam-induced damage formation in CdTe*

C.W. Rischau, C.S. Schnohr, E. Wendler, W. Wesch  
J. Appl. Phys. **109**, 113531 (2011)

*Void formation in amorphous germanium due to high electronic energy deposition*

K. Gärtner, J. Jöhrens, T. Steinbach, C.S. Schnohr, M.C. Ridgway, W. Wesch  
Phys. Rev. B **83**, 224106 (2011)

*Structure and optical properties of silicon layers with GaSb nanocrystals created by ion beam synthesis*

F. Komarov, L. Vlasukova, O. Milchanin, A. Mudryi, B.S. Dunetz, W. Wesch, E. Wendler, C. Karwat  
Acta Physica Polonica A **120**, 87 (2011)

*Structural modifications of low-energy heavy-ion irradiated germanium*

T. Steinbach, J. Wernecke, P. Kluth, M.C. Ridgway, W. Wesch  
Phys. Rev. B **84**, 104108 (2011)

*Phosphorus implanted cadmium telluride solar cells*

C. Kraft, A. Brömel, S. Schönherr, M. Hädrich, U. Reislöhner, P. Schley, G. Gobsch, R. Goldhahn, W. Wesch, and H. Metzner  
Thin Solid Films **519**, 7153 (2011)

*Measurement of the zinc oxide - molybdenum specific contact resistance for applications in CIGS-technology*

M. Oertel, S. Goetz, J. Cieslak, J. Haarstrich, H. Metzner, W. Wesch  
Thin Solid Films **519**, 7545 (2011)

*Effects of annealing regimes on the structural and optical properties of InAs and GaSb nanocrystals created by ion-beam synthesis in Si matrix*

Fadei F. Komarov, Ludmila A. Vlasukova, Oleg V. Milchanin, Mikel V. Greben, Alexander V. Mudryi, W. Wesch  
Proceedings 1st Int Conf. on Nanomaterials: Applications and Properties (NAP-2011), Alushta, Ukraine, Sept. 27-30, 2011; Vol. 1, Part II, p.409.

*Rainbow scattering under axial surface channeling from a KCl(001) surface*

U. Specht, M. Busch, J. Seifert, A. Schüller, H. Winter, K. Gärtner, R. Włodarczyk, M. Sierka, J. Sauer  
Phys. Rev. B **84**, 125440 (2011)

*Classical and quantum mechanical rainbow-scattering of fast He atoms from a KCl(001) surface*

U. Specht, M. Busch, J. Seifert, H. Winter, K. Gärtner, R. Włodarczyk, M. Sierka, J. Sauer  
Nucl. Instr. & Methods B **269**, 799 (2011)

*Transition from axial to planar surface channeling for fast atom diffraction*

J. Seifert, A. Schüller, H. Winter, K. Gärtner  
Nucl. Instr. & Methods B **269**, 1212 (2011)

*Magnetorelaxation (MRX) measurements with DC-SQUID gradiometers*

M. Büttner, F. Schmidl, M. Schiffler, P. Seidel  
IEEE Trans. Appl. Supercond. **21**, 473 (2011)

*A non-destructive beam monitoring system based on an LTS-SQUID*

R. Geithner, R. Neubert, W. Vodel, M. Schwickert, H. Reeg, R. von Hahn, P. Seidel  
IEEE Trans. Appl. Supercond. **21**, 444 (2011)

*Investigation of magnetic active core sizes and hydrodynamic diameters of a magnetically fractionated ferrofluid*

M. Büttner, P. Weber, F. Schmidl, P. Seidel, M. Röder, M. Schnabelrauch, K. Wagner, P. Görnert,

G. Glöckl, W. Weitschies  
Journal of Nanoparticle Research **13**, 165 (2011)

*Dark current measurements on a superconducting cavity using a cryogenic current comparator*  
R. Geitner, R. Neubert, W. Vodel, P. Seidel, K. Knaack, K. Wittenburg, O. Kugeler  
Rev. Sci. Instruments **82**, 013302 (2011)

*Neue supraleitende Materialien*  
P. Seidel  
Deutscher Kälte- und Klimatechnischer Verein e.V. (DKV), (2011) AA I.16 (8 Seiten)

*Josephson junctions*  
P. Seidel  
Buchkapitel in "High Temperature Superconductors", Ed. X. G. Qiu, Woodhead Publishing Ltd., Cambridge, U.K., 2011

*Josephson effects in iron based superconductors (Invited topical review)*  
P. Seidel  
Supercond. Sci. Technol. **24**, 043001 (2011)

*The Influence of the Resonator on the Self Heating Effect and the Synchronization of Josephson Junctions*  
A. Grib, P. Seidel  
IEEE/CSC & ESAS EUROPEAN SUPERCONDUCTIVITY NEWS FORUM (ESNF), **16**, April 2011

*Resonance Features of Coupled Josephson Junctions in High Temperature Superconductors*  
Y. Shukrinov, P. Seidel  
IEEE/CSC & ESAS EUROPEAN SUPERCONDUCTIVITY NEWS FORUM (ESNF), **16**, April 2011

*Engineering of  $YBa_2Cu_3O_{7-\delta}$  grain boundary Josephson junctions by Au nanocrystals*  
P. Michalowski, M. Schmidt, F. Schmidl, V. Grosse, D. Kuhwald, C. Katzer, U. Hübner and P. Seidel  
Physica Status Solidi (RRL) **5**, 268 (2011)

*Resonance features of coupled Josephson junctions in high temperature superconductors*  
Y. Shukrinov, P. Seidel  
Elektronika **6**, 52 (2011)

*The influence of the resonator on the self heating effect and the synchronization of Josephson junctions*  
A. Grib, P. Seidel  
Elektronika **6**, 26 (2011)

*Increased flux pinning in  $YBa_2Cu_3O_{7-\delta}$  thin-film devices through embedding of Au nano crystals*  
C. Katzer, M. Schmidt, P. Michalowski, D. Kuhwald, F. Schmidl, V. Grosse, S. Treiber,  
C. Stahl, J. Albrecht, U. Hübner, A. Undisz, M. Rettenmayr, G. Schütz, P. Seidel  
EPL **95**, 68005 (2011)

*Optical resonances of self-organized monocrystalline Au nanoparticles embedded in  $SrTiO_3$  matrix*  
S. Christke, C. Katzer, V. Grosse, F. Schmidl, G. Schmidl, W. Fritzsche, J. Petschulat, T. Pertsch, M. Rettenmayer  
Optical materials express **1**, 890 (2011)

*Challenges in thermal noise for 3rd generation of gravitational wave detectors*  
R. Nawrodt, S. Rowan, J. Hough, M. Punturo, F. Ricci, J.-Y. Vinet  
Gen. Relativ. Gravit. **43**, 593 (2011)

- Low-temperature strength tests and SEM imaging of hydroxide catalysis bonds in silicon*  
N. L. Beveridge, A. A. van Veggel, M. Hendry, P. Murray, R. A. Montgomery, E. Jesse, J. Scott, R. B. Bezensek, L. Cunningham, J. Hough, R. Nawrodt, S. Reid, S. Rowan,  
Class. Quantum Grav. **28**, 085014 (2011)
- Sensitivity studies for third-generation gravitational wave observatories*  
S. Hild et al. (D. Heinert, R. Nawrodt, C. Schwarz, P. Seidel)  
Class. Quantum Grav. **28**, 094013 (2011)
- Mechanical loss of calcium fluoride at cryogenic temperatures*  
Ch. Schwarz, D. Heinert, P. Seidel, A. Tünnermann, G. D. Hammond, R. Nawrodt  
Phys. Status Solidi A **208**, 2719 (2011)
- The effect of a laser beam displacement on parametric oscillatory instabilities for Advanced LIGO*  
D. Heinert, S.E. Stringin  
Physics Letters A **375**, 3804 (2011)
- Reduction of coating thermal noise by using an etalon*  
K. Somiya, A. G. Gurkovsky, D. Heinert, S. Hild, R. Nawrodt, S. P. Vyatchanin,  
Physics Letters A **375**, 1363 (2011)
- Thermorefractive noise of finite-sized cylindrical test masses*  
D. Heinert, A. G. Gurkovsky, R. Nawrodt, S. P. Vyatchanin. K. Yamamoto,  
Phys. Rev. D **84**, 062001 (2011)
- Reducing thermal noise in future gravitational wave detectors by employing Khalili etalons*  
A. G. Gurkovsky, D. Heinert, S. Hild, R. Nawrodt, K. Somiya, S. P. Vyatchanin, H. Wittel,  
Physics Letters A **375**, 4147 (2011)
- Cryogenic mechanical loss measurements of heat-treated hafnium dioxide*  
M. R. Abernathy, S. Reid, E. Chalkley, R. Bassiri, I.W. Martin, K. Evans, M.M. Fejer, A. Gretarsson,  
G. M. Harry, J. Hough, I. MacLaren, A. Markosyan, P. Murray, R. Nawrodt, S. Penn, R. Route,  
S. Rowan, P. Seidel  
Class. Quantum Grav. **28**, 195017 (2011)
- News about the Cryogenic Current Comparator for beam diagnostics*  
W. Vodel, R. Neubert, R. Geithner, P. Seidel, M. Schickert, H.Reeg, K. Knaack, K. Wittenburg,  
A. Peters  
Proceedings of DIPAC 2011, Hamburg, 569-571 (2011)
- Sensor optimizations for a Cryogenic Current Comparator*  
R. Geithner, W. Vodel, R. Neubert, P. Seidel, P. Kowina, F. Kurian, M. Schwickert, R. von Hahn  
Proceedings of DIPAC 2011, Hamburg, 458-460 (2011)
- Placenta perfusion – a suitable ex vivo model to characterise interaction of nano-particles with human tissue?*  
L. Seyfarth, U. Enke, R. Bräuer, N. Brendel, M. Büttner, A. Csaki, F. Schlenk, C. Bergemann, D. Fischer, W. Fritzsche, P. Seidel, E. Schleussner  
Placenta **32**, A1–A149 (2011)
- Search for Gravitational Wave Bursts from six magnetars*  
J. Abadie et al. (R. Nawrodt),  
ApJ **734**, L35 (2011)

*Search for gravitational waves from binary black hole inspiral, merger, and ringdown*

J. Abadie et al. (R. Nawrodt)  
Phys. Rev. D **83**, 122005 (2011)

*Beating the spin-down limit on gravitational wave emission from the vela pulsar*

J. Abadie et al. (R. Nawrodt)  
ApJ **737**, 93 (2011)

*Search for gravitational waves associated with the August 2006 timing glitch of the Vela pulsar*

J. Abadie et al. (R. Nawrodt)  
Phys. Rev. D **83**, 042001 (2011)

*A gravitational wave observatory operating beyond the quantum shot-noise limit*

J. Abadie et al. (R. Nawrodt)  
Nature Physics **7**, 962-965 (2011)

*Examination of magnetite nanoparticles utilising the temperature dependent magnetorelaxometry*

M. Büttner, P. Weber, C. Lang, M. Röder, D. Schüller, P. Görnert, P. Seidel  
J. of Magn. and Mag. Mater. **323**, 1179 (2011)

*Electronic spectroscopy of FUV-irradiated diamondoids: A combined experimental and theoretical study*

M. Steglich, F. Huisken, J. E. Dahl, R. M. K. Carlson, and Th. Henning  
Astrophys. J. **729**, 91-1-10 (2011)

*Can neutral and ionized PAHs be carriers of the UV extinction bump and the diffuse interstellar bands?*

M. Steglich, J. Bouwman, F. Huisken, and Th. Henning  
Astrophys. J. **742**, 2-1-12 (2011)

*Abundances of PAHs in the ISM: Confronting observations with experimental results*

R. Gredel, Y. Carpentier, G. Rouillé, M. Steglich, F. Huisken, and Th. Henning  
Astron. Astrophys **530**, A26-1-15 (2011)

*Determination of the photoluminescence quantum efficiency of silicon nanocrystals by laser-induced deflection*

K. Potrick, T. Schmidt, S. Bublitz, Chr. Mühlig, W. Paa, and F. Huisken  
Appl. Phys. Lett. **98**, 083111 (2011)

*Spectroscopy of dibenzorubicene: Experimental data for a search in interstellar spectra*

G. Rouillé, M. Steglich, C. Jäger, F. Huisken, Th. Henning, G. Theumer, I. Bauer, and H.-J. Knölker  
Chem. Phys. Chem. **12**, 2131 (2011)

*Dynamical effects of defect photoluminescence from single Si/SiO<sub>2</sub> and SiO<sub>2</sub> nanoparticles*

A. I. Chizhik, T. Schmidt, A. M. Chizhik, F. Huisken, and A. J. Meixner  
Phys. Procedia **13**, 28-32 (2011)

*From PAHs to solid carbon*

C. Jäger, H. Mutschke, Th. Henning, and F. Huisken  
in: PAHs and the Universe: A Symposium to Celebrate the 25th Anniversary of the PAH Hypothesis,  
edited by C. Joblin and A. G. G. M. Tielens  
EAS Publications Series **46**, 293-304 (2011)

*Absorption spectroscopy of astrophysically relevant molecules in supersonic jets*

F. Huisken, G. Rouillé, Y. Carpentier, M. Steglich, and Th. Henning

in: *Rarified Gas Dynamics, 27th International Symposium on Rarefied Gas Dynamics, RGD27*, edited by D. A. Levin, I. Wysong, and A. L. Garcia  
AIP Conference Proceedings **1333**, 819-824 (2011)

*Low-temperature chemistry in helium droplets: Reactions of Al atoms with O<sub>2</sub> and H<sub>2</sub>O*  
S. A. Krasnokutski and F. Huisken  
J. Phys. Chem. A **115**, 7120-7126 (2011)

*High-resolution electron spectroscopy, preferential metal-binding sites, and thermochemistry of lithium complexes of polycyclic aromatic hydrocarbons*  
J. S. Lee, S. A. Krasnokutski, and D. S. Yang  
J. Chem. Phys. **134**, 024301 (2011)

*Electronic states and spin-orbit splitting of lanthanum dimer*  
Y. Liu, L. Wu, C. H. Zhang, S. A. Krasnokutski, and D. S. Yang  
J. Chem. Phys. **135**, 034309 (2011)

*Ionic and vibrational properties of an ultra-low ionization potential molecule: Tetrakis (dimethylamino)ethylene*  
N. Mirsaleh-Kohan, W. D. Robertson, J. Lambert, R. N. Compton, S. A. Krasnokutski, and D. S. Yang  
Int. J. Mass Spectrom. **304**, 57 (2011)

*Dielectric effects on the optical properties of single silicon nanocrystals*  
N. El-Kork, F. Huisken, and Chr. von Borczyskowski  
J. Appl. Phys. **110**, 074312 (2011)

## 5.2 Invited talks and colloquia

C. Ronning

*Ion beam doping of semiconductor nanowires and their characterization using a X-Ray nano probe*

MRS fall meeting 2011, Boston, Session BB, 1.12.2011

*Ion beam doping of semiconductor nanowires*

Frühjahrstagung der DPG, Dresden – Section DS, 16.3.2011

*Semiconductor nanowires: synthesis, properties and doping*

U Hasselt, Belgien, IMO lecture, 20.06.2011

*Semiconductor nanowires for photonic applications*

TU Wien, SFB Seminar, 29.05.2011

*Ionenbestrahlung: neue Physik mit altem Prinzip*

Ehrenkolloquium zur Verabschiedung Prof. T. Butz, Universität Leipzig, 22.2.2011

T. Fritz

*Formation of Organic-on-Organic Heteroepitaxial Layers*

Collaborative Conference on 3D & Materials Research (3DMR), Jeju, South Korea, 30.06.2011

P. Seidel

*Josephson effects in iron based superconductors*

ESF Exploratory Workshop, Bad Schandau, May 23 – 25, 2011

*Films, junctions and electronic devices*

ISS 2011, Tokyo/Japan, October 24 – 26, 2011

W. Wesch

*Structural modification of amorphous silicon and germanium under swift heavy ion irradiation*

2011 International Workshop on Ion Beam Applications of Functional Materials, Jinan, China, August 19-22, 2011

W. Wesch, E. Wendler, C.S. Schnohr

*Amorphization kinetics in semiconductors under ion irradiation*

E-MRS 2011 Spring Meeting, Nice, France, 9.-13 Mai 2011

U. Reislöhner

*Electrical Characterization of Cu(In,Ga)(S,Se)<sub>2</sub>-Based Solar Cells at Low Temperatures*

Frühjahrstagung der DPG, Dresden – Section DS, 14. März 2011

C. Borschel

*Highly Mn-doped GaAs nanowires realized by ion-implantation with dynamic annealing*

4th NordForsk Nanospintronics Network meeting, Enköping (Sweden), 27.09.11

C.S. Schnohr

*Crystalline and amorphous semiconductors after high electronic energy deposition*

Subtherm 2011 - International Topical Workshop on Subsecond Thermal Processing of Advanced Materials, Dresden, Germany, October 24-26, 2011

Y. Shukrinov, P. Seidel

*Resonance features of coupled Josephson junctions in high temperature superconductors*

International Conference on Quantum Metrology 2011, Poznan/Poland, May 11 – 13, 2011



F. Huisken

*Optical properties of silicon-based nanomaterials: Ensemble and single particle spectroscopy of silicon nanocrystals and silicon oxide nanoparticles*

Invited Seminar, Korean Institute of Energy Research, University of Daejeon, South Korea, March 28, 2011

*Photoluminescence studies on size-selected silicon nanocrystals*

Invited Seminar, School of Materials Science and Engineering, University of Ulsan, South Korea, March 29, 2011

*Oxidative reactions of group IIA and IIIA elements in helium droplets*

Invited lecture, 482nd Wilhelm and Else Heraeus Seminar: Helium Nanodroplets – Confinement for Cold Molecules and Cold Chemistry, Bad Honnef, 30.05. – 01.06.2011

*Laboratory Experiments for the Interpretation of Astrophysical Phenomena*

Seminar des Sonderforschungsbereichs 956, I. Physikalisches Institut der Universität zu Köln, 7. November 2011

C. Jäger

*Formation of GEMS from interstellar silicate dust*

2nd Annual Meeting of the SPP 1385, Mainz, October 17–19, 2011

G. Rouillé

*Laboratory astrophysics in Jena: From spectroscopic characterization of large molecules and grains to low temperature chemistry*

NWO Astrochemistry Workshop: Molecular Networks Connecting the Universe, Amsterdam, The Netherlands, April 18 – 20, 2011

M. Steglich

*Electronic spectroscopy of neutral and ionized PAHs in inert gas matrices*

International Conference on Interstellar Dust, Molecules and Chemistry, Pune, India, 22. – 25.11.2011

### 5.3 Conference contributions

#### 471. WEH-Seminar "Functional Magnetoelectric Oxide Heterostructures", Bad Honnef, January 5-7, 2011

V. Grosse, F. Schmidl, P. Seidel  
*Current transport in epitaxially strained strontium titanate thin films*

#### SFB-Meeting Potsdam – Golm, Februar 21- 22, 2011

D. Heinert, C. Schwarz, P. Seidel, R. Nawrodt  
*Status of C4*

#### Kick-off SPP, Dresden, Februar 24 - 25, 2011

P. Seidel, F. Schmidl, v. Grosse, S. Schmdit, S. Döring, V. Tympel  
*Hybrid Josephson junctions with Co-doped Ba-122 electrode*

#### Workshop „Admittance Spectroscopy in CIGS solar cells“, 28. Feb / 1. March, Luxembourg

U. Reislöhner  
*Hopping conduction observed in Thermal Admittance Spectroscopy*

#### Second International Conference on Multifunctional, Hybrid and Nanomaterials, 6-10 March 2011, Strasbourg, France

M. Kozlik, S. Milz, C. Ronning, and T. Fritz  
*Combination of Zinc-phthalocyanine and Zinc Oxide for Functional Hybrid Materials*

#### Abschlusskolloquium SPP 1165 "Nanodrähte und Nanoröhren – von kontrollierter Synthese zur Funktion", 9.-10. März, Bonn

C. Ronning  
*Ion beam doping of semiconductor nanowires*

#### LSC Meeting, Arcadia/CA (USA), March 14-17, 2011

R. Nawrodt et al.  
*Material issues related to the 2.5<sup>th</sup> generation*

#### Frühjahrstagung der DPG, Dresden, March 13 - 18, 2011

J. Haarstrich, H. Metzner, C. Ronning, T. Rissom, C.A. Kaufmann, H.-W. Schock, A. Undisz  
*Influence of band-gap grading on luminescence properties of Cu(In,Ga)Se<sub>2</sub>*

C. Borschel, S. Spindler, D. Lerose, A. Bochmann, S.H. Christiansen, S.Nietzsche, M. Oertel, C. Ronning  
*Permanent bending and alignment of ZnO nanowires*

M. Kozlik, S. Milz, S. Möller, C. Ronning, T. Fritz  
*Hybrid Solar Cells made of Phthalocyanines and Zinc Oxide Nanowires*

S. Weidner, S. Geburt, J. Ye, S. Ulrich, C. Ronning  
*Significant stress reduction of cBN layers upon ion irradiation at elevated temperatures*

- M. Oertel, S. Götz, J. Haarstrich, H. Metzner, U. Reislöhner, C. Ronning, W. Wesch  
*Aspects of designing an optimized molybdenum back contact in CIGS-technology*
- C. Borschel, C. Ronning  
*Ion Beam Irradiation of Nanostructures - A 3D Monte Carlo Simulation Code*
- F. Limbach, T. Gotschke, T. Stoica, C. Pfüller, O. Brandt, A. Trampert, S. Geburt, C. Ronning, R. Calarco  
*Effects of doping profile on the optoelectronic properties of GaN nanowires*
- H. Metelmann, A. Laufer, D. Reppin, S. Graubner, A. Polity, B.K. Meyer, S. Geburt, C. Ronning  
*Quantification of Impurities in Cu<sub>2</sub>O*
- U. Kaiser, L. Chen, W. Heimbrodt, S. Geburt, C. Ronning  
*Energy transfer dynamics of the Mn 3 5 luminescence in ZnS:Mn nanostructures*
- R. Niepelt, A. Johannes, M. Gnauck, I. Slowik, S. Geburt, C. Ronning  
*Single ion implantation in semiconductor nanowires*
- A. Johannes, R. Niepelt, M. Gnauck, I. Slowik, A. Thielmann, S. Geburt, U. Schröder, D. Stoll, C. Ronning  
*Persistent Ion Beam induced Conduction in Semiconductor Nanowires*
- Y. Haj-Hmeidi, R. Niepelt, M. Gnauck, F. Schmidl, C. Ronning  
*Formation of p-Si/ZnO nanowire heterostructures for light emitting devices*
- C. Müller, S. Geburt, A. Laufer, B.K. Meyer, C. Ronning  
*Optical properties of as-grown and ion implanted Cu<sub>2</sub>O thin films*
- U. Schröder, M. Gnauck, R. Möller, B. Rudolph, W. Fritzsche, C. Ronning  
*Biofunctionalization of ZnO nanowires for DNA sensory applications*
- A. Thielmann, S. Geburt, M. Kozlik, J. Kühnel, C. Borschel, C. Ronning  
*Lasing in ZnO and CdS Nanowires*
- F. Riedel, S. Geburt, C. Ronning  
*Optical properties of terbium doped ZnS nanowires*
- S. Jankowski, L. Chen, S. Geburt, C. Ronning, W. Heimbrodt  
*Magneto-optical studies on doped and undoped ZnO nanostructures*
- Roman Forker and Torsten Fritz  
*Electronic Coupling and Charge Transfer between Metals and Epitaxial Organic Layers*
- Matthias Meißner, Bernd Schröter, and Torsten Fritz  
*PTCDA monolayer growth on epitaxial graphene*
- C.W. Rischau, C.S. Schnohr, E. Wendler, W. Wesch  
*Ion-beam-induced damage formation in CdTe at 15 K*
- T. Steinbach, J. Wernecke, W. Wesch  
*Structural modifications of low energy heavy ion irradiated Ge*
- T. Steinbach, C.C. Jacobi, W. Wesch  
*Development of porous structures in GaSb by ion irradiation*

T. Steinbach, C.S. Schnohr, L.L. Araujo, R. Giulian, D.J. Sprouster, M.C. Ridgway, D. Severin, M. Bender, C. Trautmann, W. Wesch  
*Structural modification of SHI irradiated amorphous Ge layers*

S. Döring, S. Schmidt, F. Schmidl, V. Tympel, V. Grosse, S. Haindl, K. Iida, F. Kurth, B. Holz-  
apfel, P. Seidel  
*Tunnelling spectroscopy of BaFe<sub>2</sub>As<sub>2</sub> / Au / PbIn thin film junctions*

S. Schmidt, S. Döring, F. Schmidl, V. Tympel, V. Gosse, S. Haindl, K. Iida, F. Kurth, I.  
Mönch, B. Holzapfel, P. Seidel  
*Thin film hybrid Josephson junctions with Co doped Ba-122*

P. Michalowski, C. Katzer, D. Kuhwald, M. Schmidt, V. Grosse, F. Schmidl, P. Seidel  
*Magnetic field sensors based on growth modified bi-crystal grain boundaries*

G. Hofmann, C. Schwarz, J. Komma, D. Heinert, R. Nawrodt, G. Hammond, A. Grib, P. Seidel  
*Mechanical dissipation in bulk silicon for precision measurements*

D. Kuhwald, C. Katzer, R. Erlebach, M. Schmidt, V. Grosse, F. Schmidl, P. Seidel  
*Characterization of YBa<sub>2</sub>Cu<sub>3</sub>O<sub>7-x</sub>-grain boundary contacts with Au-clusters*

C. Katzer, R. Erlebach, D. Kuhwald, P. Michalowski, F. Schmidl, I. Uschmann, P. Seidel  
*Growth of YBCO thin films and their interaction with gold nano clusters*

M. Schiffler, M. Büttner, F. Schmidl, P. Seidel  
*Temperature dependent magnetorelaxometry: Comparison between theory and experimental data*

S. Christke, R. Erlebach, F. Schmidl, J. Kräusslich, M. Rettenmayr, P. Seidel  
*The effect of gold nanoclusters on the growth and properties of homoepitaxial strontium titanate layers*

R. Erlebach, M. Hübner, S. Christke, V. Grosse, F. Schmidl, J. Kräusslich, M. Rettenmayr, P.  
Seidel  
*Enhancement of growth and structure properties of YBa<sub>2</sub>Cu<sub>3</sub>O<sub>7-δ</sub> thin layers by in situ incorporation of gold nano-clusters*

J. Komma, C. Schwarz, G. Hofmann, D. Heinert, R. Nawrodt, G. Hammond P. Seidel  
*Mechanical dissipation in thermally grown silica at low temperatures*

#### **Moriond Meeting, LaThuile/Italy, March 20 -27, 2011**

R. Nawrodt et al.  
*Experimental Approaches for the Einstein Telescope*

#### **Thüringer Werkstofftag 2011, Jena, 30. März 2011**

S. Günschmann, M. Hopfeld, T. Kups, V. Drescher, J. Wilden, C. Borschel, C. Ronning, P.  
Schaaf  
*Metall-Keramik-Verbund Schichten mit einstellbarem thermischen Ausdehnungskoeffizient*

**European Symposium on Biomaterials and Related Areas, EuroBioMat 2011, Jena, 13./14. April 2011**

J. Hönig, J. Sommerfeld, S. Kosan, T. F. Keller, K. D. Jandt, C. Ronning  
*Human Plasma Fibrinogen adsorption on ion beam nano-patterned Si and TiO<sub>2</sub> surfaces*

**IEEE Internat. Magnetics Conf. (Intermag 2011) Taipei/Taiwan, April 25 – 29, 2011**

S. Glathe, B. Burkhardt, P. Seidel, R. Mattheis  
*Evaluation of the effective domain wall mass by velocity measurements in permalloy nanostripes*

**Spring Meeting of the European Materials Research Society (E-MRS), Nice, France, 08. – 13. 05. 2011**

C.W. Rischau, C.S. Schnohr, E. Wendler, W. Wesch  
*Damage formation mechanisms in CdTe under ion irradiation*

E. Wendler  
*Empirical model of damage formation in ionic-covalent crystalline materials ion implanted at 15 K*

**481. WE-Heraeus-Seminar "Energy Materials Research by Neutrons and Synchrotron Radiation", Bad Honnef, 08. - 11. 05. 2011**

H. Kämmer, T. Steinbach, C. Stephan, S. Schorr, C.S. Schnohr  
*Atomic-scale structure of Cu(In,Ga)Se<sub>2</sub> by EXAFS*

**International Conference on Quantum Metrology 2011, Poznan/Poland, May 11 – 13, 2011**

A. Grib, P. Seidel  
*The influence of the resonator on the self-heating effect and the synchronization of Josephson junctions*

Y. Shukrinov, P. Seidel  
*Resonance features of coupled Josephson junctions in high temperature superconductors*

**DIPAC Hamburg, May 16 – 18, 2011**

W. Vodel, R. Geithner, R. Neubert, P. Seidel, K.K. Knaack, K. Wittenburg, A. Peters, H. Reeg, M. Schwickert,  
*News about the Cryogenic Current Comparator for Beam Diagnostics*

R. Geithner, W. Vodel, R. Neubert, P. Seidel, P. Kowina, F. Kurian, M. Schwickert, R. von Hahn  
*Sensor optimizations for a Cryogenic Current Comparator*

**Elba Meeting Elba/Italy, May 22 – 28, 2011**

R. Nawrodt, J. Komma, J. Hofmann  
*Silicon Research*

**ESF Exploratory Workshop, Bad Schandau, May 23 – 25, 2011**

P. Seidel

*Josephson effects in iron based superconductors (invited talk)*

**IAU Symposium 280: The Molecular Universe, Toledo, Spain, May 30 – June 3, 2011**

G. Rouillé, M. Steglich, Y. Carpentier, F. Huisken, and Th. Henning

*Spectroscopy of PAHs with carbon side chains*

**Recent trends in nanomagnetism, spintronics and their applications (RTNSA 2011)  
Ordizia/Spain, June 1 – 4, 2011**

S. Glathe, B. Burkhardt, P. Seidel, R. Mattheis

*Study on the effective domain wall mass determined by velocity measurements in perm-alloy nanostripes*

**Scandem 2011, Annual Meeting of Scandinavian Microscopy Society, June 8-10, 2011, Oulu**

M.E. Messing, C. Borschel, M.T. Borgström, H. Pettersson, C. Ronning

*Strongly Mn-doped GaAs nanowires of high crystalline quality*

**13th International Conference on the Formation of Semiconductor Interfaces (ICFSI 13), Prag, 3.7. bis 8.7.2011.**

Roman Forker, Marco Grünewald, Matthias Meißner, and Torsten Fritz

*Formation of Organic-on-Organic Heteroepitaxial Layers*

**ICIFMS16 Lausanne/Schweiz, July 04 – 08, 2011**

R. Nawrodt

*Mechanical spectroscopy of silicon as a low loss material for high precision mechanical and optical experiments*

**471. WEH-Seminar, Bad Honnef, July 5 -7, 2011**

V. Grosse, F. Schmidl, P. Seidel

*Current transport in epitaxially strained strontium titanate thin films*

**Workshop “Forschung mit Ionen- und Positronenstrahlen”, 04. – 05.07.2011, Universität der Bundeswehr München**

C.S. Schnohr

*Damage formation mechanisms in CdTe under ion irradiation*

C. Borschel

*Ionenbestrahlung von Nanostrukturen – 3D Monte-Carlo-Simulationen*

**16<sup>th</sup> International Conference on Radiation Effects in Insulators, Beijing, China, 14. – 19. August 2011**

S. Milz, J. Rensberg, E.-B. Kley, F. Schrepel, W. Wesch

*Ion beam synthesis of silver nanoclusters in lithium niobate*

E. Wendler, Th. Bierschenk, J. Sommerfeld, W. Wesch, D. Alber, G. Bukalis, L. Prinsloo, N. van der Berg, E. Friedland, J. Malherbe  
*Damage formation in neutron irradiated 4H-SiC*

E. Friedland, N.G. van der Berg, T.T. Hlatshwayo, J.J. Kuhudzai, J. B. malherbe, E. Wendler, W. Wesch  
*Diffusion behaviour of cesium in silicon carbide at  $T > 1000^{\circ}\text{C}$*

E. Friedland, N.G. van der Berg, J.B. Malherbe, E. Wendler, W. Wesch  
*Investigation cesium diffusion in silicon carbide*

E. Wendler, Th. Bierschenk, P. Schöppe, W. Wesch, N. van der Berg, E. Friedland, J. Malherbe  
*Damage formation in SiC ion implanted at 625 K*

**Euromat 2011 - European Congress and Exhibition on Advanced Materials and Processes, Montpellier, France, 11. – 14. 09. 2011**

H. Kämmer, T. Steinbach, M. Gnauck, C. Stephan, S. Schorr, C.A. Kaufmann, R. Caballero, T. Rissom, H.-W. Schock, C.S. Schnohr  
*Atomic-scale structure of  $\text{Cu}(\text{In},\text{Ga})\text{Se}_2$  as a function of stoichiometry*

**EUCAS/ISEC/ICMC Superconductivity Centennial Conference, Den Haag/Netherlands, September 18 – 23, 2011**

P. Seidel, S. Döring, S. Schmidt, V. Tympel, F. Schmidl, S. Haindl, K. Iida, B. Holzapfel  
*Josephson and tunneling junctions with thin films of ion based superconductors*

**ISS 2011 Tokyo/Japan, October 24 – 26, 2011**

P. Seidel, S. Döring, S. Schmidt, F. Schmidl, V. Tympel, S. Haindl, F. Kurth, I. Mönch, K. Iida, B. Holzapfel  
*Development of iron-based superconducting devices*

P. Seidel  
*Films, junctions and electronic devices*

**Kick-off Meeting IRON-SEA Tokyo/Japan, 27.10.11**

P. Seidel  
*Josephson effects in iron based superconductors*

**Workshop on Precision Physics and Fundamental Physical Constants, December 5.-9.11, Dubna, Russia**

Y. Shukrinov, P. Seidel, W. Nawrocki  
*The perspective of intrinsic Josephson junctions for quantum metrology*

**Fall meeting of the Materials Research Society (MRS), Boston, USA, 27. Nov. – 2. Dec., 2011**

F. Limbach, T. Gotschke, R. Calarco, T. Stoica, R. Caterino, C. Pfueller, O. Brandt, X. Kong, A. Trampert, L. Geelhaar, S. Geburt, C. Ronning and H. Riechert  
*Effects of Doping Profile on the Optoelectronic Properties of GaN Nanowires*

C. Borschel, M.E. Messing, K. Mergenthaler, M. Borgstroem, W. Paschoal, J. Wallentin, S. Kumar, K. Deppert, C. Canali, H. Petterson, L. Samuelson, and C. Ronning  
*A New Route towards Semiconductor Nanospintronics: Highly Mn-Doped GaAs Nanowires Realized by Ion-Implantation under Dynamic Annealing Conditions*

F. Riedel, S. Geburt, C. Borschel, U. Kaiser, W. Heimbrodt, C. Ronning  
*Intense Intra-4f-Emission from Tb Doped Single ZnS Nanowires*

A. Thielmann, S. Geburt, C. Borschel, J. Kuehnel, M. Kozlik, A. McDonnell, K. Sunter, F. Capasso, C. Ronning  
*Low Threshold Room Temperature Lasing of Single CdS Nanowires*

W. Molnar, A. Lugstein, P. Pongratz, M. Seyring, M. Rettenmayr, C. Borschel, C. Ronning, N. Auner, C. Bauch, E. Bertagnolli  
*Shape Control Method for Prismatic Si-NWs by Subeutectic VLS Growth Using Cubic  $\alpha$ -NiSi<sub>2</sub> as Catalyst.*

S. Milz, J. Rensberg, C. Ronning, W. Wesch  
*Structural and Optical Properties of Ion Beam Synthesized Silver Nanoclusters in Lithium Niobate*

J. Sommerfeld, T.F. Keller, K.D. Jandt, C. Ronning  
*Biofunctionalization of Diamond like Carbon Layers*

**International Conference on “Next Generation Solar Energy: From Fundamentals to Applications”, 12.-14. Dezember 2011, Schloss Erlangen**

R. Niepelt, M. Gnauck, C. Gutsche, A. Lysov, W. Prost, F.-J. Tegude, C. Ronning  
*Determination of minority carrier diffusion lengths in axial GaAs nanowire pn-junctions*

M. Kozlik, S. Milz, R. Forker, A. Donat, S. Paulke, C. Ronning, T. Fritz  
*Zinc Phthalocyanine in Hybrid Solar Cells with Zinc Oxide Nanowires*

**International Conference on Nanomaterials & Nanotechnology, Delhi, India, 18.-21. Dez. 2011**

S. Kumar, C. Borschel, M.E. Messing, M.T. Borgström, W. Paschoal Jr., J. Wallentin, K. Mergenthaler, K. Deppert, C.M. Canali, H. Pettersson, L. Samuelson, C. Ronning  
*Highly Mn-doped GaAs nanowires and their transport properties*



## 5.4 Theses

### PhD theses

Christian Kraft	<i>Spektroskopische Untersuchungen zur Dotierung von polykristallinen CdTe-Schichten für Solarzellen</i>
Jakob Haarstrich	<i>Interface modification by ion implantation and optical characterization of high-efficiency Cu(In,Ga)Se<sub>2</sub> solar cells</i>
Veit Große	<i>Ladungsträgertransport in epitaktischen Strontiumtitanat-Schichten für den Einsatz in supraleitenden Bauelementen</i>
Sascha Glathe	<i>Field driven domain wall dynamics in ferromagnetic nanostripes</i>
Torsten Schmidt	<i>Charakterisierung der Photolumineszenz siliziumbasierter Nanoteilchen mittels Einzelteilchen- und Ensemblespektroskopie</i>
Mathias Steglich	<i>Experimentelle und theoretische Untersuchungen zur UV-VIS-Spektroskopie großer astrophysikalisch relevanter Kohlenwasserstoff-Moleküle</i>

### Diploma and Master theses

Henry Holland-Moritz	<i>Untersuchung der elektrischen Eigenschaften von Halbleiternanodrähten</i>
Christian Müller	<i>Optische Eigenschaften reaktiv gesputterter Kupferoxid-Schichten und Wachstum von Kupferoxid-Nanodrähten</i>
Franziska Riedel	<i>Terbiumdotierte Zinksulfidnanodrähte</i>
Andreas Thielmann	<i>Aufbau einer Mikrophotolumineszenzapparatur und Lasingeigenschaften von ZnO- und CdS-Nanodrähten</i>
Andreas Johannes	<i>In-situ Characterisation of ion-doped Zinc Oxide Nanowires</i>
Julian Kühnel	<i>Cathodoluminescence probing of semiconductor nanowires and plasmonic nanostructures</i>
Jessica Höning	<i>Untersuchungen zur Adsorption von Proteinen auf nanostrukturierten Oberflächen</i>
Susann Spindler	<i>Morphologieänderungen und Ausrichtung von Halbleiternanodrähten unter Ionenbeschuss</i>
Marco Grünewald	<i>Organische Heteroepitaxie von PTCDA und SnPc auf einkristallinem Silber</i>
Falko Sojka	<i>Quantifizierung von LEED – Aufnahmen für Untersuchungen an organischen Dünnschichten</i>
Sandra Christke	<i>Untersuchungen zum epitaktischen Schichtwachstum von SrTiO<sub>3</sub> unter dem Einfluss von Au-Nanoclustern</i>
Sebastian Döring	<i>Untersuchungen zu elektrischen Eigenschaften von FeAs Supraleitern</i>
Ralf Erlebach	<i>Untersuchungen zum Einfluss von Au-Clustern auf die supraleitenden Eigenschaften von YBa<sub>2</sub>Cu<sub>3</sub>O<sub>7-δ</sub>-Schichten</i>
Gerd Hofmann	<i>Charakterisierung von Bulk-Materialien bei tiefen Temperaturen</i>
Christian Katzer	<i>Herstellung und Charakterisierung von HTSL-BE auf Basis von wachstumsmodifizierten Korngrenzenkontakten</i>
Julius Komma	<i>Untersuchung und Charakterisierung optischer Schichten für Präzisionsmesstechnik</i>

Daniel Kuhwald	<i>Charakterisierung von Magnetfeldsensoren auf der Basis von wachstumsmodifizierten YBCO-Schichten</i>
Peter Michalowski	<i>Hoch-TC-Gradiometer mit Au-Nanopartikeln</i>
Matthias Schmidt	<i>Temperaturabhängige Charakterisierung von HTSL-DC-SQUID-Gradiometern</i>
Stefan Schmidt	<i>Tunnelmessungen an eisenbasierten Supraleitern</i>
Alexander Hüsler	<i>Detektion der Verteilung von Defekten in gerichtet erstarrtem multikristallinen Silizium für die Photovoltaik mittels Photolumineszenz (extern Schott AG)</i>
Alexander Winkler	<i>Comparison of Characterization Methods for CdTe / CdZnTe Radiation Detector Materials and Development of an Automated Test System (extern U Helsinki)</i>
Andreas Falk	<i>Metallisierung und Charakterisierung der passivierten Rückseite von Siliziumsolarzellen (extern CIS Erfurt)</i>
Tim Sprenger	<i>Fett-Wasser-Separation mit erweiterten Dixon-Techniken (extern medizinische Fakultät)</i>
Martin Schreivogel	<i>Silizium Nanodrähte: Herstellung, Integration in Bauelemente zur photovoltaischen Energiekonversion und Charakterisierung (extern IPHT)</i>
Kasper Rothenfuß	<i>Construction of the MICE Electron Muon Ranger (extern CERN, U Genf)</i>
Anja Harpf	<i>Herstellung und Charakterisierung von CdTe-Solarzellen einer neuen Prozeßlinie</i>
Helena Kämmer	<i>Strukturanalyse an Cu(In,Ga)Se<sub>2</sub> mittels Synchrotronstrahlung</i>
<b>Bachelor theses</b>	
Marcel Wille	<i>Qualitative Untersuchung diamantähnlicher Schichten, hergestellt mittels Massenseparierter Ionenstrahldeposition (MSIBD)</i>
Moritz Laubscher	<i>Wachstum und Charakterisierung von Halbleiternanodrähten auf vorstrukturierten Substraten</i>
Stefanie Kosan	<i>Ionenstrahlerosion von TiO<sub>2</sub></i>
Martin Krauß	<i>Bestimmung der Bandlücke an Cu(In,Ga)Se<sub>2</sub>-Schichten mit Hilfe optischer Messungen</i>
Alexandra Mannig	<i>Optische und topologische Charakterisierung einzelner modifizierter Goldnanopartikel in Lösung (extern IPHT)</i>
Hendrik Bernhardt	<i>Aufbau und Schichtoptimierung einer Sputteranlage für die Herstellung von Oxiden</i>
Martin Feltz	<i>Herstellung von Tunnelstrukturen auf der Basis von Supraleiter-Elektroden</i>
Sandra Gottwals	<i>Pb-Deckelelektroden für Tunnel- und Josephsonkontakte</i>
Manuel Monecke	<i>Herstellung und Charakterisierung von Ti/Au-Schichten für supraleitende Bauelemente</i>
Philipp Naujok	<i>Herstellung und Untersuchung von SiO<sub>2</sub>-Schichten für integrierte SL-Bauelemente</i>

David Reifert	<i>Untersuchungen zum thermischen Verdampfen von Supraleitern</i>
Benjamin Rößler	<i>Herstellung und Charakterisierung von Deckelektroden für Tunnelkontakte</i>
Martin Salge	<i>Bestimmung optischer Parameter bei tiefen Temperaturen</i>
Felix Felgenträger	<i>Spektroskopische Untersuchung von neutronenbestrahltem SiC</i>
Philipp Schöppe	<i>Untersuchung der Schädigungsbildung durch Implantation der Eigenionen in 4H-SiC bei 625 K</i>
Henning Gutheil	<i>Strahlenschädenerzeugung in CdTe bei Ionenbestrahlung</i>
Michael Brückner	<i>Herstellung und Charakterisierung von CdTe-Dünnschichtsolarzellen bei Variation der Substrattemperatur</i>
Christian Stolze	<i>Phosphordotierung von CdTe-Dünnschichtsolarzellen</i>
Yiyang Zhang	<i>Matrixisolationsspektroskopische Untersuchungen der PAHs Anthracen und 9-Ethynyl-Anthracen</i>
Christian Udhardt	<i>Untersuchung des epitaktischen Wachstums von Molekülschichten auf einkristallinen Substraten</i>
Alexander Kusch	<i>Elektrische Charakterisierung hybrider Solarzellen</i>

## 6. Cooperations, guests and colloquia at IFK

The Institute of Solid State Physics collaborates with a large number of Institutes and Universities in Germany and around the world and has also close connections with several companies. In the framework of these wide spread contacts in 2011 a number of scientists from various countries visited our Institute to perform experiments, discuss scientific results obtained within joint projects and to give talks in the colloquium of the Institute of Solid State Physics.

### 6.1 Visiting scientists

Prof. Dr. K. Baruth-Ram	iThemba Labs, Cape Town, Südafrika
Dr. Rupert Oulton	Imperial College London
Prof. Dr. Iman Roqan	KAUST, Jiddah, Saudi-Arabien
Dr. Enrico Fumagalli	Università degli Studi di Milano-Bicocca
Alexey Gavrik	Lomonossow Universität Moskau
Dr. Alexander Grib	Kharkov National University, Physics Department
Dr. Enrico Serra	Fondazione Bruno Kessler, Trento/Italy
Dr. Yury Shukrinov	Bogoliubov Laboratory of Theoretical Physics, Joint Institute for Nuclear Research Dubna
Dr. Giles Hammond	IGR Glasgow
Dr. Ian Martin	University of Glasgow
Prof. Alexander Shengelaya	Tbilisi State University, Georgia
Dr. Andrii Shapovalov	Institute of Metal Physics Kiew
Dr. Volodymyr Shaternik	Institute of Metal Physics Kiew
Dr. Antonio Borrielli	Universität Trento
Dr. Garrett Cole	Universität Wien
Dr. Stuart Reid	Universität Glasgow
Prof. Dr. Erich Friedland	University of Pretoria, Pretoria, South Africa
Prof. F.F. Komarov	Universität Minsk, Minsk, Belarus
Prof. Dr. Johan Malherbe	University of Pretoria, Pretoria, South Africa
Prof. Dr. Marika Schleberger	Universität Duisburg-Essen
Prof. Dr. Wolfgang Ensinger	TU Darmstadt
Dr. Katharina Lorenz	ITN, Sacavem, Portugal
Prof. Dr. Nikolai Sobolev	Universität Aveiro, Aveiro, Portugal
Dr. Andrey Timopheev	Universität Aveiro, Aveiro, Portugal
Dr. Thulani Hlatswayo	University of Pretoria, South Africa
Dolly Langa, MSc	University of Pretoria, Pretoria, South Africa
Dr. Platon Karasev	Dept. of Physical Electronics, State Polytechnic University, St Petersburg, Russian Federation
Dr. Alexander Azarov	Department of Physics, University of Oslo, Oslo, Norway
Prof. Dr. Susan Schorr	Helmholtz-Zentrum Berlin für Materialien und Energie & Freie Universität Berlin

### 6.2 Colloquia at the Institute of Solid State Physics

Dr. Frank Schwierz (TU Ilmenau), 07. Jan. 2011  
*Graphene - the material for future electronics?*

Dr. Marcello Campione (Università degli Studi di Milano Bicocca), 21. Jan. 2011  
*Probing the properties of the surfaces of organic crystals: from epitaxy to nanotribology*

Prof. Dr. Rudolf Bratschitsch (TU Chemnitz), 04. Feb. 2011

*Ultrafast quantum optics with solid-state nanosystems*

Dr. Rupert Oulton (Imperial College London), 11. Feb. 2011  
*Deep sub-wavelength lasers based on semiconductor nano-structures*

Prof. Dr. Wolfgang Ensinger (TU Darmstadt), 15. April 2011  
*Ion track etched nanochannels for electrochemical sensing*

Prof. Dr. Nicolaas Stolwijk (U Münster), 29. April 2011  
*Diffusionsexperimente in CIGS Solarzellenmaterial*

Prof. Dr. Joachim Albrecht (Hochschule Aalen), 13. Mai 2011  
*Flusslinienbewegung in metallischen Supraleiterschichten*

Dr. Martin Knapfer (IFW Dresden), 27. Mai 2011  
*Elektronische Eigenschaften kondensierter aromatischer Kohlenwasserstoffe: dotiertes und nichtdotiertes Picen*

Prof. Dr. Susan Schorr (FU Berlin/HZ Berlin), 24. Juni 2011  
*New insights into absorber materials for thin film solar cells by neutron diffraction*

Prof. Dr. Marika Schleberger (U Duisburg-Essen), 8. Juli 2011  
*Oberflächenmodifikation nach intensiver elektronischer Anregung*

Dr. Jürgen Kräußlich (FSU Jena, IOQ), 28. Okt. 2011  
*Röntgendiffraktometrische Charakterisierung epitaktisch gewachsener dünner Schichten*

Prof. Dr. Alexander Schengelaya (Tbilisi State University, Georgien), 11. Nov. 2011  
*Study of advanced superconducting and magnetic materials using moun-spin rotation technique*

Prof. Dr. Hans-Gerd Boyen (Universität Hasselt, Belgien) 9. Dez. 2011  
*Metal/Molecule Multilayers - a new design tool for molecular electronics?*

## **7. Teaching activities**

### **7.1 Lectures**

Grundkurs Experimentalphysik 1: Mechanik und Wärme	Prof. Dr. C. Ronning
Nukleare Festkörperphysik	Prof. Dr. C. Ronning
Nanomaterials and Nanotechnology	Prof. Dr. C. Ronning
Physik der Materie II	Prof. Dr. T. Fritz
Physik der Materie I	Prof. Dr. W. Wesch
Festkörperanalyse mit energiereichen Teilchen	Dr. F. Schrempel, Prof. Dr. W. Wesch
Festkörpermodifikation mit Ionenstrahlen	PD Dr. E. Wendler
Physik für Nebenfach-Studenten (Biologie, Ernährungswiss., Pharmazie, Biogeowissenschaften, Chemie, Biochemie)	Prof. Dr. W. Wesch
Kerne und Teilchen	Prof. Dr. W. Wesch
Photovoltaik I	PD Dr. H. Metzner
Festkörperphysik I	Prof. Dr. P. Seidel
Elektronik	Dr. R. Nawrodt
Messtechnik	Dr. R. Nawrodt
Supraleitung	Prof. Dr. P. Seidel
Optoelectronics (englisch)	PD Dr. F. Schmidl
Gravitational wave detection (englisch)	Dr. R. Nawrodt
Experimentalphysik für Mediziner	PD Dr. F. Schmidl
Supraleitende Materialien	Prof. Dr. P. Seidel
Tiefemperaturphysik	M. Thürk , Prof. Dr. P. Seidel
Einführung in die Halbleiterphysik	Prof. Dr. T. Fritz

### **7.2 Seminars**

Proseminar zum Fortgeschrittenenpraktikum	Dr. B. Schröter
Oberflächenanalytik	Dr. R. Forker
Neuere Arbeiten zur Laborastrophysik	Prof. Dr. F. Huisken, Dr. H. Mutschke
Physik der Materie I	PD Dr. K. Gärtner, PD Dr. E. Wendler
Physik für Biogeowissenschaftler	PD Dr. E. Wendler, M. Schmidt
Phyisk der Materie II	Dr. R. Forker

Elektronik für Physiker	D. Heinert
Experimentalphysik I für Physiker	PD Dr. E. Wendler
Experimentalphysik II für Physiker	PD Dr. E. Wendler
Kerne und Elementarteilchen	PD Dr. K. Gärtner, Dr. C.S. Schnohr
Physik für Chemiker	Dr. C.S. Schnohr
Tiefemperaturphysik und Supraleitung	Prof. Dr. P. Seidel
Supraleitung	Prof. Dr. P. Seidel
Optoelectronics (englisch)	PD Dr. F. Schmidl
Tutorium (Physik für Mediziner)	PD Dr. F. Schmidl, C. Katzer
Oberseminar (Festkörper/Material: Masterst.)	Prof. Dr. P. Seidel
Festkörperphysik	Dr. R. Forker
Festkörperphysik (Materialwissenschaftler)	Dr. V. Tympel
Supraleitende Materialien	Prof. Dr. P. Seidel
Tiefemperaturphysik	M. Thürk
Seminar zur Staatsexamensprüfung Lehramt Ex-physik	Prof. Dr. P. Seidel
<b>7.3 Practica</b>	
Fortgeschrittenen-Praktikum	Dr. B. Schröter (Leitung) M. Thürk, C. Schwarz
Praktikum für Biochemiker	Prof. Dr. W. Wesch (Leitung)
Praktikum für Biologen	Prof. Dr. W. Wesch (Leitung)
Praktikum für Nebenfächler	Prof. Dr. W. Wesch (Leitung) Dr. C.S. Schnohr
Humanmediziner	PD Dr. F. Schmidl (Leitung)
Zahnmediziner	PD Dr. F. Schmidl (Leitung)
Grundpraktikum	Dr. R. Nawrodt (Leitung), PD Dr. F. Schmidl, H. Mühlig, R. Neubert, J. Komma
Elektronikpraktikum	Dr. R. Nawrodt (Leitung), PD Dr. F. Schmidl, R. Neubert, H. Mühlig, R. Geithner, S. Döring
Messtechnik	R. Nawrodt (Leitung), H. Mühlig, R. Neubert, Dr. V. Tympel
Optikpraktikum	PD Dr. F. Schmidl, Dr. R. Nawrodt, H. Mühlig, R. Neubert

## 8. Personnel

### Professors

Prof. Dr. habil. Carsten Ronning (director)  
Prof. Dr. habil. Torsten Fritz  
Prof. Dr. habil. Paul Seidel  
Prof. Dr. habil. Werner Wesch  
Prof. Dr. habil. Friedrich Huisken

### Scientific Staff

PD Dr. habil. Heinrich Metzner	PD Dr. habil. Frank Schmidl
PD Dr. habil. Elke Wendler	Dr. Cornelia Jäger
Dr. Claudia Schnohr	Dr. Yvain Carpentier
Dr. Udo Reislöhner	Dr. Gaël Rouillé
Dr. Ernst Glaser	Dr. Mathias Steglich
Dr. Mathias Hädrich	Dr. Serge Krasnokutski
Dr. Bernd Schröter	Dr. Ronny Nawrodt
Dr. Roman Forker	Dr. Volker Tympel

### PhD Students

Christian Borschel	Steffen Milz
Jakob Haarstrich	Michael Oertel
Christian Kraft	Jana Sommerfeld
Christoph Heisler	Raphael Niepelt
Sebastian Geburt	Yaser Haj-Hmeidi
Martin Gnauck	Davide Cammi
Andreas Johannes	Tolou Sabri
Marco Grünewald	Falko Sojka
Michael Kozlik	Matthias Meissner
Torsten Schmidt	Karsten Potrick
Mathias Steglich	Tobias Steinbach
Matthias Schmidt	Markus Büttner
Sebastian Döring	Rene Geithner
Daniel Heinert	Gerd Hofmann
Christian Katzer	Julius Komma
Christian Schwarz	Stefan Schmidt

### Extern PhD students

Sascha Glathe	(IPHT Jena)
Michael Blech	(CiS Erfurt)
Matthias Rost	(Bosch Solar Energy, Erfurt)
Stephan Pohlner	(Avancis GmbH, Munich)
Boris Ivanov	(IPHT Jena)
Gregor Oelsner	(IPHT Jena)
Thomas Schönau	(IPHT Jena)
Uwe Schinkel	(IPHT Jena)
Ivo Zunke	(Innovent Jena)



## **Diploma and Master Students**

Julian Kühnel  
Falk Wyrwa  
Henry Holland-Moritz  
Jessica Hönig  
Susann Spindler  
Andreas Thielmann  
Sören Paulke  
Jura Rensberg  
Emmanuel Schmidt  
Aaron Reupert  
Ralf Erlebach

Irma Slowik  
Sven Möller  
Christian Müller  
Stefan Weidner  
Franziska Riedel  
Kristin Wachter  
Helena Krämmer  
Anne Nathanael  
Sandra Christke  
Peter Michalowski  
Daniel Kuhwald

## **Technical Staff**

Ulrich Barth  
Uta Bornkessel  
Uwe Eberhardt  
Tobias Eißmann  
Lutz Föllmer  
Silke Frunzke  
Kristina Garlipp  
Frank Jehn  
Gerald Lenk

Holger Mühlig  
Anja Mittelstädt  
Ralf Neubert  
Stefan Prass  
Helga Rudolph  
Sylvia Stender  
Matthias Thürk  
Carmen Voigt